

THESIS

GEOLOGIC MAPPING AND KINEMATIC ANALYSIS OF THE INDEPENDENCE MINE
SHEAR ZONE IN THE SANGRE DE CRISTO RANGE, SOUTHERN COLORADO:
EXTENSIONAL REACTIVATION OF A LARAMIDE REVERSE FAULT

Submitted by

Michael C. Sitar

Department of Geosciences

In partial fulfillment of the requirements

For the Degree of Master of Science

Colorado State University

Fort Collins, Colorado

Spring 2023

Master's Committee:

Advisor: John Singleton

John Ridley

Stephen Leisz

Jonathan Saul Caine

Copyright by Michael Cole Sitar 2023

All Rights Reserved

ABSTRACT

GEOLOGIC MAPPING AND KINEMATIC ANALYSIS OF THE INDEPENDENCE MINE SHEAR ZONE IN THE SANGRE DE CRISTO RANGE, SOUTHERN COLORADO: EXTENSIONAL REACTIVATION OF A LARAMIDE REVERSE FAULT

The Sangre de Cristo Range in southern Colorado records some of the deepest Cenozoic structural levels in the Rocky Mountain region. Exposures of Laramide-age contractional mylonites show evidence for brittle-plastic extensional overprinting associated with the Rio Grande rift. This study examines the relation between Laramide contraction and Rio Grande rift extension by detailed geologic mapping and kinematic, geochronological, and geochemical analyses in a 50 km² area centered on the Independence Mine shear zone (IMSZ), formerly called the Independence Mine thrust. The IMSZ is a 15- to 100-meter-thick, shallow-to-moderately (25°–62°), WSW-dipping brittle-plastic shear zone near the topographic base of the western flank of the range. It displays microstructural evidence for initiation as a top-NE contractional mylonite zone consistent with Laramide kinematics but is pervasively overprinted by deformation fabrics indicating top-SW extensional reactivation. Top-SW microstructures are characterized by phyllosilicate-lined C- and C'-shear bands and mixed brittle-plastic deformation of quartz. Mapping shows that the IMSZ is the thickest member of a system of mylonitic shear zones that dip shallowly to moderately (25°–67°) to the WSW and are hosted primarily within Proterozoic gneiss. Shear zones in amphibole-rich gneiss are commonly dominated by chlorite whereas those in quartzo-feldspathic gneiss have abundant white mica. Many of the thinner shear zones also record top-SW overprinting of top-NE fabrics. Though both top-NE and top-SW shear fabrics involve cataclasis and quartz dislocation creep, extensional overprinting appears to be

mostly restricted to mylonites where secondary phyllosilicates form an interconnected weak phase. These relations are interpreted as fluid-mediated, reaction-weakening gradients where lithologically controlled rheological contrasts were variably sensitive to extensional reactivation. One top-SW shear zone adjacent to the IMSZ cuts a gabbro stock that was dated at 25.7 ± 0.7 Ma using LA-ICP-MS zircon U-Pb geochronometry. Synkinematic monazite grains in two samples of the IMSZ yield LA-ICP-MS U-Pb and U-Th-Pb ages of 24.9 ± 3.0 Ma and 22.2 ± 0.7 Ma, respectively. These data are consistent with extensional reactivation occurring during Late Oligocene to Early Miocene time. The IMSZ and associated reactivated shear zones may represent mid-crustal extension that was widespread in the earliest stages of Rio Grande rifting before extension shifted to high-angle brittle-regime normal faults along the range front.

ACKNOWLEDGEMENTS

I would like to first and foremost express my deepest gratitude to my advisor, John Singleton. The work presented in this thesis would probably not have been possible without his encouragement and moral support, and certainly not without his conceptual and material scientific contributions. John was not alone in this regard: Paul O’Sullivan, Jeff Rahl, and Paula Leek also provided vital analytical services and data for the project. Likewise for Jacob King, who valiantly assisted in mapping the lower range-front in spite of harsh weather, grueling terrain, and probably-not-unrelated injuries. Edits from my committee members, John Ridley, Jonathan Saul Caine, and Steve Leisz allowed me to significantly improve this thesis, and I regret not being able to incorporate all of their suggestions.

I am also indebted to the various property owners in the Crestone area who allowed me to stumble around on their (in some cases, sacred) land while geologizing. They include but are not limited to the Vajra Vidya Retreat Center, the Sangdo Palri Temple, and the Crestone MahaLakshmi Temple.

Work on this project was supported by grants from the National Science Foundation (award # 2115719) and USGS EDMAP Program (award # G21AC10493), as well as by a Warner College of Natural Resources research assistantship.

Finally, thank you to my family and to Mikaela Moore, for endless love and support.

TABLE OF CONTENTS

ABSTRACT.....	ii
ACKNOWLEDGEMENTS.....	iv
LIST OF SUPPLEMENTARY DATA INCLUDED SEPARATELY.....	vii
1. INTRODUCTION	1
1.1. Geographic Setting and History	3
1.2. Geologic Setting	9
1.2.1. Proterozoic	11
1.2.2. Paleozoic	12
1.2.3. Mesozoic	14
1.2.4. Cenozoic	15
1.3. Prior Work	17
1.4. Research Objectives and Relevance	19
2. METHODS AND MATERIALS.....	21
2.1. Geologic Mapping	21
2.2. Geospatial Analyses.....	24
2.3. Microstructural Analysis.....	26
2.4. Geochronology and Thermochemistry	27
2.5. Whole Rock Geochemistry	28
3. RESULTS	30
3.1. Geologic Units	30
3.1.1. Proterozoic Units	30
3.1.2. Paleozoic Units	36
3.1.3. Cenozoic Intrusives.....	42
3.1.4. Surficial Deposits.....	46
3.2. Geologic Structures.....	49
3.2.1. Proterozoic Structures.....	49
3.2.2. Thrust/Reverse Faults & Associated Structures	51
3.2.3. Shear Zones.....	54
3.2.4. Rift-related Brittle Regime Structures	63
3.3. Minimum Displacement Estimates	65
3.4. Microstructural Analysis.....	70

3.4.1. EBSD	78
3.5. Geochronology and Thermochronology	82
3.6. Whole Rock Geochemistry	87
4. DISCUSSION	94
4.1. Geologic History	94
4.1.1. Proterozoic	94
4.1.2. Paleozoic	95
4.1.3. Laramide	96
4.1.4. Cenozoic	99
4.2. Extensional Shear Zone Rheology and Controls on Reactivation	102
5. CONCLUSIONS	107
REFERENCES	109
Appendix A: Gabbro Geochemistry	125

LIST OF SUPPLEMENTARY DATA INCLUDED SEPARATELY

Plate 1: Geologic Map of the Western Flank of the Sangre de Cristo Range Near Crestone,
Colorado

Dataset 1: Waypoints and Localities in Study Area

Dataset 2: Sample and Petrographic Section List with Kinematics

Dataset 3: Raw Structural Orientation Data from Study Area

Dataset 4: Per-Station Per-Structure Structural Data E1 Eigenvector Orientations

Dataset 5: Zircon Fission Track and U-Pb Analytical Data

Dataset 6: Calcite U-Pb Analytical Data

Dataset 7: Monazite U-Th-Pb Analytical Data

Dataset 8: Whole Rock Geochemistry Data

1. INTRODUCTION

Faults and shear zones play a fundamental role in accommodating strain in the Earth's crust. Brittle faulting occurs in the upper to middle crust, whereas plastic shear generally takes place in the middle to lower crust and uppermost mantle; faults commonly evolve into plastic shear zones where they extend into the middle crust. The brittle-plastic transition zone, where mylonitic fault rocks begin to form in shear zones, lies at the boundary between the upper and middle crust. This transition is also where the crust is strongest, so its rheology and variations therein likely play an important role in governing how, where, and when faults are active in the brittle crust (Brace & Kohlstadt, 1980; Behr & Platt, 2014). The degree to which the behavior of the middle crust is itself influenced by structural inheritance is not well understood, but studying exhumed brittle-plastic shear zones that have undergone polyphase deformation (e.g., reactivation) within the middle crust may help to rectify this.

The processes governing initiation of brittle faults and the conditions under which brittle faults may be reactivated are well-understood (Anderson, 1905; Byerlee, 1978; Sibson, 1977, 1985). Brittle faults that are not optimally oriented (e.g., non-Andersonian) in a stress field at a particular time may be reactivated given a sufficiently high pore fluid pressure (p_f), a low coefficient of static friction (μ), or some combination thereof (Byerlee, 1978; Sibson, 1985). Several studies of active faults (e.g., some segments of the San Andreas Fault) suggest that frictionally weak clay minerals found in fault gouge can facilitate slip along misoriented faults in the upper crust, but these minerals break down at greater depths ($>7-8$ km), and slip along non-Andersonian faults and shear zones near and below the brittle-plastic transition is consequently somewhat enigmatic (Carpenter et al., 2012). Frictionally weak chlorite-rich shear fabrics have

been proposed as a serviceable low- μ substitute for clay gouge in the middle crust (Carpenter et al., 2012).

In addition to increasing ρ_f , fluids likely play multiple additional roles in weakening the brittle-plastic transition to facilitate fault-shear-zone reactivation. Chlorite is relatively strong while dry but weakens substantially when wet (Colletini, 2011). In the absence of very weak minerals such as (wet) chlorite, fluids at depth can weaken conventionally stronger silicate minerals such as quartz by infiltrating and disrupting their crystalline structures (i.e., ‘hydrolytic weakening’; Griggs (1967)). Fluids can likewise produce weaker minerals through alteration of stronger ones, such as amphiboles and feldspars (i.e., ‘reaction weakening’; O’Hara (1988)).

The Independence Mine shear zone (IMSZ) is a SW-dipping brittle-plastic shear zone that is exposed along the western flank of the Sangre de Cristo Range in southern Colorado and is characterized by chlorite-rich mylonites and ultramylonites. Since the IMSZ and related shear zones have also been exhumed from the brittle-plastic transition, they could also provide a useful analogue for how other sub-optimally oriented faults behave at depth. Though it has previously been mapped at 1:24,000 or smaller-scale (Clement, 1952; Lindsey et al., 1985), the IMSZ has not been studied in detail. Outcrops of IMSZ mylonites commonly display tectonite fabrics consistent with top-SW (normal-sense) displacement. These fabrics are locally mixed with fabrics and kinematic indicators consistent with top-NE (reverse-sense) displacement. Regional ENE-directed crustal shortening is known to have occurred during the Late Cretaceous to early Paleogene Laramide orogeny, with subsequent WSW-directed extension associated with the Rio Grande rift occurring from the Late Oligocene until the present day (e.g., Lindsey, 2010). Known local Laramide thrust faults are mostly shallowly SW-dipping, and local Rio-Grande-rift-associated normal faults are moderately to steeply SW-dipping (e.g., Brister & Gries, 1994;

Kluth & Schaftenaar, 1994; Lindsey et al., 1984). The dip of the IMSZ generally appears to be intermediate to those of local Laramide and Rio Grande faults, and contradictory kinematic fabrics within it suggest that it may have been active in both events (i.e., accommodation of Laramide shortening prior to rift-related extensional reactivation). In this study, the IMSZ and its geologic surroundings were investigated through detailed geologic mapping in combination with microstructural, geochemical, and geochronological analyses in order to learn more about its structural history and, more broadly, how deformation has been accommodated in the middle crust during regional shortening and rifting events.

1.1. Geographic Setting and History

The Sangre de Cristo Range constitutes the northern end of the Sangre de Cristo Mountains, which are themselves the southernmost subrange of the Rocky Mountains (Fig. 1). The range, which runs NNW to SSE between the towns of Poncha Springs and Blanca, Colorado, separates the westerly San Luis Valley from the easterly Wet Mountain Valley, and is roughly 120 km long and 15 km wide (Fig. 1). Both the southwestern and northeastern sides of the range rise sharply towards a spine of 13,000–14,350 ft. peaks and ridges running along the approximate longitudinal center of the range (Fig. 1). The range's steep slopes and narrow width can be directly attributed to its origin as an extensional fault block (Lindsey, 2010), and triangular facets and prograding alluvial fans characteristic of active normal faulting are indeed observable along each flank (Fig. 1). Eolian sand sourced from across the San Luis Valley collects against the western flank of the range, and especially so in the embayment to the NW of Blanca Peak, where it forms the dune fields of Great Sand Dunes National Park (Fig. 1; Valdez, 2007). Though the Sangre de Cristo National Wilderness area encompasses most of the high interior of the range to

the N and E of Great Sand Dunes National Park, the actual western flank of the range is U.S. Forest Service and private land.

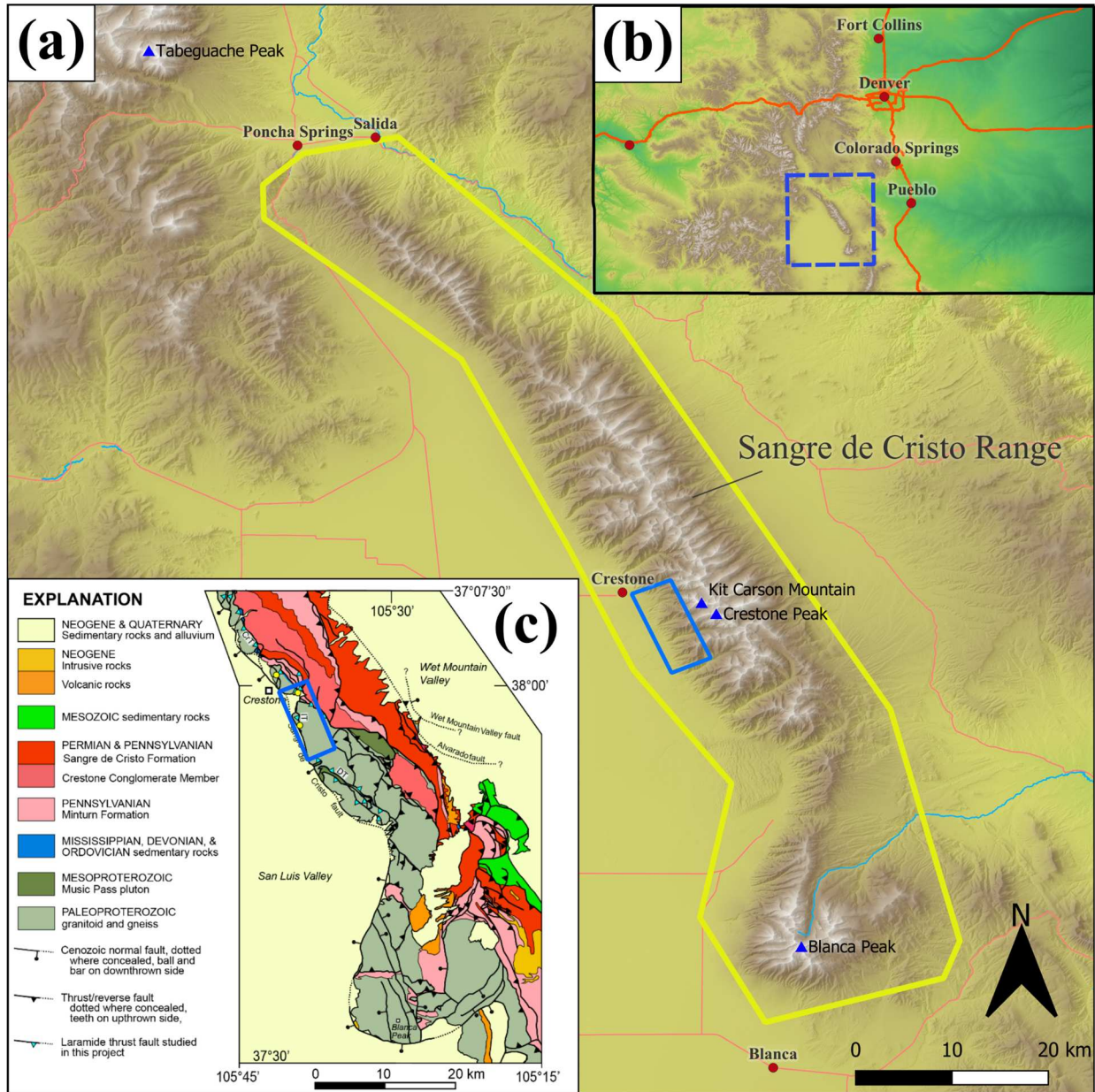


Figure 1: Maps providing an overview of the study area and its broader geographic and geologic context, with a hillshade and false-color elevation base map derived from USGS 1 arc second DEMs. (a) Map of the northeastern San Luis Valley, with the Sangre de Cristo Range and study area respectively outlined in yellow and blue. (b) Reference map of the state of Colorado, with the area of (a) outlined in blue. (c) Simplified geologic map of the Sangre de Cristo Range (modified from Johnson et al., 1969, and Lindsey et al., 1985, 1986b).

At the inception of this investigation, a primary ‘study area’ focused on the IMSZ was identified; this area was targeted for mapping, sampling, and all other analyses. The NW corner

of the primary study area is located 1.3 kilometers SE of Crestone, and the area is 11 km long and 4.5 km wide with a long axis bearing of 158° (Figs. 1, 2; Plate 1). Slopes along the range front in the study area are ubiquitously steep and rise from a basal elevation of around 7,900 feet on the alluvial plain of the San Luis Valley to maximum elevations of 12,100–12,400 feet along ridgelines at the northeastern edge of the area (Fig. 1, 2; Plate 1). The walls of the NE-SW-trending valleys that dissect the range (Fig. 1, 2, Plate 1) are steeper still, and time-efficient navigation on foot is generally restricted to ridgelines and valley bottoms (i.e., not valley walls) close to the northeastern edge of the area (Fig. 3; Plate 1). With the exceptions of cliffs, some S-facing valley walls, and areas above the timberline (~12,000 feet), the area is heavily vegetated (Figs. 2a, 2b), with grass and sagebrush dominant at lower elevations (~ 8,000 feet), juniper and piñon dominant at moderate elevations (~ 8,500 feet), and denser coniferous forests dominant at high elevations below timberline (~ 9,500–12,000 feet; McCalpin, 1981). The boundary of the Sangre de Cristo National Wilderness runs irregularly down the approximate center of the study area, and land to the SW is private and owned by an assortment of ranchers, homeowners, residential associations, and by various temples, ashrams, and religious centers.

The town of Crestone and other, since-abandoned settlements along the western flank the Sangre de Cristo Range originated during mining boom in the 1870s after the discovery of local vein-style Au-Cu deposits (Benson & Jones, 1996; Clement, 1952; Fauntleroy, 2013; Johnson et al., 1984). Mine workings and prospect pits are common where bedrock or subcrop appear in the study area, though they tend to be concentrated along apparent faults and shear zones which likely directed mineralizing fluid flow (Benson & Jones, 1996; Clement, 1952; Johnson et al., 1984). Individual prospectors and miners scoured the area from the 1860s until 1898, when a U.S. Supreme Court decision (Shaw v. Kellogg, 1898) granted exclusive mineral rights to the

owner of Luis Maria Baca Grant No. 4 (Fauntleroy, 2013), which includes all but the northern portion of the study area. Economic mineral exploration and extraction in the study area thereafter continued sporadically through the 1930s but was restricted to organized operators associated with established mines such as the Independent Mine (Clement, 1952; Johnson et al., 1984).

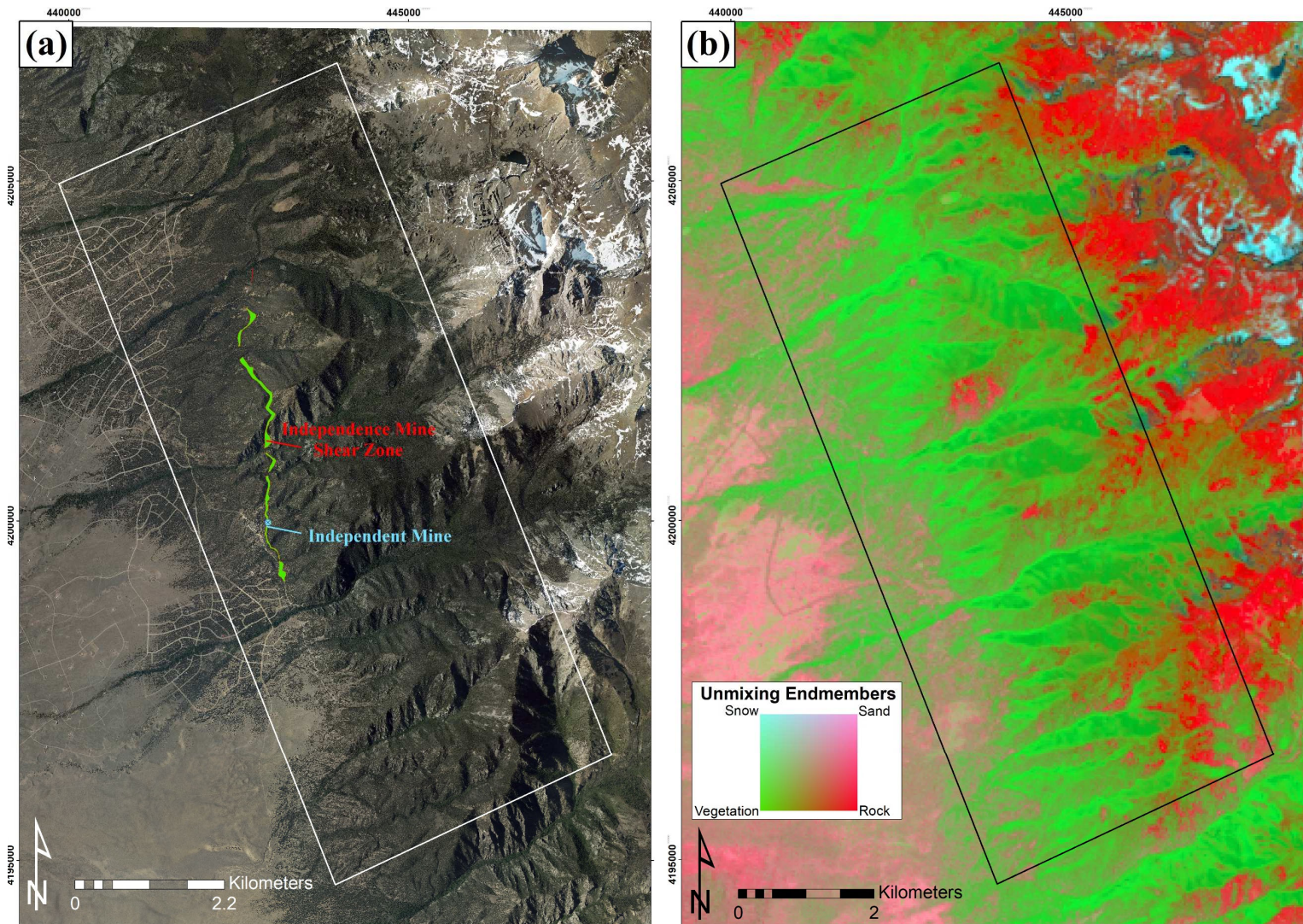


Figure 2. Map images of the study area and key features within it. (a) Bing maps satellite imagery of the study area, with the mapped IMSZ shown in green (area) and red (boundaries and presumed and/or concealed trace). (b) Land cover map of the study area, with land cover classifications derived from regression-based spectral unmixing of 30m resolution hyperspectral data from the PRISMA satellite, captured May 2022.

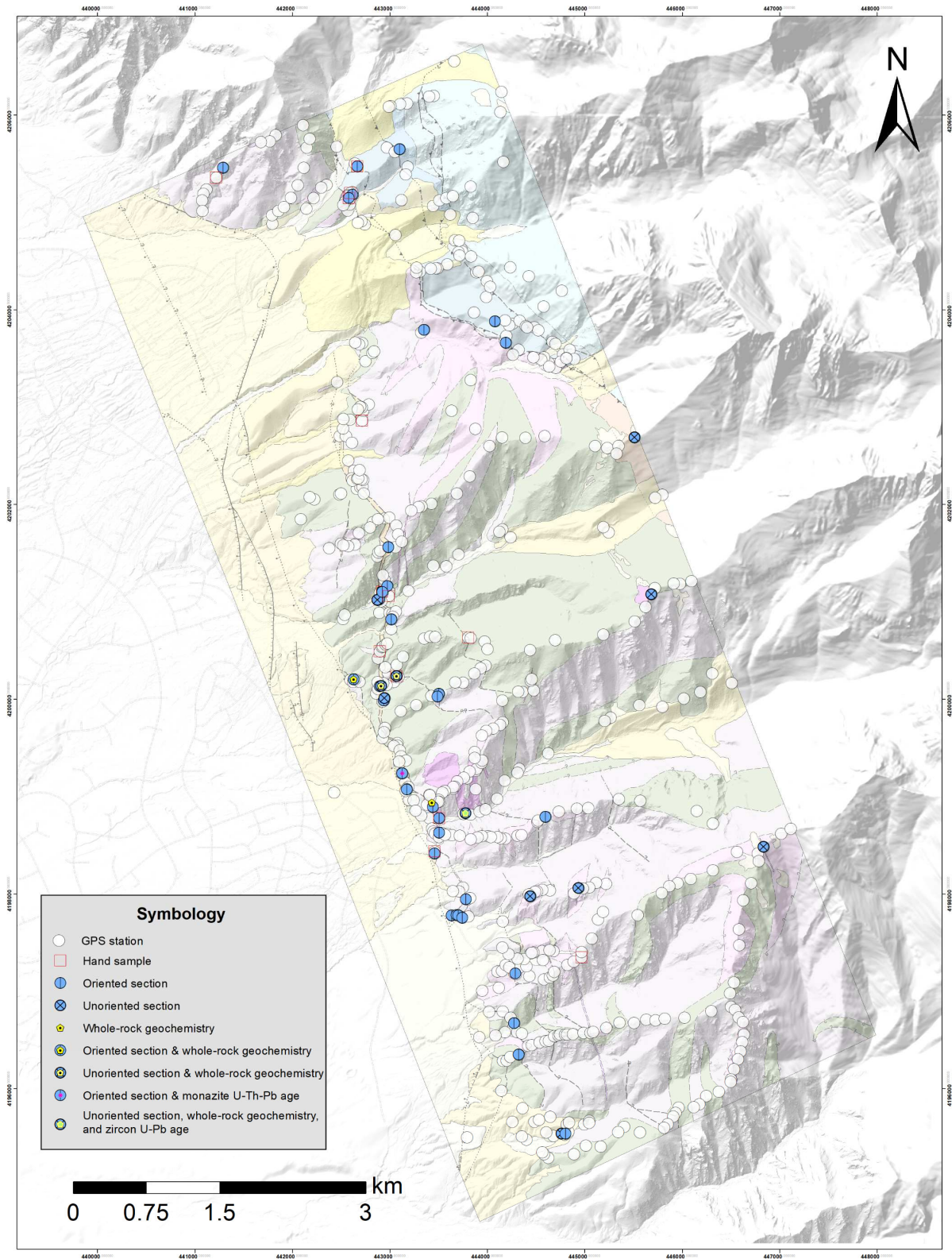


Figure 3. Map showing study area waypoint and sample coverage, with types symbolically differentiated. GPS station locations are available in Dataset 1, and sample locations are available in Dataset 2.

The Independent Mine is the type locality of the IMSZ and constitutes a pit and several shafts sunk into IMSZ mylonites on private land in the center-W part of the study area (Fig. 2a). Though it is variably referred to by previous workers as the “Independent Mine fault zone” (e.g., Clement, 1952) or as the “Independence Mine Thrust” (e.g., Lindsey, Johnson, et al., 1986), for the purposes of this study it will be referred to as the Independence Mine shear zone. The surface exposure of the IMSZ runs N-S for approximately 4.8 kilometers along the range front S and E of Crestone. Previous workers (Clement, 1952; Johnson et al., 1987; Lindsey, Johnson, et al., 1986) have mapped the IMSZ as being truncated by the Sangre de Cristo fault system at the southern terminus of its exposure, and both Lindsey et al. (1986) and Johnson et al. (1987) interpreted the IMSZ to be truncated by a concealed thrust fault at the northern terminus of its exposure.

1.2. Geologic Setting

The Sangre de Cristo Range has a long, complex, and variably well-understood geologic history. Rocks in the Sangre de Cristo Range and in the study area (e.g., Fig. 4) record local and regional deformational events spanning from the Paleoproterozoic to the present (Hoy & Ridgway, 2002; Jones & Connelly, 2006; Lindsey et al., 1984; Lindsey, 2010; McCalpin, 1981).

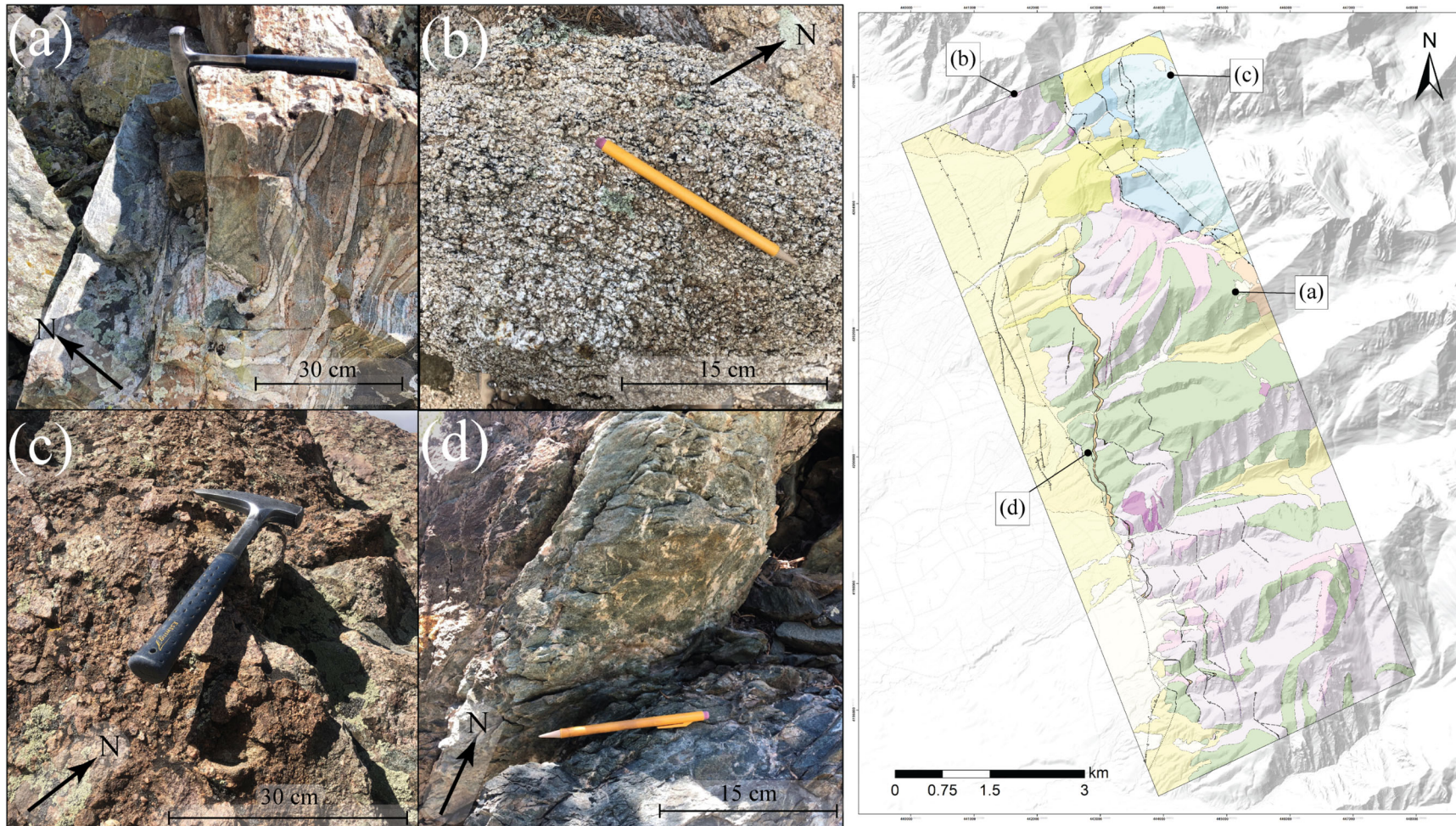


Figure 4. Photographs showing representative outcrops of various units in the study area, with photo locations shown on reference map (at right). (a) Proterozoic amphibolitic gneiss (Xga). (b) Mesoproterozoic Crestone quartz monzonite (Ycqm). (c) Crestone conglomerate member of the Sangre de Cristo Formation (PPsc). (d) Independence Mine shear zone (Tcm).

1.2.1. Proterozoic

The oldest rocks in the range are comprised of interleaved Paleoproterozoic amphibolite and quartzo-feldspathic gneisses (Fig. 4A) that have been interpreted as interlayered basalts, felsic lavas, and volcanoclastic sediments that underwent amphibolite-facies metamorphism based on sharp, albeit complexly deformed, compositional boundaries (Jones & Connelly, 2006; Reed, 1984). The age of these gneisses vary within the range (Jones & Connelly, 2006); amphibolite near Blanca Peak is constrained to pre-1750 Ma by on a 1749 ± 4 Ma zircon U-Pb age for the intruding Blanca suite (Sabin, 1994), but a metarhyolite constituent of the gneiss at the northern end of the range dates to 1728–1713 Ma (Bickford et al., 1989). The gneisses and amphibolite throughout some of the range exhibit steeply-dipping, NW-trending fabrics and isoclinal folds (Fig. 4A). These are interpreted to record strain associated with the amalgamation of the Yavapai province between 1750 and 1710 Ma (“D₁”, per Jones & Connelly (2006)). This deformation event was followed by regional emplacement of felsic intrusions such as the Crestone quartz monzonite (Fig. 4B) prior to a deformational event that produced localized NE-SW-trending fabrics in the range and has been interpreted to represent the late stages of the Mazatzal orogeny (“D₂”, per Jones & Connelly (2006)). A subsequent tectonic lull spanning into the Mesoproterozoic was broken by the emplacement of the coarse-grained A-type Music Pass quartz monzonite at 1434 ± 2 Ma (zircon U-Pb; Jones & Connelly, 2006) and shortly thereafter by an additional, poorly-understood deformational event that produced NE-SW-trending folds and subvertical mylonitic fabrics in both Paleo- and Mesoproterozoic units (“D₃”, Jones & Connelly, (2006)).

1.2.2. Paleozoic

The area of the modern Sangre de Cristo Range is interpreted to have experienced relative tectonic quiescence through the early Paleozoic, and a succession of units including the Ordovician Harding Formation and the Mississippian Leadville Formation were deposited during two of several periods of marine deposition, punctuated by episodes of subaerial erosion (Clement, 1952; Lindsey, 2010). Late Paleozoic rocks in the range, however, provide a uniquely complete record of the elsewhere sparsely-preserved uplift and erosion of the Ancestral Rocky Mountains (ARM) (Hoy & Ridgway, 2002; Lindsey, 2010). During Pennsylvanian-Permian time, the contemporary Sangre de Cristo Range was the location of the Central Colorado Trough, which was a depositional basin bounded by the Uncompahgre uplift to the SW and by the Ancestral Front Range to the NE (Hoy & Ridgway, 2002; Sweet et al., 2021). The Pennsylvanian Minturn Formation (~2000 m-thick at type-locality; (Lindsey, et al., 1985)) and Pennsylvanian-Permian Sangre de Cristo Formation (~200–1500 m-thick; Hoy and Ridgway, 2002) were deposited in the Central Colorado Trough. An upward-coarsening trend in these units (Fig. 4c) provides evidence for the relatively rapid exhumation and beveling of the Uncompahgre uplift: marine shales and sandstones of the Minturn Formation grade into the sandstones and conglomerates of the Sangre de Cristo Formation (Hoy & Ridgway, 2002; Johnson et al., 1987; Lindsey, 2010). This trend culminates in the Crestone Conglomerate (Fig. 4c; Plate 1), which is the upper mega-conglomerate member of the Sangre de Cristo Formation and reflects extremely rapid and proximal unroofing of the crystalline basement of the Uncompahgre uplift (Hoy & Ridgway, 2002; Lindsey, 2010). The upper Paleozoic units of the Sangre de Cristo Range also preserve several primary ARM structures (Hoy & Ridgway, 2002), which are rare elsewhere (Sweet & Soreghan, 2010). These structures are generally consistent with NE-SW shortening

(Hoy & Ridgway, 2002; Sweet et al., 2021) and include the NW-SE trending Gibson Peak growth syncline within the Sangre de Cristo Formation to the NE of the study area and the Sand Creek thrust, which is reportedly well-exposed to the S of the study area (Fig. 2a; Hoy & Ridgway, 2002). The Gibson Peak syncline has been interpreted to record Pennsylvanian-Permian syndepositional shortening along the Crestone thrust (Plate 1) at the northeastern margin of the Uncompahgre uplift and thus suggests that some thrust faults that later accommodated Laramide shortening originated during ARM-related shortening (Hoy & Ridgway, 2002). Such reactivation appears to have been localized. An apparent overlapping relationship between the upper Sangre de Cristo Formation and the Sand Creek thrust, identified by Hoy and Ridgway (2002), suggests that this fault was likewise involved in early-middle ARM shortening but was not reactivated during the Laramide orogeny. Some researchers (e.g., Lindsey, 1986; Lindsey et al., 2010) have interpreted the Sand Creek thrust system as being contiguous with the Deadman Creek thrust fault to the SW (e.g., Fig. 5). A synthesis these prior (and possible irreconcilable) interpretations would suggest that the Deadman thrust fault itself originated in the Paleozoic.

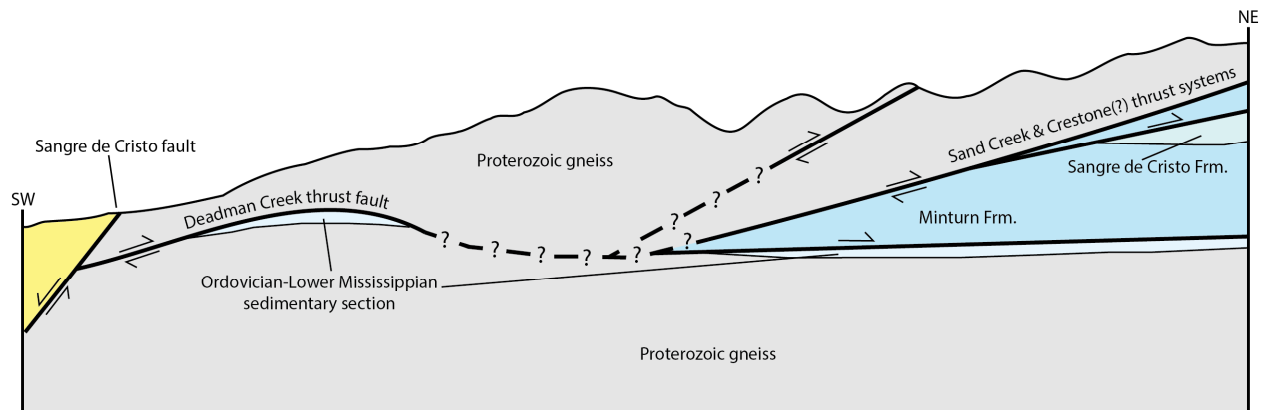


Figure 5. Schematic cross section showing the broad structural geology of the western flank of the range in the vicinity of the map area, as interpreted by various previous workers (e.g., Clement, 1952; Lindsey et al., 1986, 2010). Correlation between the Deadman Creek thrust fault and thrust systems further to the NE (i.e., Sand Creek and Crestone thrust systems) is notably not examined in the present study.

1.2.3. Mesozoic

In the early to mid-Mesozoic, the area of the Sangre de Cristo Range was likely the site of some renewed deposition. Exploratory drillholes have been reported to intersect preserved sections of subaerial and marine (i.e., Interior Seaway) units such as the Morrison and Mancos formation at depths of over a mile below the surface of the northeastern San Luis Valley (Hoey et al., 2006; Watkins, 1996). Some industry reports (i.e., Hoey et al., 2006; Watkins, 1996) also note two small outcrops of interpreted Mesozoic sediments preserved at the bottoms of alluvial washes off the range front within the southwestern corner of the study area (Plate 1); these exposures were not identified during mapping. Mesozoic deposition in the area probably ended with the onset of local deformation associated with the Laramide orogeny, as recorded by the contemporaneous sedimentary record in the Raton basin to the E of the range (Bush et al., 2016; Cather, 2004; Lindsey, 1998). Surface uplift may have begun as early as 80 Ma but certainly before 70 Ma (Bush et al., 2016; Cather, 2004). During the Laramide, the present southwestern flank of the Sangre de Cristo Range was located near the eastern margin of the San Luis uplift and has been interpreted as accommodating spatially-variable, kilometer-scale shortening along W- to SW-dipping thrusts and reverse faults such as the Deadman Creek thrust and the reactivated Crestone thrust (Plate 1; Bush et al., 2016; Hoy & Ridgway, 2002; Lindsey, 2010; Tweto, 1975). Laramide slip histories for these faults have been interpreted largely based on indirect evidence, though NE-vergent thrust faults along the eastern flank of the range locally involve Mesozoic sedimentary units (e.g., the Loco Hill and Spread Eagle thrusts; Hoy and Ridgway, 2002). The IMSZ (Plate 1; Fig. 4a) may have originated contemporaneously as the mid-crustal counterpart of a similarly-oriented thrust/reverse fault (Hoy and Ridgway, 2002; Lindsey et al., 2010).

1.2.4. Cenozoic

Based on the sedimentary record in the Raton Basin, Laramide uplift likely continued into the Early Eocene and was followed by a period of erosional beveling (Bush et al., 2016; Cather, 2004). Subsequent development of significant paleotopography associated with the Rio Grande Rift at the site of the modern Sangre de Cristo Range is constrained by Oligocene volcanic and volcanoclastic deposits (Brister & Gries, 1994; Cather, 2004; Lipman, 1989). These deposits include the 28 Ma Fish Canyon Tuff, which was erupted from the La Garita Caldera to the W of the present Sangre de Cristo Range but also crops out along the western flank of the Wet Mountains to the E of the range (McIntosh & Chapin, 2004; Steven & Lipman, 1975). Further evidence from volcanic deposits (e.g., < 26.8 Ma Hinsdale Formation basalt flows which unconformably cover earlier Oligocene ash deposits; Lipman, 1975; Brister & Gries, 1994) suggests that extensional development of the San Luis Basin to the N and W of Blanca Peak may have begun ca. 27 Ma. $^{40}\text{Ar}/^{39}\text{Ar}$ dates for plutonic and volcanic rocks represented as clasts in basal syn-rift sediments indicate a slightly younger (~25 Ma) initiation of rift-related extension in the Culebra embayment to the S of Blanca Peak (Wallace, 2004). Apatite low-temperature thermochronology data (i.e., fission track from Kelley et al., 1992 and Lindsey et al. (1986), and (U-Th)/He from Ricketts et al. (2016)) from the Sangre de Cristo Range itself, though complex and at times mutually inconsistent, also broadly suggest an onset of extensional unroofing between ~27 Ma and ~25 Ma. Some workers interpret relatively slow extension prior to an increase in exhumation rates at some point in the Early to Middle Miocene (at ~19 Ma based on AFT ages (Lindsey et al., 1986); at ~15 Ma based on comparisons between $^{40}\text{Ar}/^{39}\text{Ar}$ ages for volcanic units near the valley floor versus those found at higher elevations in the Culebra Range (Miggins et al., 2002)). Abbey and Niemi (2020) identify spatial variability in exhumation rates

during the first 10–15 Ma of rifting through (U-Th)/He thermochronology and propose that this corresponded to a period of progressive fault initiation and linkage.

Rio Grande rift extension along the northeastern flank of the range was partially accommodated along the Alvarado fault, which likely originated as a Laramide thrust fault prior to normal-sense reactivation (Lindsey et al., 1984). Faults along and off the SW flank of the range have since accommodated up to ~9 km of normal-sense vertical separation, with the majority of this separation accommodated along the range-bounding, moderate to high angle (~45–60°) Sangre de Cristo fault system and geometrically similar buried normal faults (Kluth & Schaftenaar, 1994; Grauch et al., 2013). Relatively well-defined fault scarps in Quaternary sediments indicate that extension along the Sangre de Cristo fault system has continued into the Holocene (McCalpin, 1981; Ruleman & Brandt, 2021). Other higher- and lower-angle SW-dipping normal faults have been noted or proposed along the southwestern flank of the range (Benson & Jones, 1996; Caine et al., 2013; Hoey et al., 2006; Watkins, 1996), but their significances in accommodating Rio Grande rift-related extension are unclear. The role played by pre-existing thrust faults along the southwestern flank of the range during Rio Grande rifting is likewise poorly understood, though some workers have interpreted rift-related reactivation of Laramide thrusts to the N (Fletcher et al., 2006) and S (Caine et al., 2017; Lisenbee, 2013) of the study area.

The Sangre de Cristo Range was intermittently glaciated in the Pleistocene, and moraines and glaciofluvial deposits from the Bull Lake (penultimate glacial maximum) and Pinedale (last glacial maximum) glaciations are well-preserved along the southwestern flank of the range (Plate 1; Leonard et al., 2017; McCalpin, 1981; Ruleman & Brandt, 2021). Local glacial deposits are underlain, overlain, and intermingled with various Quaternary fan deposits (Plate 1) which have

been shed from the range to fill the San Luis Valley (McCalpin, 1981; Ruleman & Brandt, 2021). Prior to ~500 ka these fan sediments were deposited along the shores of and into Lake Alamosa, which filled the San Luis Valley; eolian sand originally sourced from the dry lakebed now forms the dunes and dune fields along the range front (Lindsey, 2010; Madole et al., 2008).

1.3. Prior Work

Though earlier, extremely small-scale geologic maps encompassing the study area exist (Hayden, 1877), the bedrock of most of the area was first mapped and studied in detail by Clement (1952) as part of a survey of the geology of the Luis Baca Grant No. 4. Lindsey et al. (1984, 1985) achieved complete geologic map coverage of the study area and much of the Sangre de Cristo Range, albeit with less detail (1:24,000 scale) than Clement (1952). Johnson et al. (1987) produced a lower-resolution (1:62,500 scale) geologic map encompassing the study area. Some more recent studies have included schematic or semi-schematic maps of various aspects of the study area's bedrock geology (e.g., Proterozoic units from Jones & Connelly (2006); Paleozoic units from Hoy and Ridgway (2002)) or of the bedrock geology of adjacent areas (e.g., the Deadman Creek area from Weigel (2014)). McCalpin (1981) produced the first maps focusing specifically on the geomorphology and Quaternary geology of the area, and further geomorphological mapping of the area has since been published by Ruleman et al. (2021). The work of Leonard et al. (2017) includes some mapping of moraines within the study area.

Several researchers have published geophysical surveys and interpretations thereof focused on rift-related faulting in the subsurface of the San Luis Valley to the W and SW of the study area. These include studies by Kluth & Schaftenaar (1994; seismic surveys due W of the study area), Brister and Gries (1994; seismic survey and borehole log interpretation to the S and

SW of the map area), Magnani et al. (2005; seismic surveys in northern New Mexico), Grauch et al., (2013; aeromagnetic surveys W of Blanca peak), and Drenth et al. (2019; gravity, aeromagnetic, and magnetotelluric data to the southwest of the study area). Additional, apparently proprietary, exploratory seismic survey lines immediately adjacent to the study area are noted by Watkins (1994), and data from several more distal lines are included as figures by Hoey et al. (2006). Seismic interpretations by Watkins (1994) and Hoey et al. (2006) of an interpreted, buried low-angle normal fault accommodating substantial extension to the SW of the study area have notably been challenged by other workers (e.g., Caine et al., 2013).

As noted in Sections 1.2.1 and 1.2.4, many researchers have published geo- and thermochronology results from rocks found within and surrounding the study area (Bickford et al., 1989; Jones & Connelly, 2006; Kelley et al., 1992; Lindsey et al., 1986; Lipman, 1989; Ricketts et al., 2016). Lindsey, et al. (1986) notably also use conodont alteration indices within Paleozoic units to estimate peak burial temperatures of up to 300 °C along the southwestern side of the Sangre de Cristo Range. Highly localized areas of Paleozoic section along the southwestern side of the range were heated to temperatures up to ~500 °C through mid-Cenozoic contact metamorphism (Malavarca et al., 2022). Additional relevant thermochronological studies from Sanders et al. (2006) and Miggins et al. (2002), respectively, use $^{40}\text{Ar}/^{39}\text{Ar}$ dating of rocks from the Sangre de Cristo Mountains of northern New Mexico to provide evidence for late Proterozoic unroofing, and to reconstruct exhumation rates in the Oligo-Miocene. Newer (U-Th)/He thermochronology work from Abbey & Niemi (2018, 2020) suggests progressive development of range-bounding extensional fault systems in both the Arkansas River valley and the northern San Luis valley, with timing for the latter largely in line with work by earlier researchers (Lindsey et al., 1986; Ricketts et al., 2016). Zircon U-Pb geochronology from Holm-

Denoma et al. (2019) indicates Late Oligocene ages (i.e., 27–28 Ma) for some dikes along Deadman Creek, just to the S of the study area (e.g., Plate 1). ^{10}Be cosmogenic exposure dating of moraine deposits by Leonard et al. (2017) places various age constraints on the extent of glaciers that retreated after the last glacial maximum within the study area itself.

The general economic geology of the study area and nearby areas of the Sangre de Cristo Range is described by Clement (1952). Later investigations by the USGS and US Bureau of mines (Ellis et al., 1983; Johnson et al., 1984; digitized by Caine et al., 2021) provide thorough assay-sample coverage of the Sangre de Cristo Range including parts of the study area and reveal scattered areas of Au-Ag-Cu mineralization both near Crestone and broadly along the length of the Sangre de Cristo fault. Benson & Jones (1996) conducted a detailed investigation of the San Luis gold deposit (~10 miles S of Blanca; Fig. 1) and concluded that local Au mineralization is associated with a low-angle, SSW-dipping brecciated “detachment fault” and probably genetically related to small-volume felsic intrusions in the area.

1.4. Research Objectives and Relevance

One major objective of this study was to produce a detailed (1:10,000 scale) geologic map of bedrock and relevant surficial units within the study area (Plate 1). This objective was important in of itself – published bedrock maps of the area were generally made without the benefit of recent advances in mapping technology (e.g., GIS, GPS, lidar DEM data, etc.) and at too small a scale to resolve some structural details of the area (e.g., the map thicknesses of individual shear zones). Detailed geologic mapping and concurrent structural data collection were also crucial to achieving another goal of the study: in-depth characterization of the IMSZ and related structures. Said characterization included determining the orientation, thickness, length, outcrop-scale kinematic indicators, and structural context of each major structure through

mapping and close examination of outcrops. This study additionally sought to use geo- and thermochronology to establish how and when local shear zones (e.g., the IMSZ) originated, and to identify evidence or a lack thereof for their reactivation. Synthesis of the aforementioned spatial and geologic data is necessary to answer one of this study's primary research question: what were the controls on observed extensional, mid-crustal reactivation of local thrust faults?

2. METHODS AND MATERIALS

A variety of field-based, lab-based, and computational techniques and methodologies were used to characterize the structural geology of the study area and to evaluate the kinematics, rheological properties, and timing of the brittle-plastic shear zones within it. These methods are described in the following section.

2.1. Geologic Mapping

Structural orientation data were collected in the field using, in order of decreasing prevalence: the *Fieldmove Clino* iPhone app (Vaughan et al., 2014), the *Stereonet Mobile* iPhone app (Allmendinger et al., 2017), and an analog Brunton compass. Structural data, paper field notes, and digital (i.e., in *Fieldmove Clino*) notes were generally geolocated to waypoints captured on a handheld GPS unit (Dataset 1). Some structural data and notes were geolocated to *Fieldmove Clino* “Localities,” but GPS waypoints were used wherever possible due to their higher spatial accuracy (Dataset 1). Mobile apps were run on an Apple iPhone X, and manual inclinometer-magnetometer calibration was done prior to collecting data as per the best practices outlined by Allmendinger et al. (2017). Some gneissic amphibolite outcrops were found to contain sufficient magnetite to skew digital and analog structural orientation measurements; a crude check (i.e., waving a Brunton compass or mobile device in front of outcrops) was conducted at each amphibolitic outcrop to verify a probable lack of magnetitic skew, and orientations on multiple planes within an area of $\leq 10 \text{ m}^2$ were generally collected at outcrops of gneissic rocks to mitigate the potential impact of unidentified magnetite. Contacts were drawn in the field using either *TouchGIS* (Touch GIS LLC, 2021) or *Fieldmove Clino* (Allmendinger et

al., 2017) at some locations where geologic contacts and structures could be seen from afar, but, owing to the complexity of the local geology and widespread vegetation cover (e.g., Fig. 2), an approach of recording notes and GPS waypoints while walking contacts or features and then interpolating features later (i.e., “waypoint mapping”) was usually adopted. A total of 1256 raw structural orientations, divided between 322 geolocated stations, were collected during the mapping process (available in Dataset 3), and notes, photos, or samples were collected at an additional 245 stations (Fig. 3). At exposures of shear zones and small-scale scale fault planes, these notes include kinematic indicators (e.g., C’ shear bands, quartz slickenfiber steps) and assessments of shear/slip sense with confidence values (0–3) assigned to each assessment.

The main map product (Plate 1) for this study was constructed in *ArcMap* using the GeMS schema and its ArcPy toolkit (Thoms et al., 2017/2022; U.S. Geological Survey National Cooperative Geologic Mapping Program, 2020). A 1 m-resolution DEM was built from various USGS 3DEP Lidar point-cloud files from in and around the study area using *whiteboxtools* (Lindsay, 2014) and combined with a USGS 3DEP 1/3rd arc-second DEM to obtain a basemap for the study area with maximum-available spatial resolution (i.e., Plate 1). Other human-geographic basemap data (e.g., streets, rivers, etc.; Plate 1; Fig. 1) were downloaded from OpenStreetMap (OpenStreetMap contributors, 2017). Relatively low-resolution (400 m line spacing) aeromagnetic data covering the study area were obtained through the USGS (U.S. Geological Survey, 1983), and high-resolution RGB satellite orthoimagery for the study area (e.g., Fig. 2A) was downloaded from Bing maps. The aforementioned data were referred to when interpolating contacts and structures between areas that were accessible and/or visible on foot, with DEM and aeromagnetic datasets used in particular when mapping fault scarps through Quaternary units along the range front.

Geolocated structural data from the field investigation were compiled from field notebooks and various apps using a Python script. Per-station, per-structure eigenvector best-fit solutions (e.g., Allmendinger et al., 2013) were automatically calculated within the script using the *mplstereonet* Python package (Kington, 2012/2020) for all structures save joints, individual fault planes, and gneissic foliation with outcrop-scale folding. Eigenvector-best-fit data were plotted on the map (i.e., Plate 1) and are presented here where average orientations might reasonably be expected to be more robust than individual datapoints, such as in the cases of gneissic foliation (often irregular and susceptible to local skew from magnetite) and of crudely-developed bedding in the Sangre de Cristo Formation. These data are made available in Dataset 4.

Sampling for petrographic and/or microstructural analyses, in-situ geochronology, and electron backscatter-diffraction (EBSD) was conducted throughout the study area, with oriented samples collected where appropriate, such as in shear zones (Fig. 3; Dataset 2). Oriented petrographic section billets were generally cut parallel to mineral lineations and perpendicular to foliations to obtain X-Z sections for microstructural analysis. Petrographic sections were prepared from the cut billets by Paula Leek Petrographics. Polished thin sections and thick sections were respectively prepared from billets that appeared viable for EBSD and/or monazite geochronology and for billets that contained potentially datable (U-Pb LA-ICP-MS) syn-kinematic calcite veins; covered thin sections were prepared from all other billets. Bulk sampling (i.e., ~500-mL to ~3 liters of material) was conducted at several stations for zircon U-Pb LA-ICP-MS geochronology, whole-rock geochemistry, or both (Fig. 3).

2.2. Geospatial Analyses

A hyperspectral dataset encompassing the study area was obtained through the Italian Space Agency (ASI) via the PRISMA satellite (239 visible to SWIR bands; 30 m spatial resolution) and analyzed in QGIS using the regression-based spectral unmixing tools of the EnMAP-Box plugin (EnMAP-Box Developers, 2019; Fig. 2B). Two different spectral unmixing analyses were attempted, each with different aims. In one analysis, averages of approximate representative landcover (i.e., vegetation, rock, sand, and snow; Fig. 2B) pixels from the PRISMA dataset itself were used as unmixing endmembers, with a simple landcover map potentially useful for identifying lineaments not visible in RGB imagery as a target product. In the other analysis, sets of potentially distinct rock and mineral spectra from published spectral libraries (Baldrige et al., 2009; Kokaly et al., 2017; Meerdink et al., 2019) were used as endmembers, with an approximate lithologic map resolving important bedrock characteristics and structures (e.g., estimated gneiss mineralogy, areas rich in Fe-oxide minerals, and/or traces of chlorite-rich shear zones) as a target product. Of the two target map products attempted using spectral unmixing of PRISMA data (Sect. 2.3), only the first (a map of landcover in the study area; Fig. 2B) was achieved. Some limited success was achieved in separating the most laterally extensive exposures of chlorite mylonite within the study area (e.g., the IMSZ along Spanish Creek; Plate 1) from surrounding bedrock. Broadly, however, complications arising from the relatively low spatial resolution of the PRISMA dataset, widespread vegetation coverage, and shadows produced by the range's highly irregular topography precluded resolution of compositional differences between bedrock units via unmixing.

Approximate estimates of minimum displacements for shear zones with extensional shear sense were calculated from compiled structural and spatial (i.e., map geometry) data using a

semi-automated adaptation of a method originated by Ramsay & Graham (1970) and described by Allmendinger (2015; p. 191-194). The mapped traces of shear zones and faults within the study area were first broken up into ~500–1000 m-long segments, and the orientations of these segments were calculated using a custom Python-based QGIS tool for solving three-point problems given elevation data from a basemap DEM. A representative thickness for each shear zone segment was then either manually calculated based on mapped shear zone boundaries, calculated shear zone orientation, and DEM-derived elevation data or, in the cases of sub-map-scale shear zone thicknesses, entered from field observations. Orientations and thicknesses were in turn combined with raw structural data (i.e., mylonitic foliations and lineations) geo-located within the shear zone segments and with per-waypoint eigenvector best-fits of these structural data. The resulting dataset was exported and run through a Python script to iteratively a) calculate local estimated shear direction orientations and shear zone displacements and b) save equal area stereonet plots of relevant data for manual verification of results. ‘Movement plane’ orientations were calculated for each waypoint; these planes were calculated as being perpendicular to the intersection lines between shear zone margins and average local mylonitic foliation. Linear ‘shear directions’ were interpreted for each waypoint at the intersections between movement planes and shear zone margins. Ideal ‘X-directions’ were additionally calculated for verification purposes as intersections between movement planes and waypoint-average mylonitic foliation. Estimated shear-strain-only displacements (d) were calculated using Equations 1 and 2 from Ramsay & Graham, 1970), where γ is the shear strain, θ' is the angle between the average local mylonitic foliation and the calculated shear zone margin orientation, and z is the shear zone thickness:

$$\gamma = \frac{2}{\tan 2\theta'} \quad (1)$$

$$d = z * \gamma \quad (2)$$

These calculations require several assumptions, including: a) foliation planes originally formed to accommodate normal-sense shear and are relatively unaffected by back-rotation related to C' shear bands, b) foliation planes rotated towards shear zone boundaries entirely through simple shear, c) strain was homogenous throughout the shear zones and d) foliation and shear zone boundary estimates are accurate and representative. The first assumption is likely to be false for most of the shear zones studied given the prevalence of macro-scale fabrics indicating past reversal of shear direction and of C' shear bands, and the following two are likely gross oversimplifications. Cases where the final assumption may have been incorrect were controlled for via filtering based on comparisons between orientations of ideal (projected) X-directions and those of actual mylonitic lineation measurements from the waypoint in question (where available) or from other nearby waypoints along the same shear zone. Calculations were deemed 'invalid' and filtered out of the dataset where X-directions did not trend within 10° of the actual, measured mylonitic lineations.

2.3. Microstructural Analysis

Microstructural kinematic indicators in oriented petrographic thin and thick sections cut from rocks within shear zones (e.g., S-C fabrics, C' shear bands, antithetic brittle fracturing with domino-style block rotation, shearing of veins, oblique subgrain and recrystallized grain orientations in quartz ribbons) were catalogued to record confidence-rated probable senses of shear. The modal percentage and dominant mineralogy of phyllosilicates present were also estimated for each sample and recorded along with the apparent interconnected weak phase in

the section. Estimates of phyllosilicate modal percentages were in some cases obtained directly from quantitative mineralogical analyses from a TESCAN system at the Colorado School of Mines. Microstructural kinematic interpretations for each oriented sample referred to in this text are available in Dataset 2.

Five quartz-rich polished, oriented petrographic thin sections were subjected to electron backscatter diffraction (EBSB) analyses by Dr. Jeffrey Rahl at Washington and Lee University. Thin-sections were polished using a colloidal silica slurry and analyzed using a Zeiss EVO MA 15, Scanning Electron Microscope SEM operating in low-vacuum at an accelerating voltage of 25 kV, a probe current of 20–25 nA, and a working distance between 15 and 25 mm. Step sizes between 0.5 and 20 μm were chosen on a sample-to-sample basis at the discretion of Rahl.

2.4. Geochronology and Thermochronology

Two igneous rock samples were analyzed via zircon U-Pb geochronology and zircon fission-track thermochronology in this study, with all steps (including mineral separation) handled by GeoSep Services and Dr. Paul O’Sullivan. These data are included in dataset 5. Inverse modelling of fission-track-based thermal histories using the resulting data was done via HeFTy (Ketcham, 2005).

Seven polished thick sections of rocks from shear zones in the study area that include probable synkinematic to late-synkinematic calcite veins were analyzed via LA-ICP-MS at the UC Santa Barbara petrochronology facility in an attempt to constrain their latest shearing with calcite U-Pb dates. Between 27 and 70 100- μm diameter spots were analyzed in each sample, with spots placed in multiple kinematically-involved veins where possible. Analysis was conducted using a Photon Machines excimer 193 nm laser equipped with a HeIEX cell and a Nu

Instruments Plasma 3D multicollector ICP with a Daly array. NIST glass standard N614 was used as a primary reference, and with secondary calcite references of WC1, ASH15, and AUG-B6 and “Mud Tank” as a secondary zircon reference (Horstwood et al., 2016; Rasbury et al., 2021; Roberts et al., 2017). Data reduction was completed by Andrew Kylander-Clark using the Iolite software package (Paton et al., 2011). These data are available in Dataset 6.

Small ($\leq 30 \mu\text{m}$) grains of probable synkinematic to late-synkinematic monazite were identified in two polished thin sections from study area shear zones via TESCAN analysis at the Colorado School of Mines followed by reflected-light petrographic examination. These grains were dated via U-Th-Pb LA-ICP-MS analysis at UCSB with a spot size of $7 \mu\text{m}$ used to maximize the number of spots and grains datable in each section. Analysis was completed using a Photon Machines excimer 193 nm laser with a HeEX cell, Nu Instruments Plasma HR-ES multi-collector ICP (for U, Th, and Pb isotopes) and an Agilent 7700x quadrupole ICP-MS (for REEs, Y, and Si). Initial data reduction was completed by Andrew Kylander-Clark using Iolite (Paton et al., 2011). IsoplotR (Vermeesch, 2018) was used to calculate various radiochronometric ages from LA-ICP-MS data, as well as to create plot figures (e.g., concordia diagrams) displaying these data, which are available in Dataset 7.

2.5. Whole Rock Geochemistry

Twelve samples (eight of mylonitic shear zones, three of host rock locally surrounding shear zones, and one of an apparently hydrothermally-altered “transition zone” between host rock and chlorite mylonite) were collected from the field area to aid in interpretation of likely-hydrothermal alteration affecting shear zones. All samples were chipped on a steel plate using a sledgehammer, with numerous layers of newspaper and Ziploc bags separating samples from steel surfaces. Chips displaying apparent weathered surfaces or (unrepresentative) metasomatic

veins (i.e., of calcite or epidote) were discarded after initial chipping. An initial batch of six samples was subsequently subjected to further rounds of sledge-plate crushing until ~20 mL of fine powder was available for analysis. Larger sample volumes were obtained for a second batch of six samples: ~ 300–500 mL of sorted chips from each of these samples were powdered using a shatterbox, the resulting powder was mixed by hand to achieve some degree of homogenization, and ~50 mL of powder was selected for analysis. Powders were sent to ALS Minerals in Reno for whole rock geochemical analysis (i.e., fused bead, acid digestion, ICP-MS or ICP-AES depending on target element). Whole-rock geochemical data for all analyzed samples are available in Dataset 8.

3. RESULTS

As previously noted, investigative work involved in this study included new geologic mapping as well as lab-based and computational analyses of samples and data collected during said geologic mapping. The initial subsections of this text (i.e., Sects. 3.1 and 3.2) consequently describe the units and structures within the study area, with results from further analyses provided in later subsections (i.e., 3.3 and beyond).

3.1. Geologic Units

3.1.1. Proterozoic Units

Proterozoic basement rocks of the study area were separated into five subunits, described below. The former three units are found throughout the study area and are generally intermingled on a cm to m-scale. Areas where each appears to be compositionally dominant over the other two (i.e., in compositional plurality) have been separated in the map of the area (i.e., Plate 1) based on field observations of outcrop. Given the extreme complexity of actual outcrop-scale intermingling within the basement and dense vegetation cover in much of the study area, contacts between these units in most areas should be considered approximate, increasingly so with greater distances from transects covered on foot (i.e., Fig. 3).

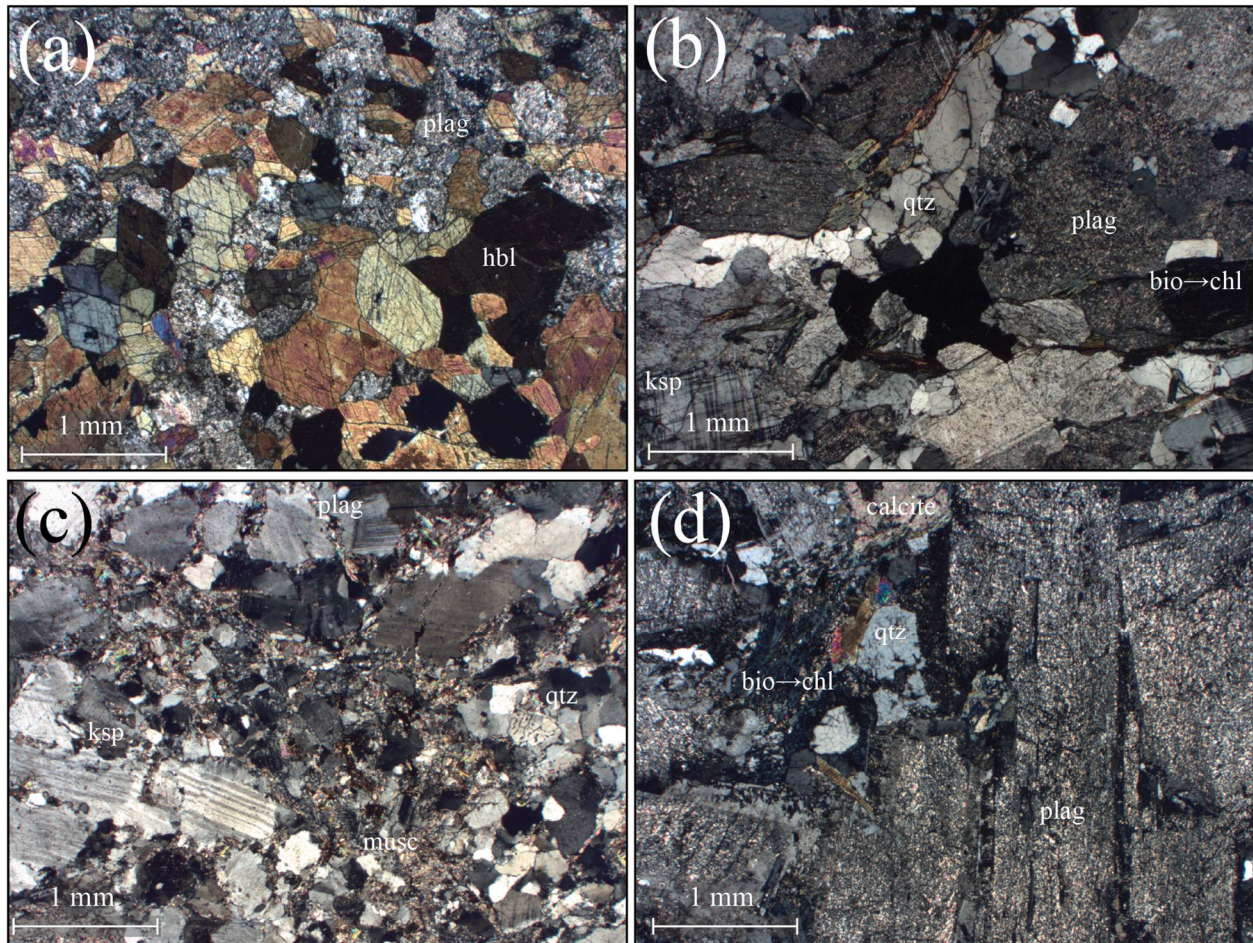


Figure 6. Representative photomicrographs of Proterozoic basement (a-c) and a poorly constrained crystalline units found in the map area (d). (a) Gneissic amphibolite (Xga), with the primary compositional-penetrative foliation dipping steeply to the left, intersected by an additional penetrative foliation defined by elongate hornblende crystals. (b) Quartzofeldspathic gneiss (Xqfg), with the primary compositional-penetrative foliation oriented horizontally, with an additional, oblique penetrative foliation defined by aligned biotite and elongate quartz also visible. (c) Mesoproterozoic quartz monzonite (Yqm), with primary solid-state (?) foliation dipping to the right and with an additional penetrative foliation (defined by aligned muscovite \pm quartz) dipping to the left. (d) Variably altered dioritic intrusion (Td); likely Oligo-Miocene in age but effectively unconstrained.

3.1.1.1. Gneissic Amphibolite (Xga)

Xga (Plate 1; Figs. 4A, 5A) is a compositionally banded (mm to cm-scale) gneiss dominated by dark, mafic bands with high (i.e., ~ 15 – 65%) proportions of μm - to mm-scale, commonly euhedral hornblende \pm biotite. Substantial compositional overlap exists between lighter, more felsic bands and the nominatively separate gneissic subunit Xqfg (quartzo-

feldspathic gneiss, below), and banding may reflect pervasively deformed but originally depositional layering (Jones & Connelly, 2006). In addition to hornblende and biotite, mafic bands in Xga also contain significant, often subequal proportions of plagioclase, locally as mm-scale laths to which hornblende appears interstitial. Additional constituents include up to 35% anhedral to subhedral quartz, up to ~4% magnetite in μm -scale generally euhedral grains, and locally, up to 10% euhedral tourmaline in variably sized euhedral crystals. All outcrops suggest some, usually minor, degree of metasomatic (likely hydrothermal) alteration, and plagioclase and biotite are commonly partially altered to sericite and chlorite, respectively. The primary foliation (i.e., the one measured in the study area; Plate 1; Fig. 4A, 5A) is both compositional and penetrative; hornblende and biotite crystals (where present) are generally subtly aligned with the rock's compositional banding. Some thin sections clearly display a second penetrative foliation, also defined by aligned hornblende and biotite, cutting across the compositional and first penetrative foliations at moderate (i.e., $\sim 45^\circ$) angles. A more obscure tertiary penetrative foliation, defined by aligned hornblende and biotite and oriented approximately perpendicular to the secondary foliation, is present in one thin section. Locally, elongate hornblende and biotite also appear to define a lineation on compositional foliation surfaces. Measured compositional foliation in Xga is mostly steep to subvertical and NE-SW- to E-W-striking (Fig. 7A) but is locally (especially in the center of the map area and above the IMSZ) steep to subvertical and NNW to SSE-striking. Measured aligned-mineral lineations most commonly plunge shallowly to the SW (Fig. 7B), regardless of the orientation of local compositional foliation; this may be intersection lineation between coaxial, NE-striking foliations (Jones & Connelly, 2006).

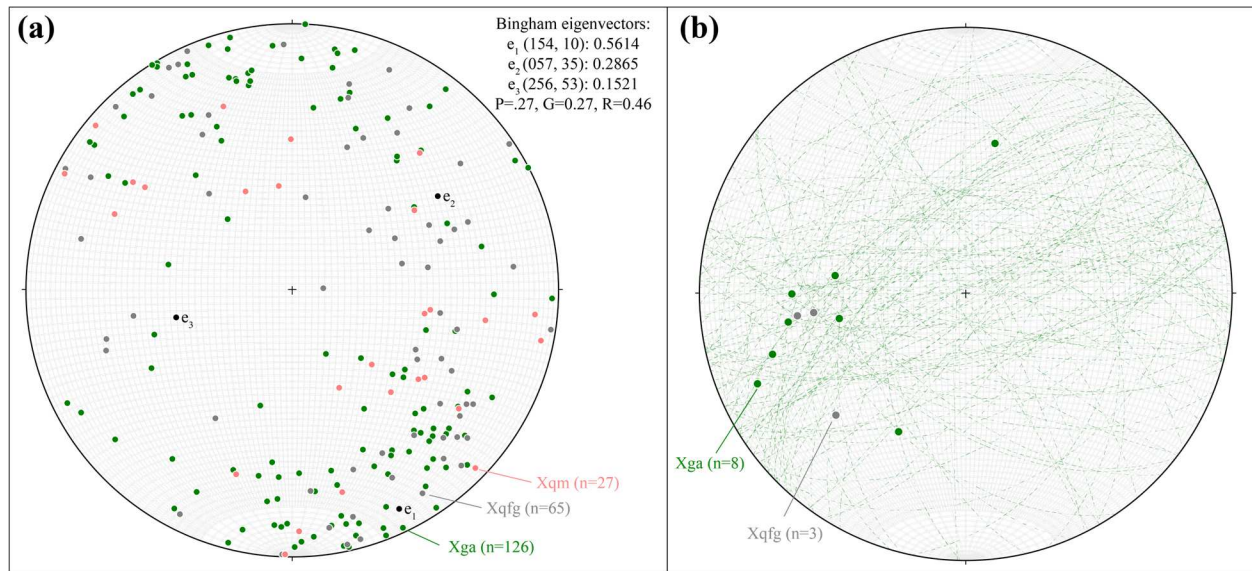


Figure 7. Equal area stereonet plots showing measured structural orientations in local Proterozoic, gneissic basement units. (a) Poles to compositional foliation planes, color-differentiated by unit and with Bingham eigenvectors, values as calculated using Stereonet (Allmendinger, 2013). (b) Aligned-mineral lineations measured within the study area; units differentiated by color.

3.1.1.2. Quartzo-feldspathic Gneiss (Xqfg)

Xqfg (Plate 1; Fig. 6B) is a gneiss that is generally tightly interleaved (i.e., cm- to m-scale) with Xga and is comprised of variable proportions of quartz and plagioclase, often with μ m- to mm-scale compositional bands rich in hornblende and biotite. Proportions of quartz and plagioclase both range from ~20–45%; plagioclase generally appears as 1–6 mm anhedral-subhedral crystals and quartz as 0.5–4 mm anhedral-subhedral grains. Microcline is usually present in sub-mm anhedral crystals, with modal percentages between 5 and 30%. Darker compositional bands (up to ~15% of total rock volume) are dominated by biotite with lesser to subequal proportions of hornblende. Plagioclase is commonly partially altered to sericite and biotite partially altered to chlorite; alteration appears to be most pervasive in the presence of hydrothermal epidote veins of unknown age. Quartz is usually elongate parallel to the compositional foliation, which is itself parallel to interleaved layers of Xga where present. At least two additional penetrative foliations oblique to the compositional foliation and defined by

aligned hornblende and biotite, with or without aligned quartz elongation, are clearly visible in one thin section. These penetrative foliations seem to be the same as those seen in Xga. In a small minority of outcrops, Xqfg resembles a plutonic texture and appears to be very lightly strained with subtle foliation visible only through sparse, foliation-aligned biotite. Foliation orientations mirror those of Xga. A shallowly SW-plunging lineation defined by aligned biotite, locally with elongate quartz, is visible on compositional foliation planes at several outcrops (Fig. 7B). As in the case of Xga, this may be an intersection lineation between compositional and secondary or tertiary penetrative foliations.

3.1.1.3. Crestone Quartz Monzonite (Xcqm)

The main body of the Crestone Quartz Monzonite (1682 ± 3 Ma zircon U-Pb date; Jones & Connelly (2006)) abuts the other gneissic units at an intrusive contact at the far northern end of the study area (Plate 1; Fig. 4B). Xcqm also appears as cm- to m-scale intrusive interlayers (i.e., similarly to Yqm, below) parallel to compositional foliations in the other basement gneisses within ~500 m of its main body. With ~35% K-feldspar, subequal plagioclase, ~25% quartz, and ~5% biotite (\pm hornblende) in ≤ 5 mm crystals, Xcqm is probably a monzogranite rather than quartz monzonite. A clear, probable solid-state foliation defined by elongate quartz and aligned biotite is clearly visible in Xcqm outcrop within the main intrusive body (i.e., Fig. 4B) and in proximal dikes. This foliation parallels the contacts with, and the prevailing foliation of, host-rock gneisses (Plate 1). Additional foliations may be present (Jones & Connelly, 2006) but were not identified in the study area.

3.1.1.4. Quartz Monzonite (Yqm)

Yqm (Plate 1; Fig. 6C) is a map unit defining gneissic rocks with a range of compositions (i.e., mostly quartz monzonite with some monzogranite and quartz monzodiorite) that

substantially overlap those of Xqfg; Yqm is distinguished by substantial proportions (i.e., > 20%) of megacrystic, ≥ 3 mm microcline. Yqm is also spatially distinct: though it appears locally as cm- to m-scale dikes interleaved along compositional foliations with Xqfg and Xga, it more commonly appears as map-scale blobs and lenses free from internal interleaving with those units (Plate 1). Like nearby, compositionally similar Mesoproterozoic rocks such as the Music Pass Pluton (Jones & Connelly, 2006), Yqm likely intruded older gneissic units after their initial deformation and metamorphism. In addition to its characteristic megacrystic microcline, rocks mapped as Yqm include approximately subequal amounts of generally anhedral, partially sericitized plagioclase, 15–35% generally anhedral quartz, and up to 15% micas, usually with biotite > muscovite. The prevailing foliation is defined by aligned elongate microcline megacrysts that often appear as augen, and locally by bands of fine-grained quartz-plagioclase-white-mica aggregate (i.e., Fig. 6C) \pm aligned biotite. Jones & Connelly (2006) characterized fabrics displaying the former feature as representing solid-state foliation in the Music Pass Pluton, and Yqm foliations indeed parallel “host” gneiss foliations in the study area (Plate 1; Fig. 7A). One thin section of Yqm suggests another, younger penetrative foliation defined by aligned, elongate quartz and biotite crystals at an oblique angle to the primary foliation. Locally (i.e., in one observed outcrop), Yqm displays cm- to m- scale isoclinal folding along an axial plane parallel to compositional foliation in nearby Xqfg.

3.1.1.5. Mesoproterozoic (?) Pegmatite Dikes

Meter-scale to cm-scale, apparently unstrained, distinctly salmon-pink pegmatite blebs and dikes appear within exposures of Yqm and Xcqm in the study area. A thin section cut from one of these “dikes” contains 55% microcline in cm-scale, anhedral to subhedral megacrysts within a “matrix” of \sim 35% plagioclase and \sim 10% quartz in mm-scale anhedral crystals. The age

of these dikes is constrained only by their lack of foliation; they necessarily postdate the Paleoproterozoic (Jones & Connelly, 2006) deformation events in which foliation developed in host-rock gneiss. Given that Jones & Connelly (2006) obtained a zircon U-Pb date of ~1434 Ma for a leucocratic but K-feldspar-rich pegmatite dike further S in the range, a Mesoproterozoic, post-Yqm age is speculated.

3.1.2. Paleozoic Units

Paleozoic sedimentary units appear in fault-bounded, usually overturned slivers and wedges in the vicinity of the Crestone thrust in the northeast of the study area and as an isolated exposure below the Deadman Creek thrust near the southern margin of the study area (Plate 1). Though some inter- and intra-formational contacts may be present (Plate 1), no complete sections are observable. As such, this study relies somewhat on descriptions and mapping of better exposures of elsewhere in the Sangre de Cristo Range for stratigraphic correlation (Johnson et al., 1987; Lindsey, Clark, et al., 1986; Lindsey et al., 1986; Lindsey et al., 1985). Mapping of the Paleozoic section in this study (Plate 1) largely corroborates prior work (Clement, 1952; Lindsey et al., 1986) in the area and complements prior mapping in adjacent areas (Lindsey et al., 1985).

3.1.2.1. Harding Formation (Oh)

The apparent basal Paleozoic unit in the study area is a light gray to buff quartzite that has been identified by previous workers as the Ordovician Harding Formation (Clement et al., 1952; Lindsey et al., 1986). This unit is exposed both along the Crestone thrust N of Copper Gulch (Plate 1) and below the Deadman Creek thrust (Plate 1; Fig. 8A). The former exposure is a ~10-m-thick sliver of pale gray, overturned, fine-grained quartz arenite that forms small cliffs above the crystalline basement; Clement (1952) interpreted the unit's basal contact here as being

a depositional unconformity, but significant variations in thickness along the observed contact suggest that the unit is instead juxtaposed against basement rocks by a splay of the Crestone thrust (i.e., Plate 1, cross-section B-B'). The upper contact with the (probable) Leadville Formation above Copper Gulch is somewhat obscure but is likely a depositional unconformity. The outcrop of Oh below the Deadman Creek thrust (Fig. 8A) is made up of about ~18 m of buff-weathering, cliff-forming fine-grained quartz arenite in capped by a ~2 m bed of darker gray, inequigranular quartzose sandstone with minor (~2%) aligned muscovite defining an incipient penetrative foliation; this bed was likely more argillaceous than the rest of the unit. The basal contact of Oh below the Deadman Creek thrust is covered by Quaternary sediments, but an upper contact with the (probable) Leadville Limestone is exposed in a single outcrop (shown in Fig. 8A). Because this contact is somewhat irregular and appears to be locally channelized (i.e., Fig. 8A), it is interpreted to be an erosional unconformity.

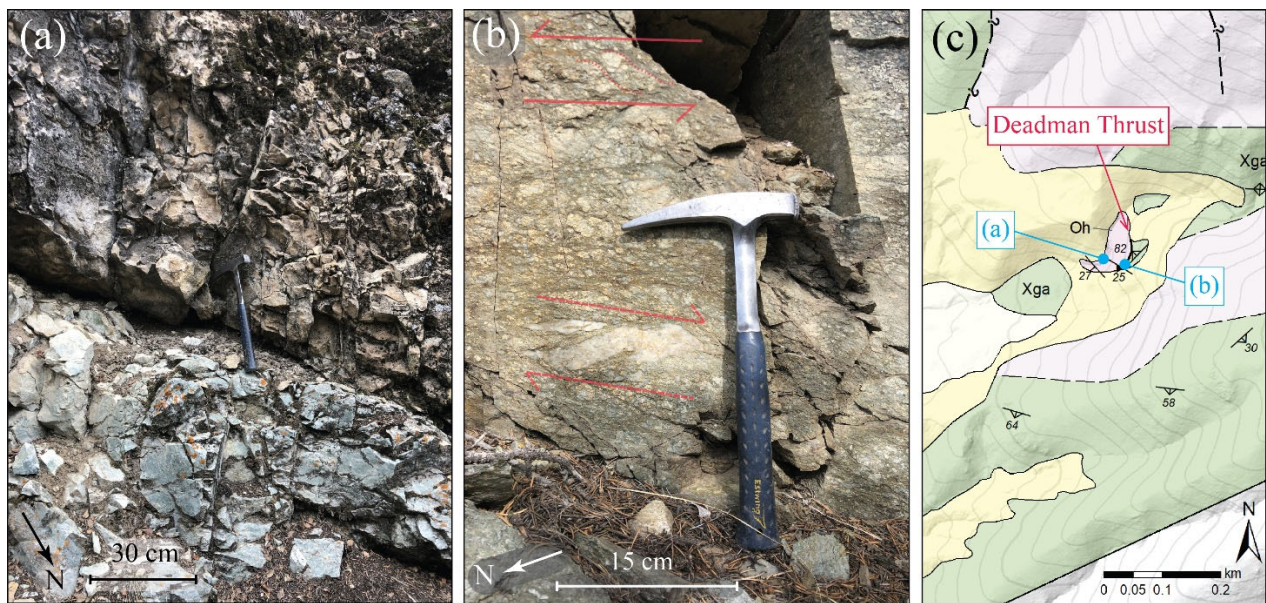


Figure 8. Photos from the apparent northernmost exposure of the Deadman Creek thrust (Lindsey, et al., 1986; Weigel, 2014) – the only exposure in the study area. (a) Contact between the Harding Formation (bottom) and a coarsely recrystallized dolomitic unit (above) tentatively identified as the Leadville Formation. Channel-like features along contact suggest an unconformity. (b) Outcrop of protomylonitic to mylonitic fabric in exposure of the interpreted Deadman Creek thrust, with Xga in hanging wall. Outcrop-scale indicators are variably compatible with top-NE kinematics (e.g., S-C-foliation; top) or more ambiguous (e.g., quartz sigmoids possibly formed through top-SW shearing of quartz veins or as

top-NE en-echelon gashes; below). (c) Reference map showing locations of photos and of Deadman Creek thrust exposure in relation to other map units.

3.1.2.2. Leadville(?) Formation (M1)

A unit of well-bedded (m-scale), overturned gray-tan dolostone crops out along the mapped trace of the Crestone thrust between Willow Creek and Copper Gulch (Plate 1). This unit is interpreted to be the Leadville Formation based on published descriptions of nearby exposures (i.e., Johnson et al., 1987; Lindsey et al., 1985), and previous mapping of the study area (i.e., Clement, 1952) identified it as such. Only a few (≤ 8) meters of section are exposed (Plate 1). At its base, the unit variably appears to overlie either the Harding Formation along an obscured but presumably unconformable contact or crystalline basement units along a similarly obscured but seemingly sharp contact. The upper contact with the Minturn Formation (Plate 1) is not exposed; localized areas of Fe-oxide mineralization parallel to the contact suggest metasomatic fluid migration along a fault. This study consequently interprets the Leadville Formation in the northern part of the study area as being situated in a thin fault bounded sliver (Plate 1).

Below the Deadman Creek thrust (i.e., Fig. 8A) the Harding Formation is overlain(?) by ~3 m of buff-weathering, inequigranular, recrystallized impure (i.e., ~2% quartz) dolostone along a likely erosional contact (Sect. 3.1.2.1; Fig. 8A). The dolostone is only exposed within the singular outcrop shown in Figure 2A; just upslope and up-dip it is covered by Quaternary sediments before (presumably) being cut by the suprajacent Deadman Creek thrust. This unit is interpreted in this study to probably also be the Leadville Formation, albeit with some caveats. Apparent cm-scale paleo-channelization (Fig. 8A) at the contact is the sole, somewhat equivocal indicator for depositional facing direction in the Paleozoic section below the Deadman Creek thrust. If the section is overturned, this unit could in fact be the Early Ordovician Manitou

Formation, which per Lindsey et al. (1985) underlies the Harding Formation farther N in the range. The Late Ordovician Fremont Formation (e.g., Lindsey et al., 1985) is another plausible candidate even if the section is not overturned given that the unconformity could encompass less missing section than is probable between Willow Creek and Copper Gulch.

3.1.2.3. Minturn Formation (Pm, Pmu)

About 325 m of gray to maroon shale, siltstone, sandstone, pebble conglomerate, and slate within an internally faulted wedge that is itself bound on both sides by splays associated with the Crestone thrust are interpreted as representing the lower Minturn Formation in the study area (Plate 1). Between Willow Creek and Copper Gulch (Plate 1), the Minturn Formation is dominated by distinctly red-weathering (with significant proportions of μm -scale Fe-oxide grains in thin section), medium- to fine-grained, quartz-rich siltstone and sandstone with minor interspersed, variably graded pebble conglomerate. This lithology likely corresponds to the (Minturn) “quartzose red-beds” of Lindsey et al. (1985). Gray and grayish-red sandstones and siltstones are more frequent moving along strike through the unit towards the northern boundary of the study area (Plate 1). Grading evident in some pebble conglomerate beds and some (scant) cross-bedding in sandstone both indicate that the Minturn Formation here is overturned. A moderately SW-dipping slaty cleavage defined by aligned white mica is locally present in Minturn outcrops (Plate 1; Fig. 9A). This cleavage is increasingly well-developed closer to probable splays of the Crestone thrust, and several outcrops within ~ 100 m of interpreted thrust splays are phyllitic, with up to 70% cleavage-aligned white mica and minor, probable talc apparently generated through alteration of sparsely preserved plagioclase and matrix clays. Possible minor chloritoid ($\leq 1\%$, as ≤ 100 μm randomly oriented crystals) was identified in one sampled phyllite outcrop. Chloritoid is locally prominent in phyllitic Minturn Formation along

North Crestone Creek (<2 km N of the Plate 1 map area; Lindsey et al., 1986). Mapped internal and unit-bounding thrust/reverse faults in the Minturn Formation (Plate 1) were interpreted based on observations of consistent lithological differences (e.g., substantial variations in the proportions of red-beds, internally) across bands of well-developed slaty or phyllitic cleavage subparallel to the Crestone thrust. Between Willow Creek and Copper Gulch, the main body of the Minturn Formation is likely juxtaposed against the lower Member of the Sangre de Cristo Formation along one such fault (Plate 1).

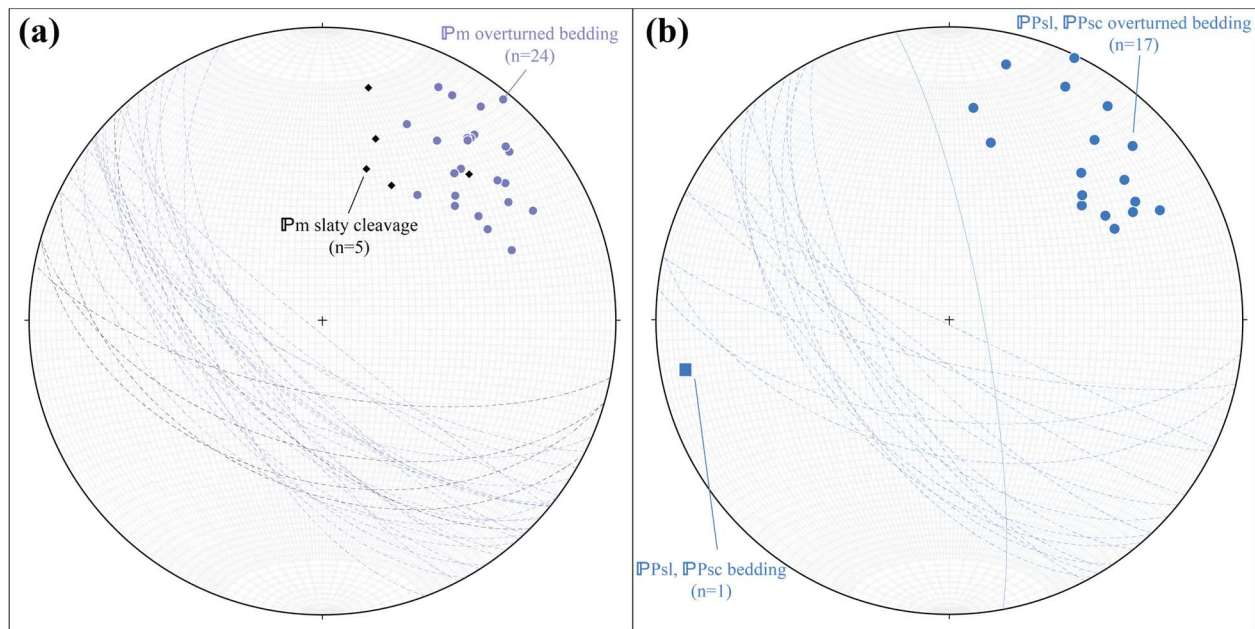


Figure 9. Poles to per-station eigenvector best-fits of bedding and bedding-subparallel cleavage measured in Paleozoic units within the study area. (a) Overturned bedding and slaty cleavage in the Minturn Formation, including its Upper Member. (b) Bedding and overturned bedding in the Sangre de Cristo Formation (lower member and Crestone Conglomerate member).

Closer to the northeastern corner of the study area, another interpreted thrust splay (i.e., a ~30 m-wide band of red phyllite with SW-dipping cleavage) separates finer-grained Minturn siltstone and sandstone (IPm in Plate 1) to the southwest from a ~180 m-thick, overturned package of coarser rocks including interbedded gray to red-purple siltstone and quartzose sandstone, polymict pebble conglomerate, with cm-scale beds of gray limestone in a few subcrop

exposures (**P_{mu}**; Plate 1). This lithology matches a description of the upper 300 m of an “Upper Minturn” member from Lindsey et al. (1985), though they do note a “phylloid algal limestone” marker bed that was not identified in the field area. Near the northeast corner of the map area, sparse outcrops of **P_{mu}** appears to grade into the less erosive pebble conglomerates and sandstones of the Lower Sangre de Cristo Formation (Plate 1) along an interpreted contact approximately along strike with the one mapped by Lindsey et al. (1985) ~2 km to the north-northeast. Apparent thinning of the **P_{mu}** above Willow Creek suggests that the contact may be cut by a thrust fault splay further to the S (Plate 1). Overturned bedding in the Minturn Formation typically dips moderately to steeply southwest (Plate 1; Fig. 9A).

3.1.2.4. Sangre de Cristo Formation (**P_{PSl}**, **P_{PSc}**)

Approximately 100 to 200 m of 5-30 m-thick, overturned packages of red-gray to maroon rock that grade stratigraphically upwards from quartz-rich fine-grained sandstone to pebble-cobble, generally matrix-supported conglomerate form cliffs between Copper Gulch and the northern end of the study area (Plate 1). These rocks have been tentatively identified as the Lower Sangre de Cristo Formation, as mapped by Lindsey et al. (1985) further to the north. This interpreted **P_{PSl}** unit has a gradational contact with the underlying Minturn Formation N of Willow Creek (Plate 1) and is juxtaposed against **P_m** along an apparent high-angle reverse fault that runs sub-parallel to bedding between Willow Creek and Copper Gulch (Plate 1). Beds within the **P_{PSl}** unit appear to strike into each other at several locations N of Willow Creek, which suggests the presence internal thrust faulting (Plate 1). A sharp transition from graded sandstone-conglomerate packages along one such interpreted internal fault (Plate 1), combined with probable missing section (Lindsey et al. (1985) record a thickness of 600–900 m for the unfaulted **P_{PSl}**) suggests a faulted **P_{PSl}**-**P_{PSc}** contact N of Willow Creek. Missing section is

likewise probable farther S (between Willow Creek and Copper Gulch; Plate 1), but there the **PPS** unit seems to grade into the overlying cobble-boulder Crestone Conglomerate along an irregular but likely depositional contact, with local missing section probably attributable to splays of the Crestone thrust.

Upwards of 700 m of interbedded (m to 10s-of-m-scale) reddish-gray to maroon sandstone and pebble to large boulder, generally matrix-supported conglomerate make up the Crestone Conglomerate member of the Sangre de Cristo Formation in the study area (Plate 1; (Clement, 1952; Lindsey et al., 1986; Lindsey et al., 1986). Cobble to boulder conglomerate layers are usually polymict, with amphibolite (i.e., Xga), quartz-monzonite, and syenite as major constituents; quartz-monzonite clasts are dominant except in the northeastern corner of the study area, where syenite clasts are dominant. Beds within the Crestone Conglomerate are mostly overturned (as indicated by internal grading in conglomeritic interval) and dip moderately to steeply to the SSW (Plate 1; Fig. 9B). Non-overturned beds at the far northeast corner of the map area dip steeply to the NNE (Plate 1; Fig. 9B).

3.1.3. Cenozoic Intrusives

The pre-Cenozoic rocks and structures (e.g., the Crestone thrust) within the study area are cut by mafic to felsic dikes and by mafic to intermediate intrusions. These rocks have been split into the four units described below for mapping and analytical purposes.

3.1.3.1. Andesite Dikes (Tad)

Dark gray to greenish-brown-weathering, 1–10 m-thick aphanitic to porphyritic dikes can be found throughout the crystalline basement of the study area (Plate 1) and have been noted by previous workers (e.g., as “minette” and “hornblende-augite-vogesite” lamprophyres by Clement (1952)). The original petrology of these dikes is somewhat obscured by pervasive chloritization

of mafic minerals, but they seem to be intermediate to mafic in composition and may encompass multiple rock types. Three thin sections cut from dikes along the range front suggest that these rocks are characterized by significant proportions of mafic minerals (up to 35%, hornblende with subequal amounts of biotite in μm -scale, variably euhedral crystals that are partially to fully altered to chlorite) and plagioclase (~40-50%, in μm -scale laths that often appear to be interstitial to biotite; Fig. 10C). One observed dike is porphyritic, with ~5% elongate 0.3 to 3 mm phenocrysts completely altered to chlorite, likely after biotite (Fig. 10C). Other constituent minerals observed include $\leq 5\%$ anhedral quartz blebs, $\leq 5\%$ opaque grains (likely magnetite), and ~1% apatite in elongate grains clearly visible in plane-polarized light (Fig. 10C). An Oligo-Miocene age for these rocks is likely given contemporary intermediate to mafic volcanism in the region (Thompson et al., 2022) and within the study area itself (i.e., P₁g). As speculated by Clement (1952), some or all of the dikes may be genetically related to local intrusive stocks (P₁g, Td).

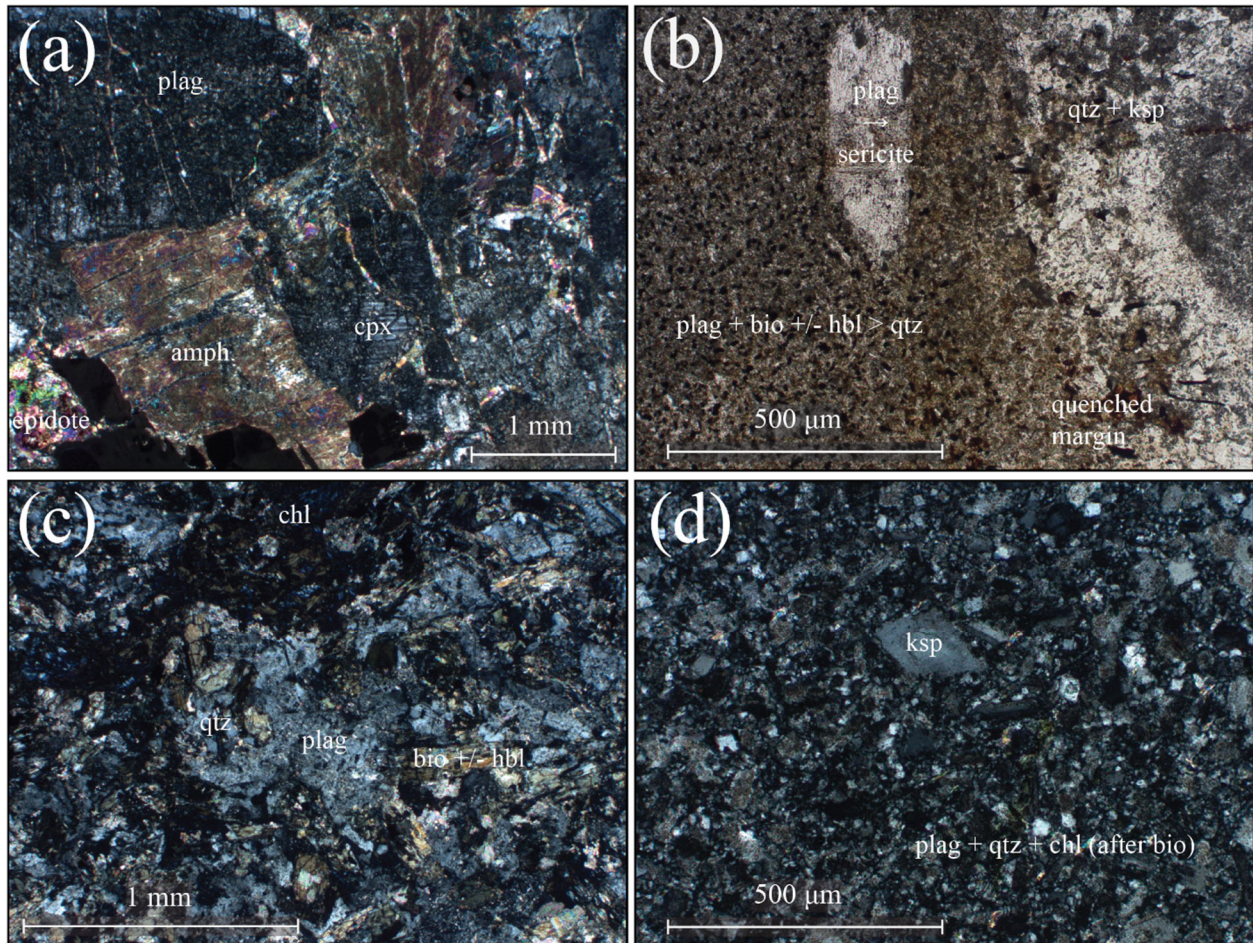


Figure 10. Representative photomicrographs of Cenozoic intrusive units found within the study area. (a) Gabbroic intrusion (Peg), with megacrystic partially sericitized plagioclase, and interstitial amphibole mantling poorly preserved clinopyroxene. (b) Quenched margin between a Peg stock and surrounding quartzo-feldspathic gneiss. (c) Andesite dike (Tad); porphyritic with mm-scale chlorite porphyrocrysts in matrix of intergranular plagioclase, quartz, and chloritically-altered hornblende. (d) Leucogranite dike (Tl); locally finely porphyritic with K-feldspar in matrix of quartz with plagioclase and chlorite, generally altered to sericite and chlorite, respectively.

3.1.3.2. Gabbroic Intrusive (Peg)

A greenish-dark-gray, phaneritic gabbroic unit intrudes crystalline units in the study area in irregular dikes and stocks of variable (i.e., 10s to 1000s of m²) lateral extent (Plate 1).

Quenched margins are present at contacts between the intrusive unit and host rock (Fig. 10B).

The rock's original composition is often obscured by metasomatic, presumably hydrothermal alteration; mafic minerals are commonly partially or fully altered to chlorite, and feldspars are generally partially altered to sericite. Examination of petrographic thin sections cut from less

altered samples suggests an ophitic texture with clinopyroxene (~5–12%, in mm-scale euhedral to anhedral phenocrysts) and amphibole (~10–15%, often as rims around clinopyroxene phenocrysts) interstitial to $\geq 50\%$ feldspar in > 3 mm-long laths. Laths are likely exclusively plagioclase, though internal zoning is broadly obscured by alteration. Additional constituents include opaque, subhedral equant to prismatic grains (presumably magnetite; $\leq 4\%$), as well as quartz (~3%, in anhedral, sub-mm grains) and apatite (~1%). This mineralogy approximates that of the “quartz-uralite-diabase” described by Clement (1952). Zircon U-Pb dates from a stock along the N side of Cottonwood Creek (Plate 1) indicate a likely crystallization age of 25.57 ± 0.74 Ma.

3.1.3.3. Paleogene(?) Diorite Intrusion (Td)

An exposure of megacrystic, unfoliated, gray-brown-weathering diorite appears on the ridge between Copper Gulch and Spanish Creek (Plate 1). In thin section this rock contains ~75% 1–3 cm long, ~5 mm thick plagioclase laths, with ~9% interstitial anhedral quartz and ~14% generally chloritized mafic minerals (biotite where preserved, though original hornblende is likely), with opaque minerals (likely Fe-oxides) and apatite as minor constituents (Fig. 6D). Plagioclase crystals commonly have 100–300 μm -thick clear rims, but their interiors are ubiquitously sericitized. In outcrop, Td appears to be morphologically similar to Miocene mafic intrusives that crop out elsewhere in the study area (i.e., **Peg**, above), but is speculatively considered to be a different unit based on mineralogical differences. Mineralogy observed in thin section suggests that Td is less mafic (lacking clinopyroxene) than **Peg**. The age of this unit is poorly constrained. Clement (1952) infers that Td is cut by the Crestone thrust and proposes an early Eocene age, but satellite and aerial orthoimagery and field observations from adjacent ridges suggest that the Td instead intruded along and above the Crestone thrust; the contact in

question was regrettably not examined up-close in this study. Given the lack of evidence for higher-grade (i.e., Proterozoic) metamorphism and the glut of Oligo-Miocene intermediate-mafic intrusive rocks both within the study area (i.e., **P_{eg}**) and in the broader region (e.g., Johnson et al., 1987; Penn & Lindsey, 2009; Thompson et al., 2022), a Tertiary (probable Oligo-Miocene) age is proposed for Td.

3.1.3.4. Rhyolitic Dikes (Trd)

Numerous white to light gray, variably aphanitic to porphyritic, ≤ 10 m-thick felsic dikes crosscut the Proterozoic crystalline rocks and intrude along the Crestone thrust within the study area (Plate 1). A single petrographic thin section was cut from a felsic dike exposure on the ridge between Deadman and Cottonwood Creeks (Plate 1). This dike (Fig. 10D) is a lightly altered, sparsely porphyritic rhyolite containing $\sim 2\%$ 1–3 mm sanidine(?) phenocrysts in a holocrystalline matrix of randomly oriented, 1–100 μm -long crystals of plagioclase ($\sim 40\%$), quartz ($\sim 50\%$), and chlorite (presumably altered after biotite). U-Pb zircon dates for rhyolitic “felsite” dikes in the Deadman Creek area from Holm-Denoma et al. (2019) suggests Late Oligocene (~ 27 Ma) crystallization. The same is likely broadly true of the leucogranite dikes in the study area, but in one exposure in the northern quadrant of study area (along the Crestone thrust; Plate 1) a Tl dike appears to cut a **P_{eg}** intrusion, and Tl is thus likely at least slightly younger.

3.1.4. Surficial Deposits

Bedrock units in the study area are covered by a number of alluvial, mass-wasting-related, and glaciofluvial deposits. Though these units were mapped, they are not the focus of this study and so have not been analyzed in great detail. Descriptions of each are below.

3.1.4.1. Glacial and Glaciofluvial Deposits

Unsorted deposits of silty till and sub-rounded to angular, surficially-weathered boulders (largely of the Sangre de Cristo Formation) appear in apparent moraines with gentle, eroded crests along the range front and up some valleys in the study area (Qbt; Plate 1). These sediments seem to be the oldest primary glacial deposits in the study area and most exposures have been linked to the Bull Lake glaciation (penultimate glacial maximum) by previous workers (Lindsey, Johnson, et al., 1986; McCalpin, 1981; Ruleman & Brandt, 2021). Presumed Qbt moraines seem to be better preserved at higher elevations along drainages (e.g., Spanish and Cottonwood Creeks) but have been completely eroded to bedrock or to the elevation of the San Luis Valley floor, where they are cut by larger streams (Plate 1). Locally (e.g., in some areas along moraine margins up Copper Gulch and Spanish Creek), abandoned or ephemeral streams have eroded finer-grained till to create elongate, jumbled piles of weathered boulders.

Variably dissected fans comprised of gray-tan, poorly to well-stratified, unsorted sand, silt, and polymict pebble-boulder-sized clasts form topographic highs off the range front (Qbf; Plate 1). These deposits have been identified by previous workers as dating to the Bull Lake glaciation (Lindsey et al., 1986; McCalpin, 1981; Ruleman & Brandt, 2021), and are indeed observed to be variably onlapped or cut by presumably younger glaciofluvial and alluvial units (Plate 1). Scarps for normal faults in the Sangre de Cristo fault system appear clearly on Lidar hillshade where they cut Qbt fans (Plate 1).

Deposits of poorly-sorted sediment composed of polymict boulders within a distinctly brown-tan colored sand-silt matrix are found overlying presumed Qbf deposits along the range front, just S of the confluence of Willow Creek and Copper Gulch (Qppt; Plate 1). These sediments have been identified by previous workers as either Bull Lake Fan deposits (by

McCalpin (1981), with the overlapped fan deposits assigned to an older glaciation) or as an intervening alluvial unit deposited between the Bull Lake and Pinedale glaciations by Lindsey et al. (1986). The latter classification is applied in this study.

Relatively sharp-crested, moraines of unsorted pebble- to boulder-sized polymict clasts (dominantly Sangre de Cristo Formation) within a silt-clay matrix are found along and above Willow Creek in the study area (Qpt; Plate 1). Exposed boulders are commonly relatively fresh, though some appear to be thoroughly weathered and thus may be inherited from earlier glacial deposits. Qpt moraines are generally lightly dissected and appear to control the courses of streams (e.g., Willow Creek) that intersect them. These moraines have been correlated with the Pinedale glaciation (last glacial maximum) by previous mappers (Lindsey et al., 1986; McCalpin, 1981; Ruleman & Brandt, 2021) and dated as such by Leonard et al. (2017).

An expanse of silty-clayey sediment appears in an uncharacteristically flat-lying, ephemeral marshy area bounded by Qpt lateral and terminal moraine deposits along Willow Creek (Qpl; Plate 1). This area is presumed to have been covered by a moraine-dammed lake after initial retreat of Pinedale-aged glaciers (Leonard et al., 2017) and to have drained more recently after sufficient downcutting by Willow Creek.

Deposits of unsorted, generally poorly-stratified, light-gray to tan sand, silt, and polymict pebbles-boulder clasts appear in fans at mouths of valleys and canyons along the range front (Qpf; Plate 1). These relatively topographically low and undissected fans probably formed primarily during and shortly after the Pinedale glaciation, as per previous mappers (Lindsey, Johnson, et al., 1986; McCalpin, 1981), but were identified primarily via satellite orthoimagery and Lidar DEM and may encompass other geomorphologic units (Ruleman & Brandt, 2021).

Some normal fault scarps cutting Qpf deposits (e.g., just N of Willow Creek in the northwestern quadrant of the map area; Plate 1) are clearly visible on Lidar hillshade of the study area.

3.1.4.2. Mass Wasting Deposits (Qls, Qrf, Qt)

Landslide deposits of rock, mud, and debris are found above Copper Gulch and Cottonwood Creek within the field area (Qls; Plate 1); scarps for both are readily identifiable on a Lidar hillshade base map. Smaller mass wasting deposits comprised primarily of boulders (Qrf; Plate 1) also appear below chutes above Cottonwood Creek. Talus deposits (i.e., accumulations of locally derived boulders; Qt; Plate 1) mantle steeper slopes within the study area, especially above the timberline (Plate 1; Fig. 2B).

3.1.4.3. Eolian sand (Qes) and Alluvium (Qal)

Sheets and dunes of well-sorted windblown sand appear along the range front, especially near the southern border of the map area (Qes; Plate 1; Fig. 2B). Some thin (i.e., ≤ 50 m wide) fingers of eolian sand extend onto the range front itself, locally reaching elevations of more than 300 m above the San Luis Valley floor (Plate 1). Unconsolidated, polymict alluvium is found throughout the study area along washes, streams, and valley bottoms (Qal; Plate 1).

3.2. Geologic Structures

3.2.1. Proterozoic Structures

Centimeter-scale isoclinal and pygmatic folds (e.g., Fig. 4A) are common in outcrops of gneiss (Xga, Xqfg) within the study area, but they their axial planes are generally parallel to the dominant compositional foliation at a given location and were not measured as discrete structures. Six m-scale antiforms (n=4) and synforms (n=2) were identified within Proterozoic units (Xga, Xqfg, and Yqm). These folds range from isoclinal (interlimb angle $\sim 8^\circ$) to

moderately tight (interlimb angle $\sim 50^\circ$), and are variably either overturned and NW-vergent, overturned and SW-vergent, or (in the case of one isoclinal synform within an exposure of Yqm) overturned and N-trending; most folds are either NE- or SW-plunging (Fig. 11A).

In several parts of the study area, relatively thick (i.e., 10s to 100s of m), \sim NE-trending bands of individual Proterozoic basement units seem to repeat in patterns that are consistent with NE-trending, upright antiforms and synforms. Intra-basement fold traces were interpreted where substantiated by measurements of compositional foliation (Plate 1). These folds range in tightness (from open to close) and interpretable axial trace extent (from ~ 400 m to ~ 3000 m), but seem to be distinct from the isoclinal, m-scale folds commonly observed in gneissic basement outcrops (e.g., Fig. 4A). Interpretation of these map-scale folds should be appropriately qualified: given the ubiquitous cm- to m-scale variations in composition and structural orientation within the gneissic basement, the actual Proterozoic structure of the area and of these folds is probably much more complex than that which was mapped.

Centimeter- to mm-scale, curvilinear epidote veins cut the compositional foliation of units within the gneissic basement throughout the study area, and a small ($n=27$) dataset of epidote vein orientations was collected (Fig. 11B). Though sometimes observed in outcrop to be oriented sub-parallel to host rock compositional foliation, most of these are either moderately to steeply NE-dipping or moderately to shallowly SW- to W-dipping. Strikes in the former population are broadly similar to those of the NW-striking populations of joints best represented in Proterozoic units (Fig. 11B), and roughly opposite those of shear zones in the study area (Fig. 14A). Epidote veins do not fit a girdle distribution: P, G, and R values (Vollmer, 1990) for the dataset are 0.39, 0.08, and 0.54, respectively.

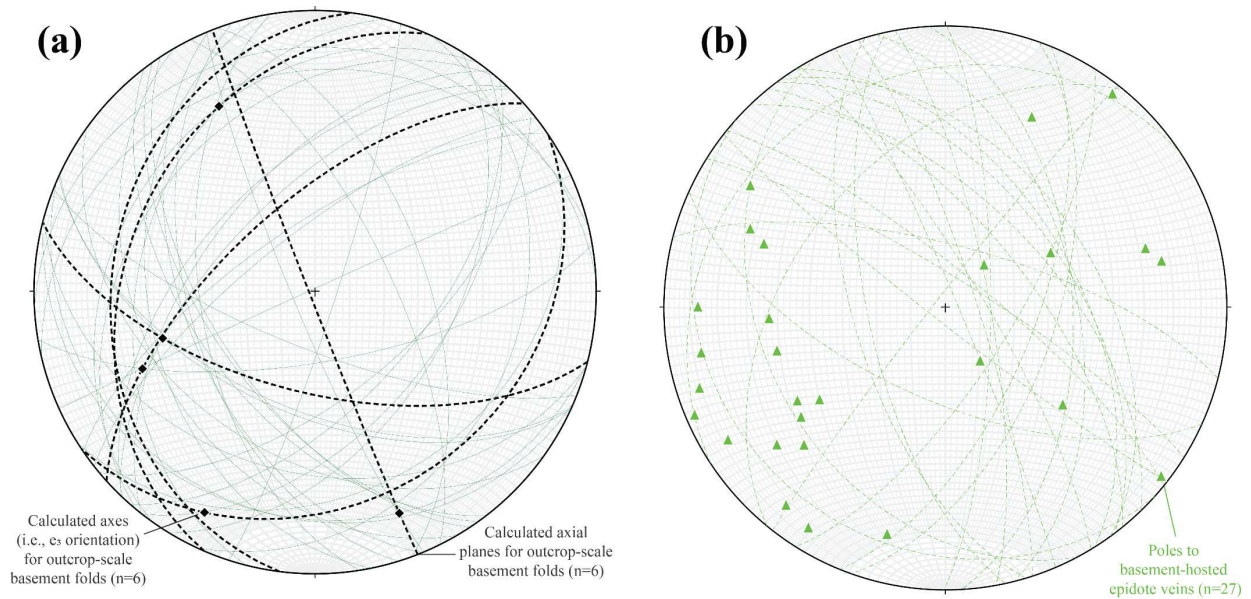


Figure 11. Equal area plots of outcrop-scale (a, b) and map-scale (c) structures identified and measured within the study area. (a) Axes and axial plunges for outcrop-scale folds in gneissic units; calculated using Stereonet (Allmendinger et al., 2013). (b) Poles to epidote veins hosted by Proterozoic basement units.

3.2.2. Thrust/Reverse Faults & Associated Structures

The Crestone thrust and associated splays appear in a ≤ 1 km-wide, NNW- to NE-trending zone of faulted sedimentary rock that appears to narrow approaching the east-northeast boundary of the study area (Plate 1). Together these faults record overthrusting of crystalline basement over a thick ($\leq \sim 3000$ m based on thicknesses given by Lindsey et al. (1985)) package of Paleozoic strata. Three-point problem solutions suggest that the Crestone thrust itself dips shallowly ($\sim 28\text{--}30^\circ$; Plate 1, cross section A-A') to the southwest but interpreted splays farther to the northeast are probably steeper given that they do not appear to cut the peaks that rise sharply (at net slopes of $45\text{--}50^\circ$) just to the E of the study area (Plate 1, cross section A-A'). Bedding is broadly overturned to the NE in Paleozoic units below the Crestone thrust system and its constituent splays. Mapping suggests that this structural configuration was produced through a combination of localized drag folding below the Crestone thrust system and fault block rotation

within it (Plate 1, cross section A-A'), as proposed by previous workers (e.g., Lindsey et al., 1986). Bands of SW-dipping slaty to phyllitic cleavage appear in footwall exposures of the Minturn Formation close to interpreted faults in the Crestone thrust system, though these zones seem to have gradual borders and so differ from the sharply-defined brittle-plastic shear zones apparent elsewhere in the study area. Undeformed, presumably Oligo-Miocene-aged intrusions that likely cut the Crestone thrust (Plate 1) may provide a constraint for its latest movement.

An interpreted exposure of the Deadman Creek thrust and underlying Paleozoic section (Figs. 8A, 8B) appears near the southern edge of the study area in an apparent erosional window that is mostly obscured by Quaternary sediment (Plate 1). Unlike the Crestone thrust system, this exposure of the Deadman Creek thrust is marked by a discrete, ≤ 10 m-thick zone of protomylonite to mylonite that appears to be composed of a variably comminuted mixture of hanging wall gneiss and footwall Harding Formation quartzite (Plate 1; Fig. 8B). Outcrop-scale S-C fabrics that are mostly consistent with top-NE (thrust-sense) kinematics are apparent in some exposures of the shear zone, with the prevailing foliation dipping $\sim 25^\circ$ WSW (Fig. 8B). Other local kinematic indicators suggest top-SW (normal-sense) kinematics, including C bands and, more equivocally, quartz sigmoids which may be interpretable as either (top-SW-) sheared quartz veins or as top-NE-consistent en-echelon gashes (Fig. 8B).

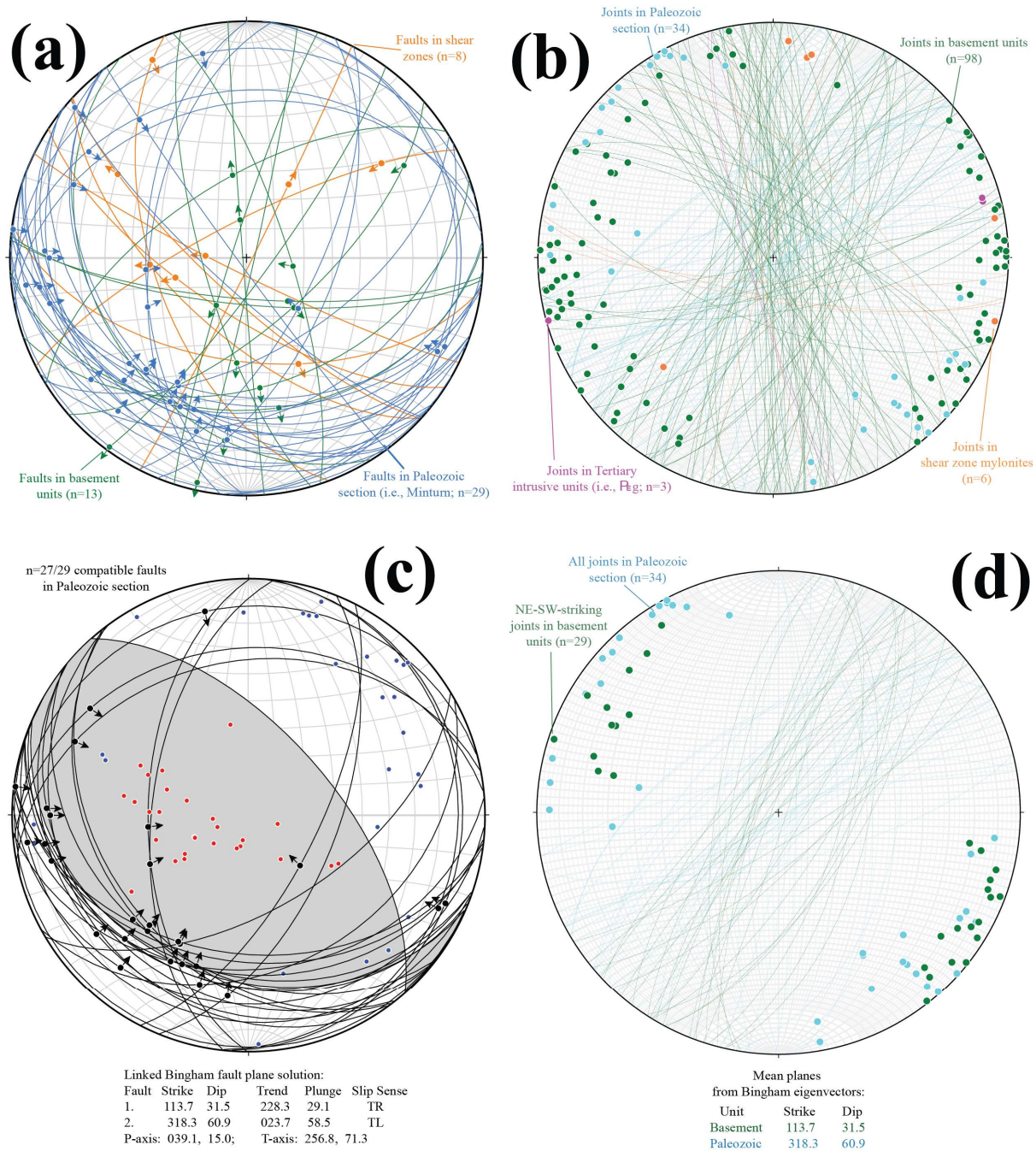


Figure 12. Structural orientations and analyses related to thrust and reverse faults in the study area. (a) Faultkin (Allmendinger et al., 2013) plot showing all outcrop-scale fault measurements for which slickenlines and slip sense indicators were recorded. (b) All joint measurements from the map area. (c) Subset of kinematically compatible faults (27/29) hosted within the Minturn Formation, with P-T axes and linked Bingham fault plane solutions plotted. (d) Joints hosted by the Paleozoic section in the map area along with a NE-SW-striking subset of joints from the Proterozoic basement.

Outcrop-scale fault plane exposures with slickenlines and indicators for shear sense (e.g., slickenfiber steps, R or R' shears, or T-shears) can be found throughout the study area (i.e., Fig.

12A). The best-preserved fault planes in the study area are, however, found in the Minturn Formation, generally in the immediate vicinity of the Crestone thrust and its mapped splays. These fault planes commonly display quartz stepped slickenfibers. A Bingham fault plane solution generated from a kinematically compatible subset of 27 fault planes in the Minturn Formation (Fig. 12C) is compatible with slightly oblique, NE-SW-directed shortening along a either a moderately NE-dipping plane or a shallowly ($\sim 30^\circ$) SW-dipping plane. The latter is notably similarly oriented to the Crestone thrust itself (Plate 1).

NE-, N-, and NNW-striking, steeply-dipping joints are common in the study area (Fig. 12B). Intra-outcrop relationships between these sets are sparse, though the NE-striking set was observed to be younger than (i.e., truncate against) the NW-striking set (Fig. 12B) in one outcrop of Xga. All joints measured in the Paleozoic section (i.e., the Minturn Formation) and a significant ($n=29$; Fig. 12D) subset of joints in the Proterozoic basement belong to the NE-striking set. The orientations of these joints would be compatible with formation in a NE-directed shortening regime, and they indeed strike roughly parallel to the linked Bingham P-axis (shortening axis) of faults in the Minturn Formation in the vicinity of the Crestone thrust (Figs. 12C, 12D).

3.2.3. *Shear Zones*

3.2.3.1. Independence Mine Shear Zone

New mapping of the IMSZ (Plate 1) largely corroborates prior work (Clement, 1952; Johnson et al., 1987; Lindsey, 1986): the shear zone appears to be truncated by the Sangre de Cristo fault at its southern end and is (commonly sporadically) exposed over a length of ~ 4.8 km before being concealed by Quaternary sediment near the confluence of Willow Creek and Copper Gulch (Plate 1). Neither evidence for a buried, \sim E-W-striking thrust fault along Copper

Gulch (i.e., as mapped by Lindsey et al., 1985) nor any exposures of the IMSZ where it might exit Quaternary cover N of Copper Gulch were identified; it is possible that the IMSZ is truncated at its northern end beneath Quaternary deposits by an unidentified normal fault associated with the Sangre de Cristo fault system. Three-point problems along the mapped trace of the IMSZ suggest that it is curvilinear: dips range from 25 to 62° W to WSW, with shallower dips at the northern and southern ends of the mapped exposure and increasingly W-dipping orientations moving N (e.g., calculated orientations of 181, 32 W; 169, 56 W; and 154, 26 SW along the northernmost, central, and southernmost segments; Plate 1). The true thickness of the IMSZ (where exposed) ranges from 15 m to ~100 m (Plate 1). Though the IMSZ is bound on either side by different gneissic units along parts its mapped exposure, the complexity inherent to the crystalline basement of the study area precludes estimation of displacement from intra-basement geologic offset markers (Plate 1; Fig. 4A). Regardless, the IMSZ is partially or fully hosted within gneissic amphibolite throughout the study area (Plate 1). The IMSZ occasionally parallels gneissic foliation in Xga but much more commonly cuts across basement fabrics (Fig. 14A).

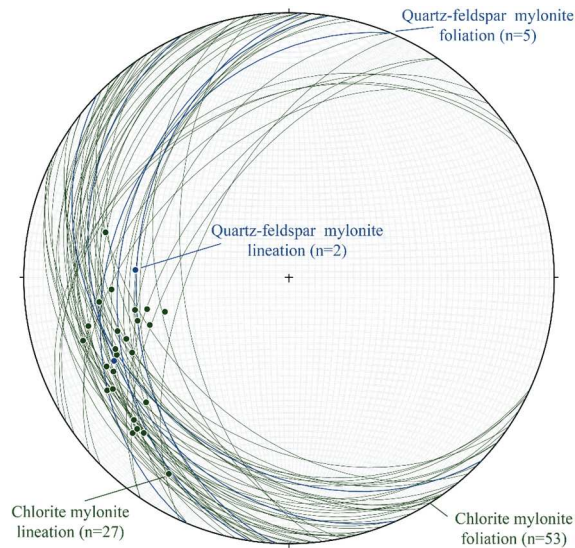


Figure 13. Mylonitic foliation and lineation measured within the IMSZ, with orientations from chlorite-rich and quartz-feldspar-rich mylonites differentiated by color.

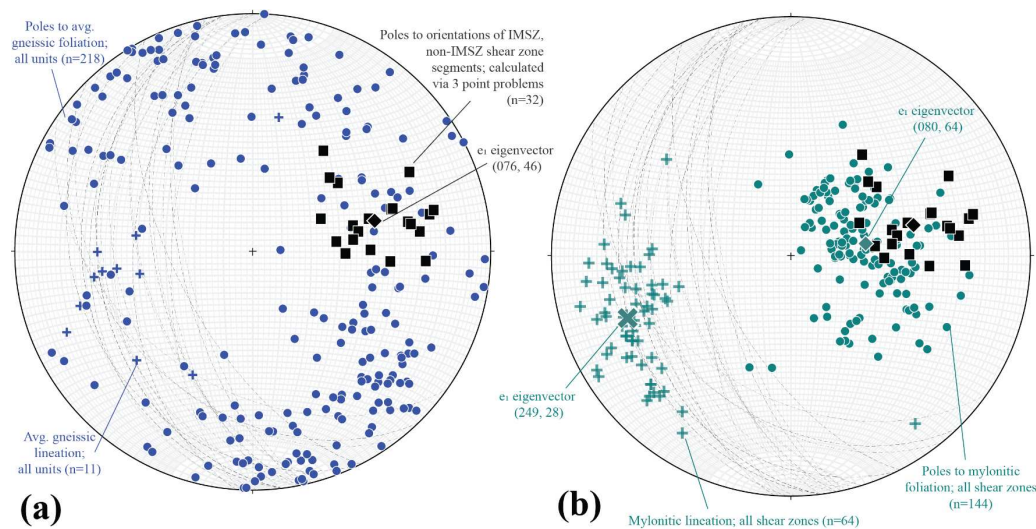


Figure 14. Poles to planes of all mylonitic shear zone segments calculated from mapped traces using three-point-problem QGIS tool plotted alongside compilations of other significant structural elements in the study area. (a) Gneissic foliation and lineation. (b) Mylonitic foliation and lineation.

Rocks within the mapped IMSZ are composed of chlorite-rich mylonites and ultra-mylonites, with minor, localized areas of quartz-feldspar-rich protomylonite to mylonite near contacts between the IMSZ and quartzo-feldspathic host rock (Plate 1; Fig. 13). Mylonitic foliation defined by aligned phyllosilicates \pm quartz bands is ubiquitous in IMSZ mylonites, and a lineation generally defined by elongate quartz grains and streaks of mica is common (Fig. 13).

Foliation dips $\sim 15\text{--}40^\circ$ WSW to WNW, and lineation plunges approximately down-dip to the WSW (Fig. 13). No variations in orientations of mylonitic foliation and lineation between chlorite-rich and quartz-feldspar-rich IMSZ mylonites are apparent (Fig. 13), but mylonitic foliation dips in both are consistently $\geq 10^\circ$ shallower than that of the calculated (i.e., by three-point-problem) local orientation of the IMSZ margins (Plate 1; Fig. 14B). Macro-scale S-C fabrics with locally well-developed C' shear bands are visible in most exposures of the IMSZ (Figs. 15A, 15B). Generally, these fabrics are consistent with top-SW (normal-sense) kinematics (e.g., Figs. 15A, 12), but they locally suggest top-NE (thrust/reverse-sense) shear, most notably at the Independent Mine itself (Figs. 15B, 12).

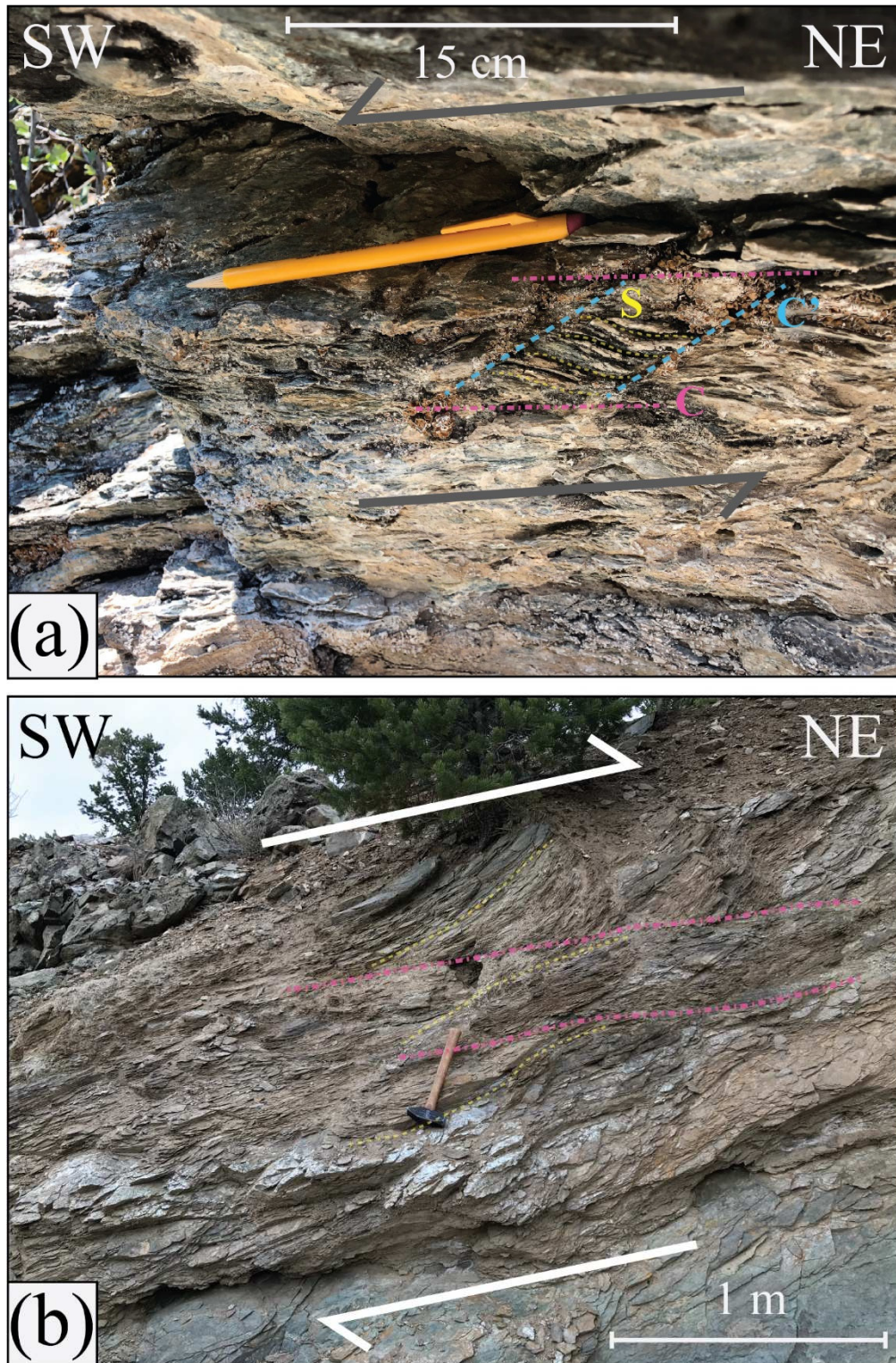


Figure 15. Photographs of cm- to mm-scale S-C, S-C-C' shear fabrics within the IMSZ in the study area. (a) Well-developed S-C-C' fabric, compatible with top-SW (normal-sense) kinematics, in IMSZ chlorite ultramylonite at Spanish Creek. Annotated and labelled to indicate interpreted sense of shear and highlight S, C, and C' bands. (b) Outcrop-scale S-C fabric at the Independent Mine. Kinematically compatible top-NE (thrust-sense) kinematics; photograph annotated to indicate interpreted sense of shear.

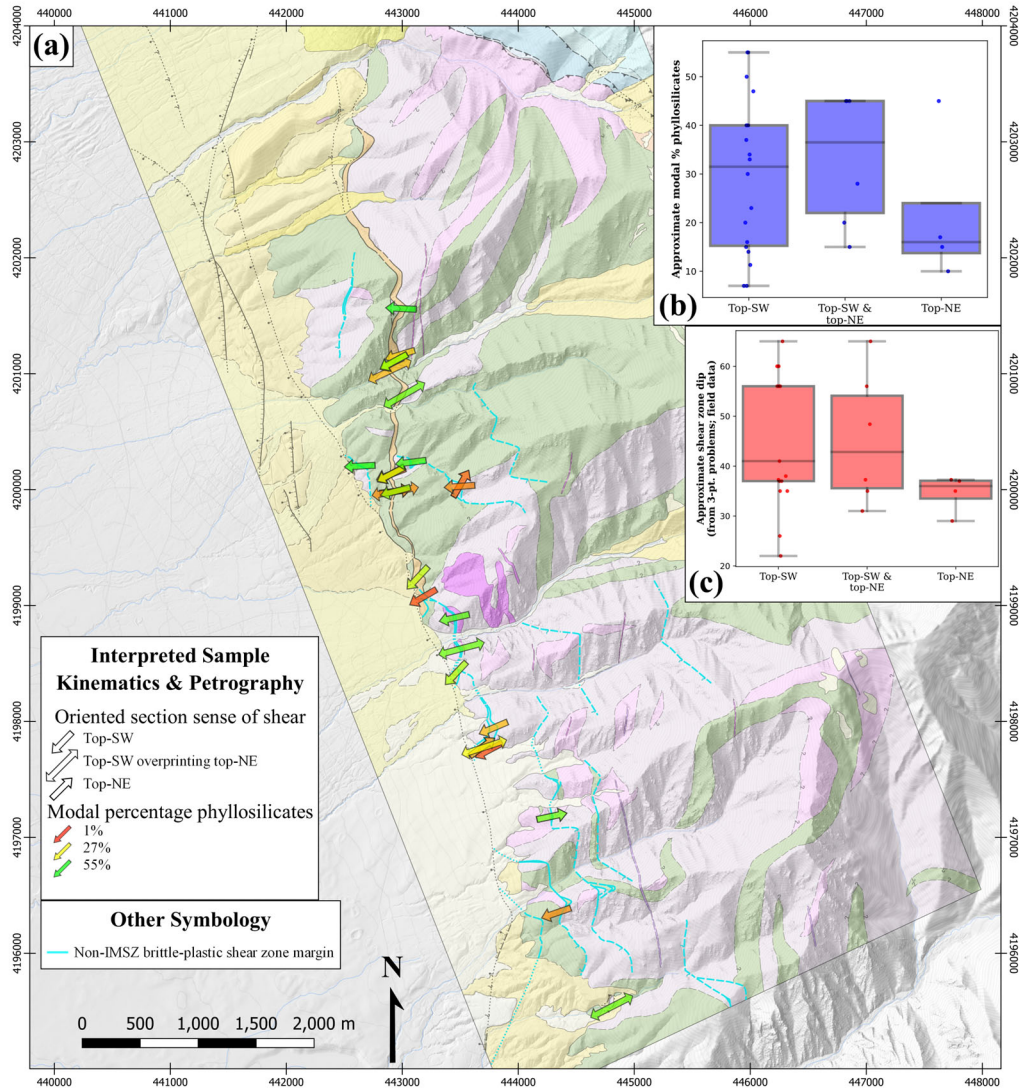


Figure 16. Map and chart showing kinematic implications of macro- and microstructural analyses of oriented samples and their source outcrops within the study area. (a) Index map with sampling locations, interpreted senses of shear, and estimated proportions of phyllosilicates from petrographic samples. Kinematics are exclusively from microstructural indicators in all samples except the southernmost sample (at the Deadman thrust), where top-SW indicators are only found in outcrop. Arrows are oriented parallel to X:Z planes of oriented petrographic sections. Non-IMSZ shear zones are highlighted in light blue. (b) Bar-whisker chart summarizing estimations of modal phyllosilicate content in samples where kinematics were interpreted. (c) Bar-whisker chart summarizing host shear zone dip angles for samples where kinematics were interpreted. Dips are calculated from three-point problems for map-scale shear zones or from direct measurements of shear zone boundary orientations for non-map-scale shear zones.

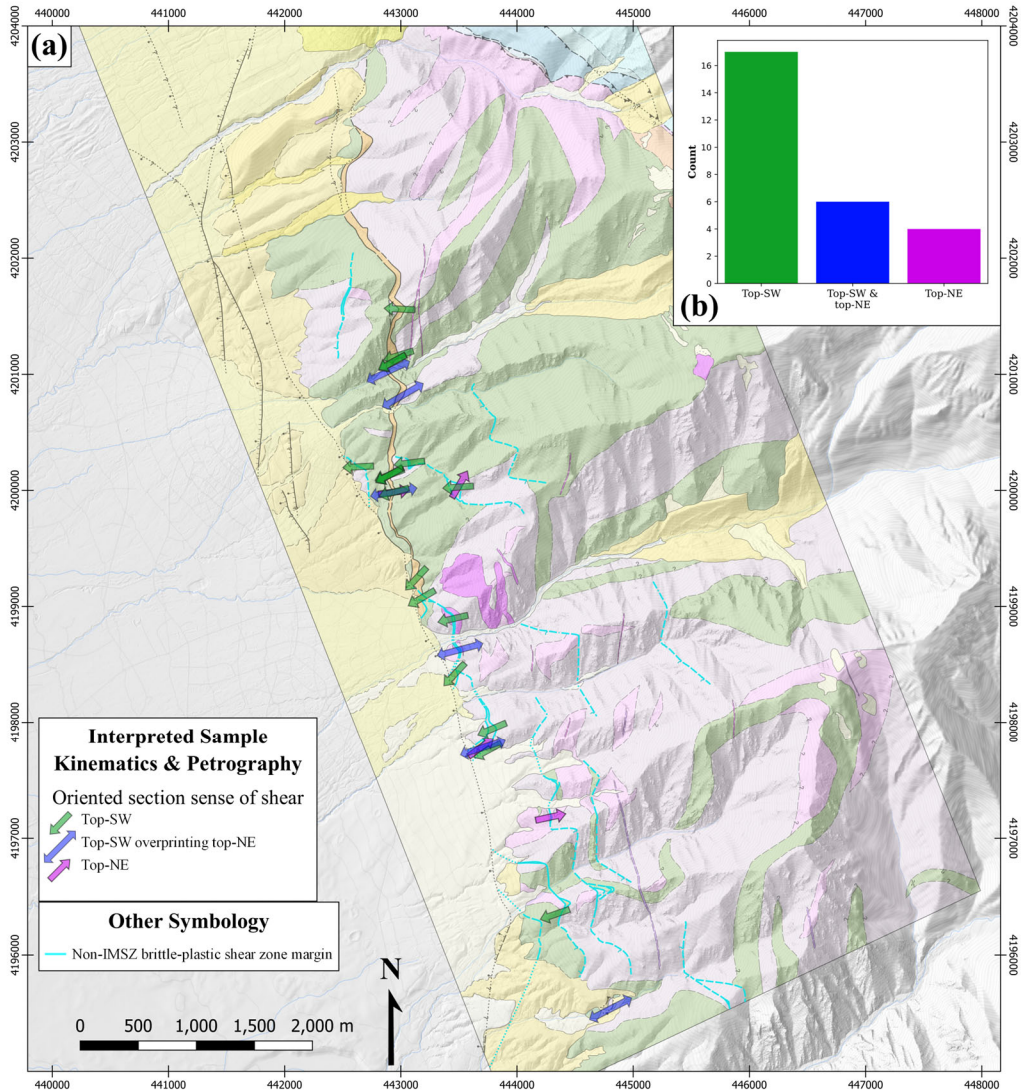


Figure 17. Simplified version of Fig. 16. (a) Map showing IMSZ, non-IMSZ shear zones, and sample locations where compelling microstructural kinematic indicators were found in thin section, with kinematics denoted by discrete coloration and arrow facing directions. (b) Bar chart showing sample counts in each kinematic category (i.e., top-SW, top-NE, or a mixture of the two).

3.2.3.2. Other Shear Zones

Twelve additional discrete brittle-plastic shear zones (highlighted in Figures 16 and 17) were identified during mapping that appear to either splay from the IMSZ at one end or trend subparallel to it; many of these shear zones were first mapped as faults by Clement (1952). All identified non-IMSZ shear zones are thinner (1–25 m-thick) and probably less laterally extensive

(with mapped lengths between ~500 m and ~3250 m) than the IMSZ (Plate 1). Three-point calculations for the non-IMSZ shear zones indicate dips ranging from 29 to 67° W to WSW (Plate 1). As in the case of the IMSZ, many of the non-IMSZ shear zones appear to offset internal contacts within the gneissic basement of the study area, but these offsets are not useful for estimating total displacement or relative age given the gneisses' complexity and Proterozoic age (Plate 1). One shear zone (Figs. 18A, 18B) does, however, cut a stock of $P\epsilon g$ gabbro. As this shear zone displays a top-SW consistent S-C fabric in outcrop, some amount of extensional offset is likely, but its magnitude is not directly determinable based on the irregular borders of the intrusion (Plate 1, cross section D-D').

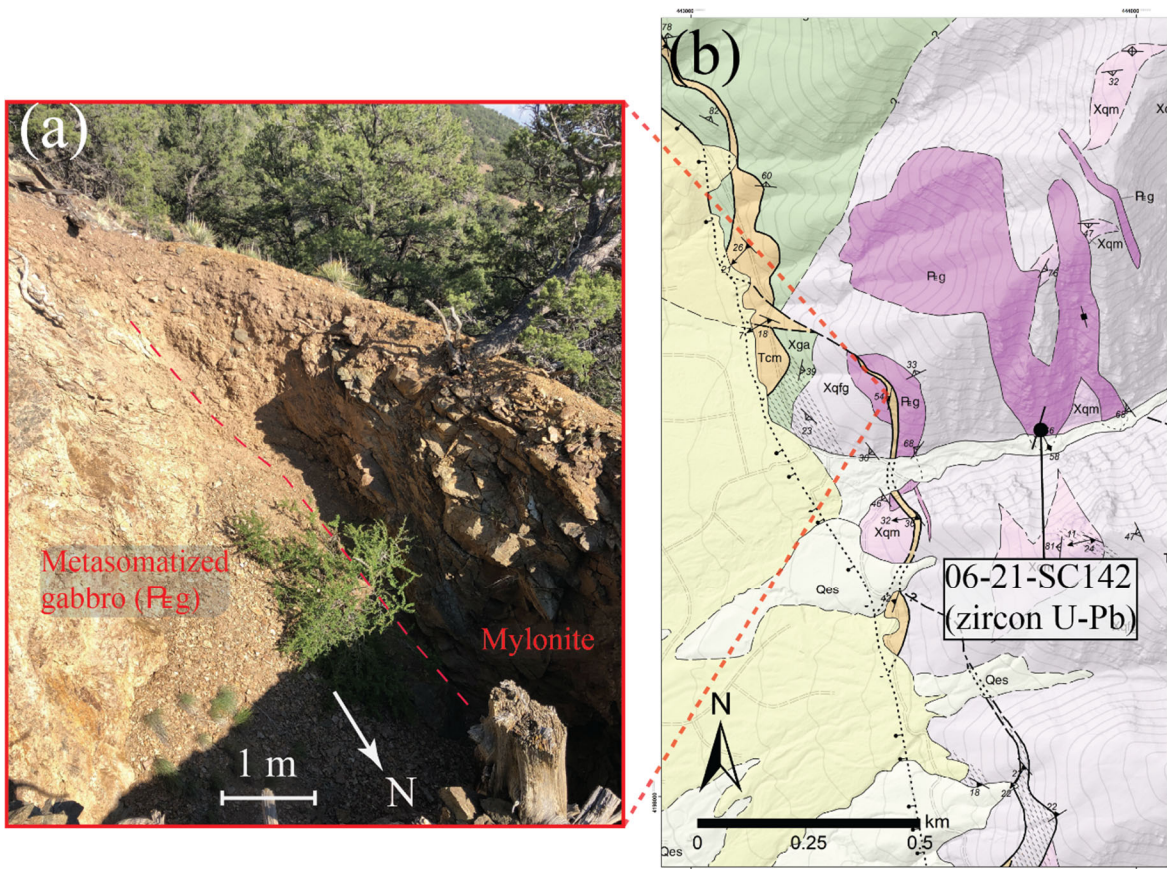


Figure 18. Explanatory map and image a key structural relationship in the study area wherein a brittle-plastic shear zone cuts a $P\epsilon g$ stock. (a) Annotated photograph (looking south) of the apparent intrusion-shear-zone contact. (b) Index map showing the intrusion and shear zone in detail, with sampling location for zircon U-Pb dating of the stock highlighted.

The non-IMSZ shear zones are more commonly bound by Xqfg and/or Xqm (Plate 1). Non-IMSZ shear zone lithology varies according to the local host rock: IMSZ-like chlorite-rich ultramylonite to mylonite (Fig. 19A) is most common where shear zones are hosted by gneissic amphibolite, and quartz-feldspar-rich protomylonite to mylonite (with foliation commonly defined by aligned bands of quartz, fractured K-feldspar, and/or white mica; Fig. 19B) is most common where hosted by quartzo-feldspathic rock (Plate 1). Some areas of quartz-feldspar-rich protomylonite are found within the relatively discrete (m-scale) boundaries of clearly identified non-IMSZ shear zones, but others appear in shear zones which are either not map scale or cannot be traced beyond a single exposure (Plate 1). Measured mylonitic foliation both within and outside of map-scale shear zones generally dip moderately to shallowly ($\sim 15\text{--}45^\circ$) W to WSW (Fig. 20A), with down-dip lineations plunging W to SW (Fig. 20B); no significant differences in mylonitic foliation and lineation orientations are apparent between chlorite-rich and quartz-feldspar-rich non-IMSZ mylonites (Fig. 20). As in the case of the IMSZ, shear zone boundaries generally cut across gneissic foliation, and measured mylonitic foliation is consistently $\geq 10^\circ$ shallower dipping than the shear zone margins (Figs. 14A, 14B). Macro-scale S-C fabrics and C' shear bands are variably well-developed within non-IMSZ shear zones, and these fabrics are locally compatible with top-SW (normal-sense; Fig. 19A) kinematics, top-NE (thrust-sense; Fig. 19B) kinematics, or both, with differing kinematics along strike in the same shear zone or even the same outcrop (Figs. 16, 17). Top-NE S-C fabrics appear to be more common in quartz-feldspar-rich protomylonites (Figs. 16, 17, 19B), especially outside of map-scale, interpretable shear zones. Besides local variations in modal mineralogy few substantive differences are clear between the IMSZ and other shear zones.

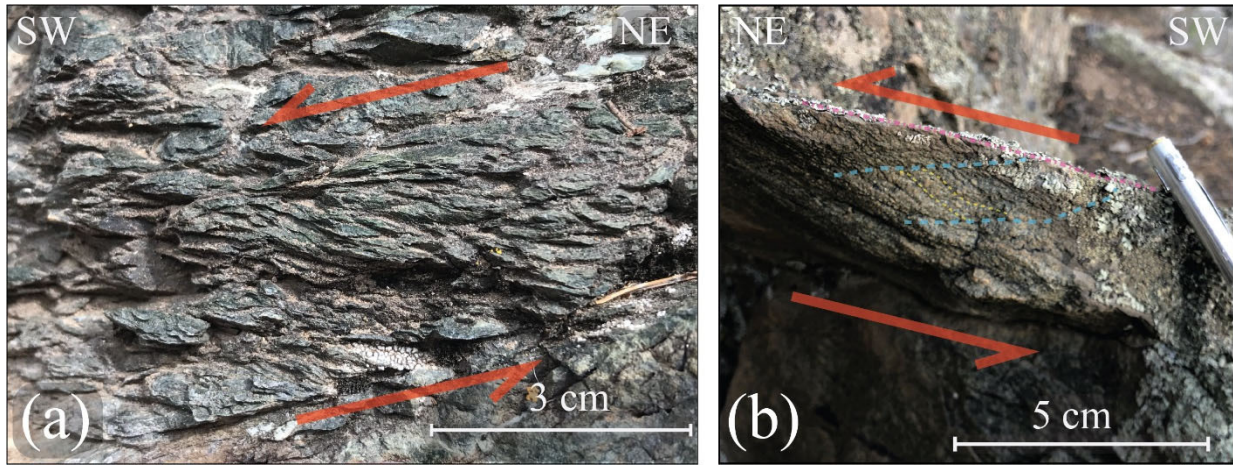


Figure 19. Photos of outcrop-scale S-C, S-C-C' fabrics in non-IMSZ brittle-plastic shear zones; annotated to indicate interpreted senses of shear. (a) A discrete cm-scale non-IMSZ shear zone with well-developed S-C fabric compatible with top-SW kinematics. (b) Outcrop of quartz-feldspar-rich protomylonite within a map-scale non-IMSZ shear zone, displaying S-C-C' fabric compatible with top-NE kinematics.

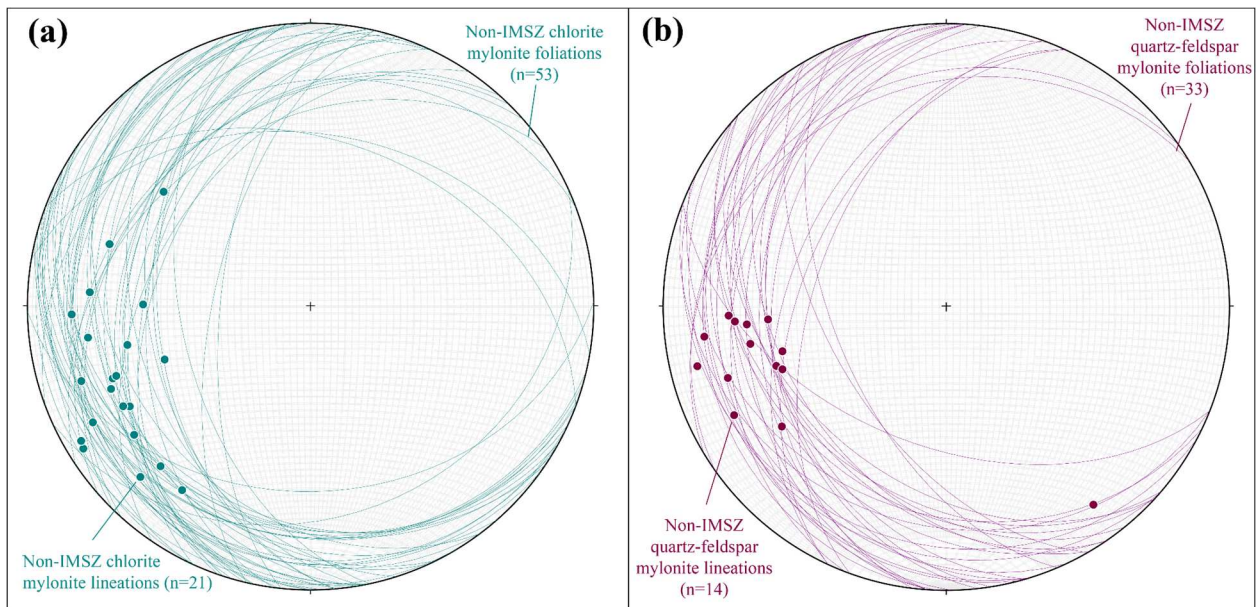


Figure 20. Equal-area stereonet-style plots showing measured mylonitic foliation and lineation in non-IMSZ brittle-plastic shear zone within the study area. (a) For chlorite-rich mylonites and ultramylonites. (b) For quartz-feldspar-rich protomylonites and mylonites.

3.2.4. Rift-related Brittle Regime Structures

3.2.4.1. Sangre de Cristo Fault System

The Sangre de Cristo fault system is locally expressed as a network of normal faults that run NNW-SSE to NE-SW along and off the range front within the study area (Plate 1).

Relatively linear, SW-side-down scarps suggest that faults constituent to this system dip to the southwest at Andersonian angles (i.e., $\sim 60^\circ$ per Anderson (1905); corroborated at depth to the southwest by Kluth & Schaftenaar (1994)) angles (Plate 1). Scarps and aeromagnetic data suggest that faults off the range front commonly splay off of, or share relay ramps with, a primary range-bounding fault (deemed the “Sangre de Cristo fault” proper for the purposes of this study) at the approximate edge of bedrock exposure in the study area (Plate 1). The absolute magnitude of offset along this fault is unclear for lack of harder geophysical (i.e., seismic) constraints, though other researchers have estimated displacements of at least ~ 250 m for the main range-bounding fault to the S of the study area (e.g., Kluth and Schaftenaar, 1994). Faults or fault segments accommodating more top-SW displacement than the interpreted primary range-bounding fault may be obscured by scarp erosion or by deposits of young alluvial-eolian sediment.

The Sangre de Cristo fault system truncates all mapped shear zones within the study area, including the IMSZ to at its southern end (Plate 1). The shear zones strike subparallel to the Sangre de Cristo fault and are more densely spaced towards the Sangre de Cristo fault system, culminating in several discontinuous exposures of SW-dipping chlorite mylonite that appear within ~ 50 m of the trace of the Sangre de Cristo fault (Plate 1) and have been interpreted by some previous workers (e.g., Clement, 1952) as representing the footwall of the fault itself. These exposures are instead interpreted in this study as being older brittle-plastic shear zones that are cut by the Sangre de Cristo fault system (Plate 1).

3.2.4.2. Outcrop-scale Structures

Fault planes measured in the study area and outside of the Paleozoic section are much less consistently oriented than those within it (Figs. 12A, 12C), and these data fail to yield

Linked-Bingham fault plane solutions consistent with the known geologic history of the area when considered in aggregate. A subset of fault planes measured in basement units and within shear zones is, however, compatible with NE-SW-directed extension along SW-dipping normal faults (Fig. 21A). These faults are consistent with the mapped orientation of the larger Sangre de Cristo fault and presumably reflect the prevailing local stress regime. Such conditions (i.e., NE-SW-directed σ_3) could also be compatible with the development of some of the joint sets in the Proterozoic basement units of the study area, which commonly strike N-S to NW-SE (Fig. 21B). ~E-W-striking joints measured within shear zones (Fig. 21B) in the study area are likewise enigmatic and may be an artefact of under-sampling.

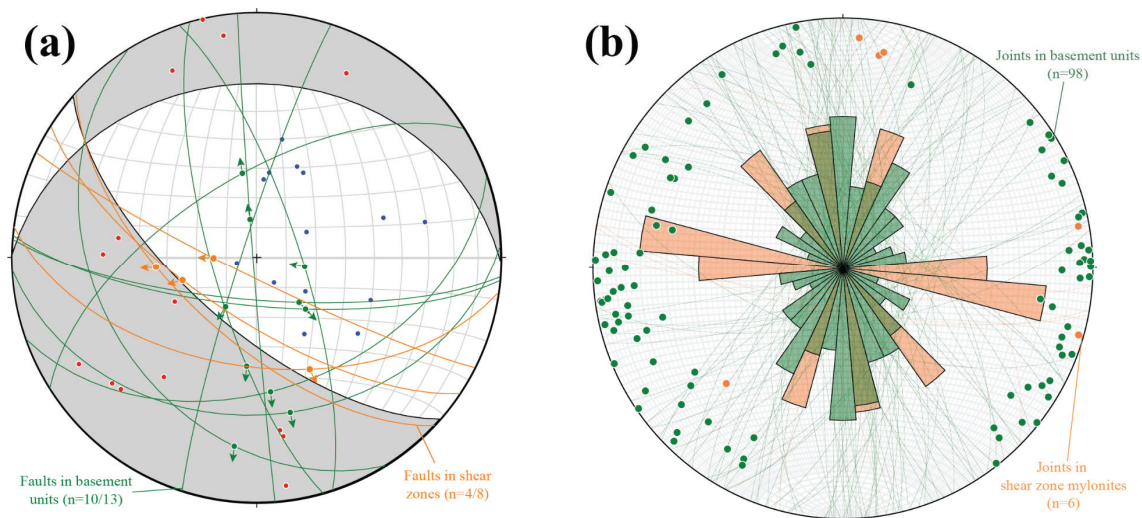


Figure 21. Equal-area plots showing outcrop-scale structures that are potentially associated with extensional, rift-related faulting. (a) FaultKin plot showing a subset (n=14/21) of basement- and shear-zone-hosted fault planes that are compatible with NE-SW extension. (b) Stereonet plot showing (via rose diagram) strike orientation distributions for joint measurements within basement units and shear zones in the study area.

3.3. Minimum Displacement Estimates

The distribution of θ' angles for stations that passed the automated checks (i.e., with calculated X directions trending sub-parallel to local measured mylonitic lineations, as outlined in Section 2.2) is roughly consistent with that of all waypoints, including those that failed (Fig.

22). A very small population ($n=4/39$; 10.3%) of stations where foliation dips more steeply than calculated shear zone margins is notably not represented in the ‘passing’ θ' angles (Fig. 22). These are assigned negative θ' values in Figure 22 and are theoretically consistent with top-NE kinematics. ‘Passing’ stations ($n=11/39$; 28.2%) have a median calculated θ' value of 30.9° , and all stations (passing and non-passing) have a median calculated θ' value of 25.8° .

Calculated minimum displacement estimates from five stations out of 18 total along the IMSZ passed the geometry validity check (Figs. 22, 23). All IMSZ foliation measurements represented in this “valid” estimated displacement dataset are from areas where top-SW fabrics were observed to be predominant in outcrop. These top-SW (normal-sense) minimum displacement estimates range from 84 to 187 m, with generally similar displacement estimates from mutually adjacent segments (e.g., Figs. 23A, 23B N of Spanish Creek, Figs. 23C, 23D along Spanish Creek) and larger estimates closer to the N (i.e., Figs. 23A, 23B) and S (i.e., Fig. 23E) ends of the mapped IMSZ than at the center (i.e., Figs. 23C, 23D). Relatively high (i.e., $\sim 25^\circ$ – 40°) θ' angles for these analyses suggest simple-shear dominated deformation.

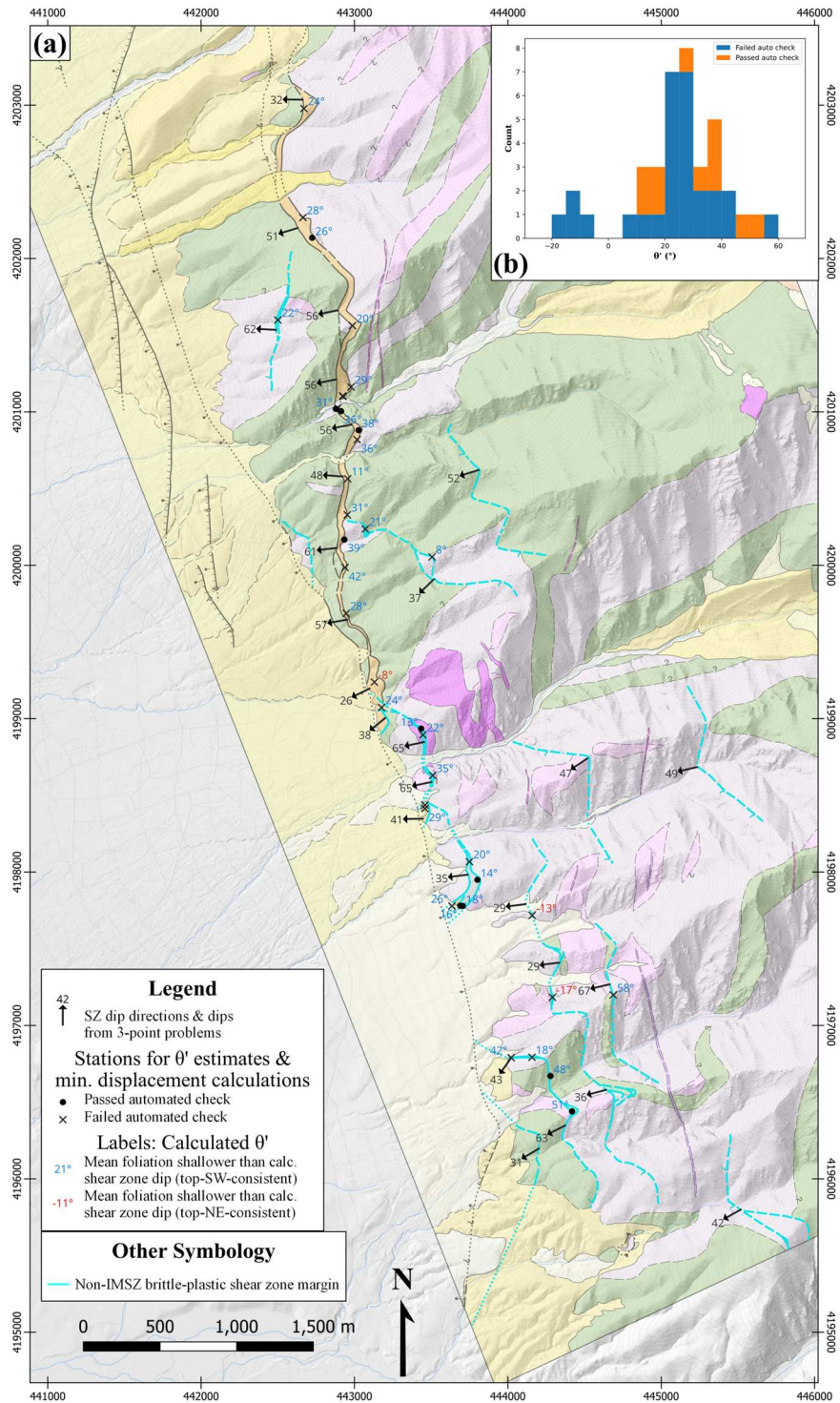


Figure 22. Calculated shear zone orientations and geolocated calculated θ' angles. (a) Map showing results of automated (using DEM in QGIS) three point shear zone orientation calculations, as well as θ' angles used in minimum displacement calculations. (b) Histogram showing distribution of calculated θ' angles, with waypoints where results passed or failed automated checks (Sect. 2.2) delineated by color. θ' values where foliation is shallower than local shear zone boundaries (consistent with normal-sense shear) are considered to be positive and colored blue. θ' values where foliation is steeper than local shear zone boundaries (consistent with reverse-sense shear) are considered to be positive and colored red.

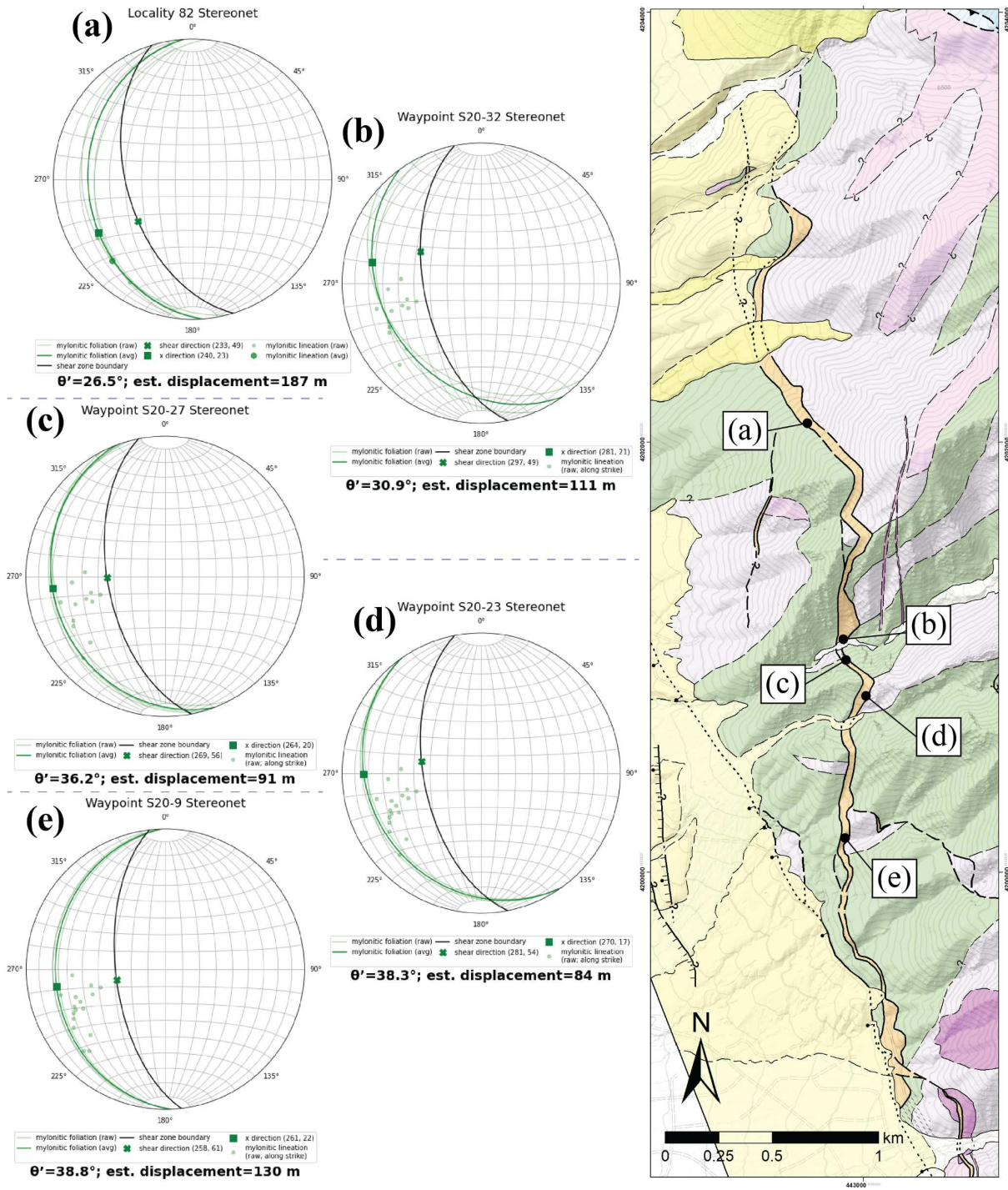


Figure 23. Summary of IMSZ displacement estimates. (a-e) Geolocated per-station stereonet plots showing key input variables (e.g., raw and eigenvector-best-fit mylonitic foliation extracted from shear zone segments; shear zone boundaries calculated via automated three-point problems) and results (i.e., calculated shear directions, X-directions, θ' angles, and displacement estimates) from scripted shear zone displacement estimate calculations.

Minimum displacement estimates from three segments out of 21 total along non-IMSZ shear zones passed the validity check (Figs. 22, 24). Eigenvector best-fits of mylonitic foliation orientation data with substantial intra-segment variation (in some cases likely due to mixtures of top-NE- and top-SW-consistent foliations) commonly produced anomalously oriented calculated shear directions and thus resulted in the elimination of many non-IMSZ shear zone segments. Outcrops within two of the “valid” segments (Figs. 22, 24A, 24C) displayed fabrics dominantly consistent with top-SW shear. The other segment (Fig. 24B) notably represented only outcrops from within a brittle-plastic shear zone cutting a stock of Peg (i.e., Fig. 18), and fabrics here were exclusively consistent with top-SW shear. Estimated displacements for non-IMSZ shear zones range from 36 m (Fig. 24A) to 141 m (Fig. 24B). A larger, generally lower range (i.e., 13° – 51°) of θ' angles provide a weaker and noisier signal for simple-dominated shear versus in the IMSZ. The 51° θ' angle for the shear zone shown in Figure 21C, in particular, is likely too high for a valid estimate of minimum displacement.

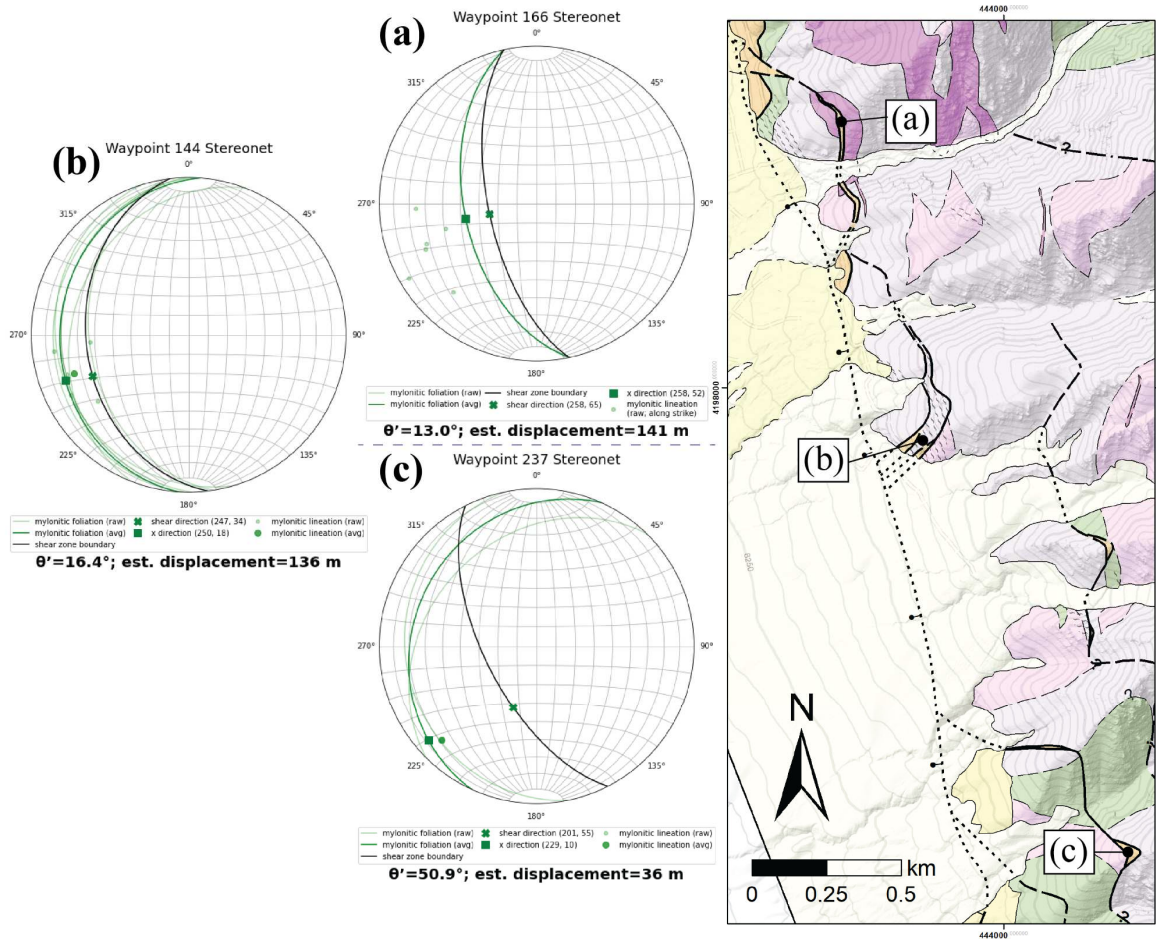


Figure 24. Summary of non-IMSZ shear zone displacement estimates. (a-c) Geolocated per-station stereonet plots showing key input variables (e.g., raw and eigenvector-averaged mylonitic foliation extracted from shear zone segments; shear zone boundaries calculated via automated three-point problems) and results (i.e., calculated shear directions, θ' angles, x-directions, and displacement estimates) from scripted shear zone displacement estimate calculations.

3.4. Microstructural Analysis

Petrographic samples (Figs. 25-28) from the IMSZ and other basement-hosted brittle-plastic shear zones (i.e., Fig. 16) vary in composition and degree of mylonitization, with samples ranging from protomylonitic quartz-feldspar-rich gneiss to chlorite ultramylonite. Protomylonitic rocks generally contain limited proportions (i.e., as little as ~1%) of white mica after plagioclase, and quartz commonly represents the interconnected weak phase in these rocks. Proportions of white mica tend to increase with greater comminution, and incipient sericitization of plagioclase concentrated along comminutional brittle shear bands with evidence for fluid channelization is

preserved in some cataclastic-protomylonitic samples (e.g., Fig. 28C-D). Chlorite, often in combination with white mica, is a common major component of more mylonitic (i.e., mylonite to ultramylonite) rocks (Fig. 25; Table 1). Though chlorite and white mica, in joint proportions of up to 55% (i.e., Fig. 16; Table 1), usually form the interconnected weak phase of ultramylonitic samples (e.g., Figs. 26B, 27B), variably scaled (i.e., mm- to outcrop-scale) domains where recrystallized quartz is the interconnected weak phase (e.g., Figs. 27F, 28A, 28E) are identifiable in many high-strain mylonitic shear zone samples and outcrops. Quartz, pervasively sericitized relict plagioclase, and K-feldspar (almost invariably displaying some degree of brittle fracturing) are the primary porphyroclasts identified in shear zone mylonites and appear in variable proportions (Fig. 25). Quartz porphyroclasts, lenses, and smaller ribbons are commonly subangular (e.g., Fig. 26B), and locally feldspar records pervasive cataclasis; as a whole these conditions give many thin sections the appearance of having evolved from cataclastically fractured rock (e.g., Fig. 24D). Apatite, epidote, calcite, and iron oxide are common metasomatic-hydrothermal (i.e., commonly appearing in veins) accessory phases within mylonite-ultramylonite samples (Fig. 19); mutually cross-cutting relationships with shear fabrics indicate that the latter two locally appear as synkinematic veinlets (e.g., Fig. 28F).

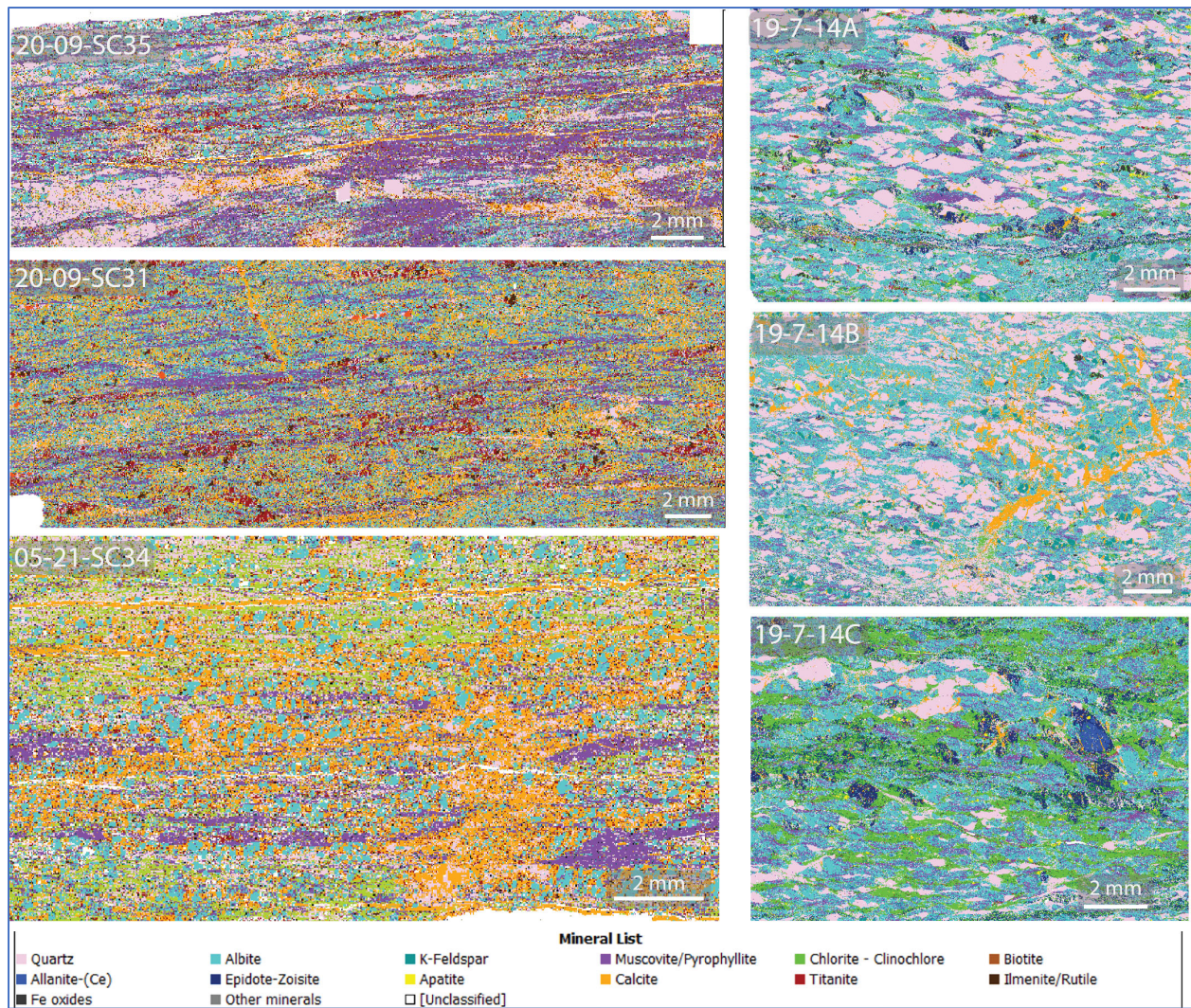


Figure 25. Tescan modal mineralogy maps for petrographic thin sections of mylonitic samples from the study area.

Table 1. Tescan-derived approximate modal mineralogy for mylonitic samples shown in Figure 19.

Area % of phase [%]	19-7-14a	19-7-14b	19-7-14c	20-9-SC31	20-9-SC35	05-21-SC34A
Quartz	37.5	38.1	17.5	11.72	26.78	21.43
Albite	32.1	32.5	32.4	26.96	17.18	17.18
Muscovite/Pyrophyllite	7.9	4.3	8.6	18.35	29.84	12.29
Chlorite	7.2	5.9	21.3	2.79	4.04	16.71
Epidote-Zoisite	5.6	4.6	7.3	1.96	0.49	0.69
K-Feldspar	1.8	3	3.2	1.39	1.76	0.61
Calcite	1.3	5.1	1.7	20.19	7.58	20.76
Biotite	0.9	1.1	2.1	1.12	2.61	2.61

Fe oxides	0.9	0.4	0.1	6.8	4.53	3.67
Titanite	0.7	0.1	0.7	0	0	0
Apatite	0.3	0.2	0.5	4.77	0.95	0.34
Ilmenite/Rutile	0.1	0.1	0.3	2.2	1.32	0.49
Zircon	0	0	0	0.02	0.01	0
Other minerals	0.2	0.1	0.2	0.73	1.8	2.12
[Unclassified]	3.5	4.5	4.1	1	1.11	1.1
Total	100	100	100	100	100	100

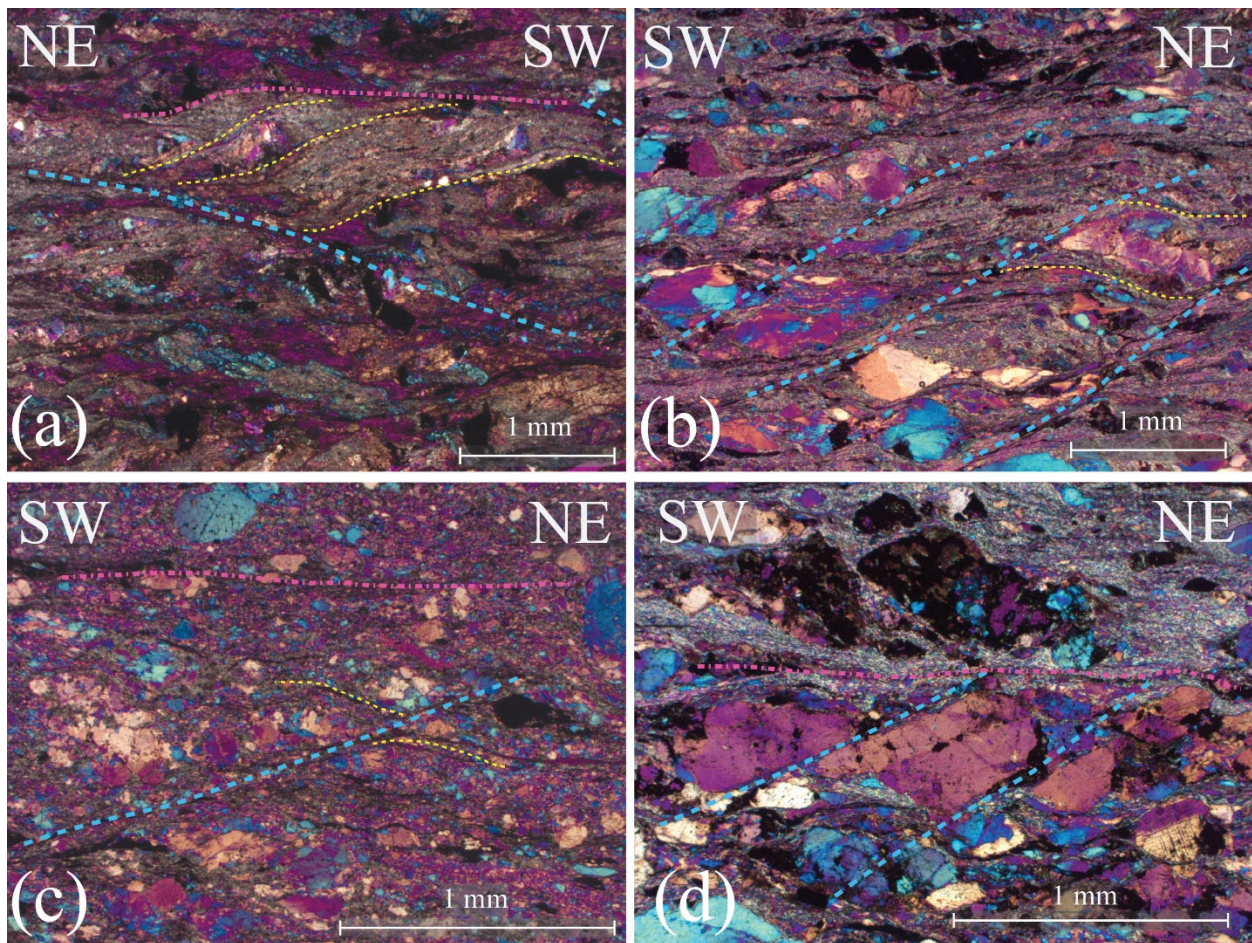


Figure 26. Representative photomicrographs of microstructural kinematic indicators for top-SW shear in the study area. (a, b) Samples 20-09-SC30A, 06-21-SC155: Extremely well-developed top-SW S-C-C' fabrics, with apparent overprinting of dynamically recrystallized quartz ribbons in b. (c) Sample 06-21-SC149: Well-developed top-SW C'>S-C fabric, with subangular quartz porphyroclasts and apparent further fracturing of dynamically recrystallized quartz. (d) Sample 06-21-SC155: Brittle dissection of quartz and K-feldspar porphyroclasts along top-SW C' shear bands.

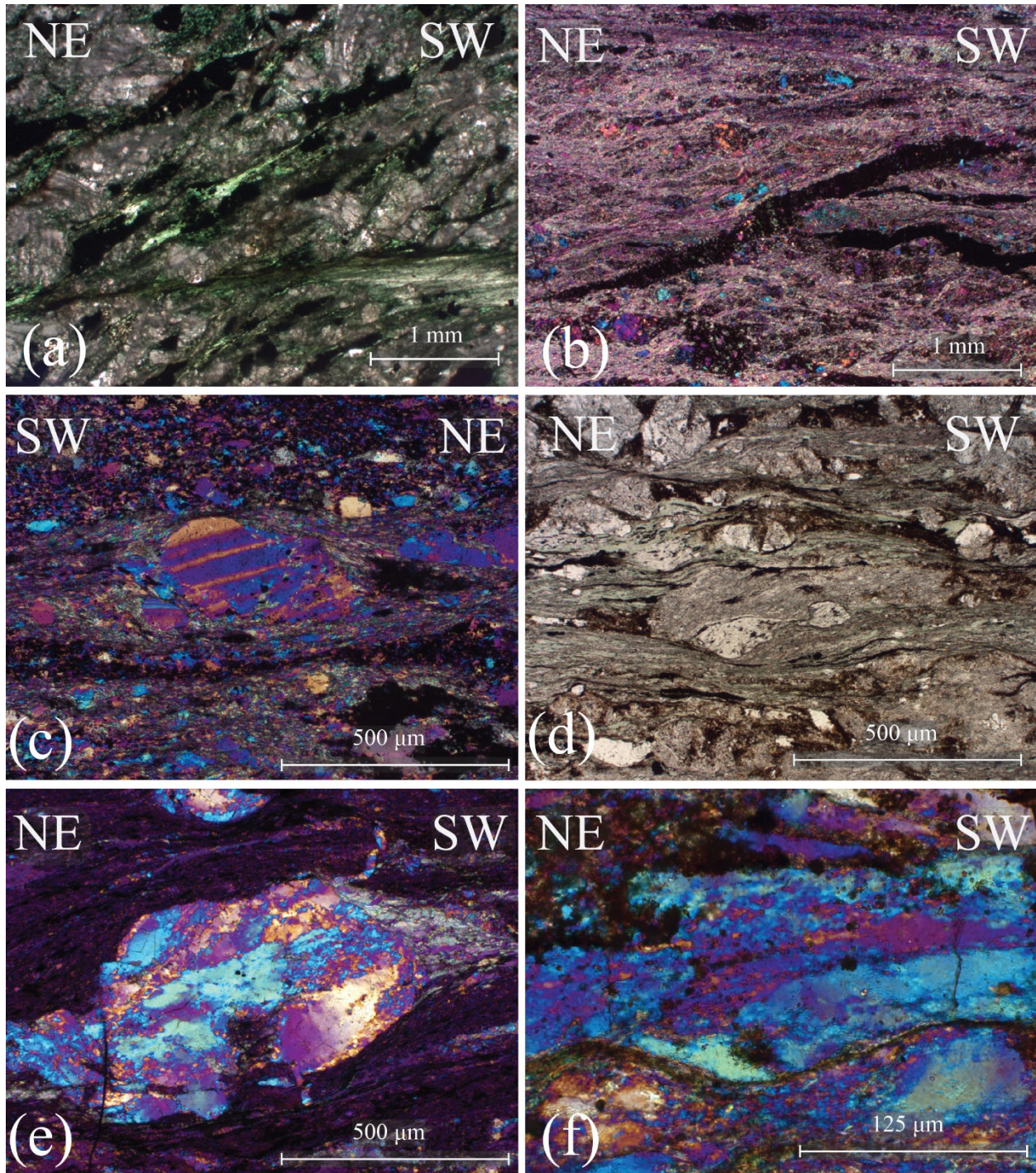


Figure 27. Additional representative photomicrographs of top-SW kinematic indicators from brittle-plastic shear zones in the study area. (a) Sample 08-21-SC268: Well-developed S-C fabric in chlorite cataclasite-mylonite, with prominent C bands (thick section photomicrograph). (b) Sample 06-21-SC167: Sigmoidal mica foliae alongside Fe-oxide veins dissected into top-SW sigmoids. Small, elongate, dynamically recrystallized quartz porphyroclasts. (c) Sample 06-21-SC149: Fractured, rotated K-feldspar top-SW σ -porphyroclast with white mica tails. (d) Sample 05-21-SC34B: Fractured altered plagioclase \pm quartz porphyroclasts entrained in chlorite-rich top-SW S-C-C' fabric. (e) Sample 20-09-SC26: Quartz sigmoid with top-SW asymmetry and mixed BLG-SGR dynamic recrystallization. (f) Sample 20-09-SC35: Oblique quartz grain shape fabric consistent with top-SW kinematics in a recrystallized and locally fractured quartz ribbon.

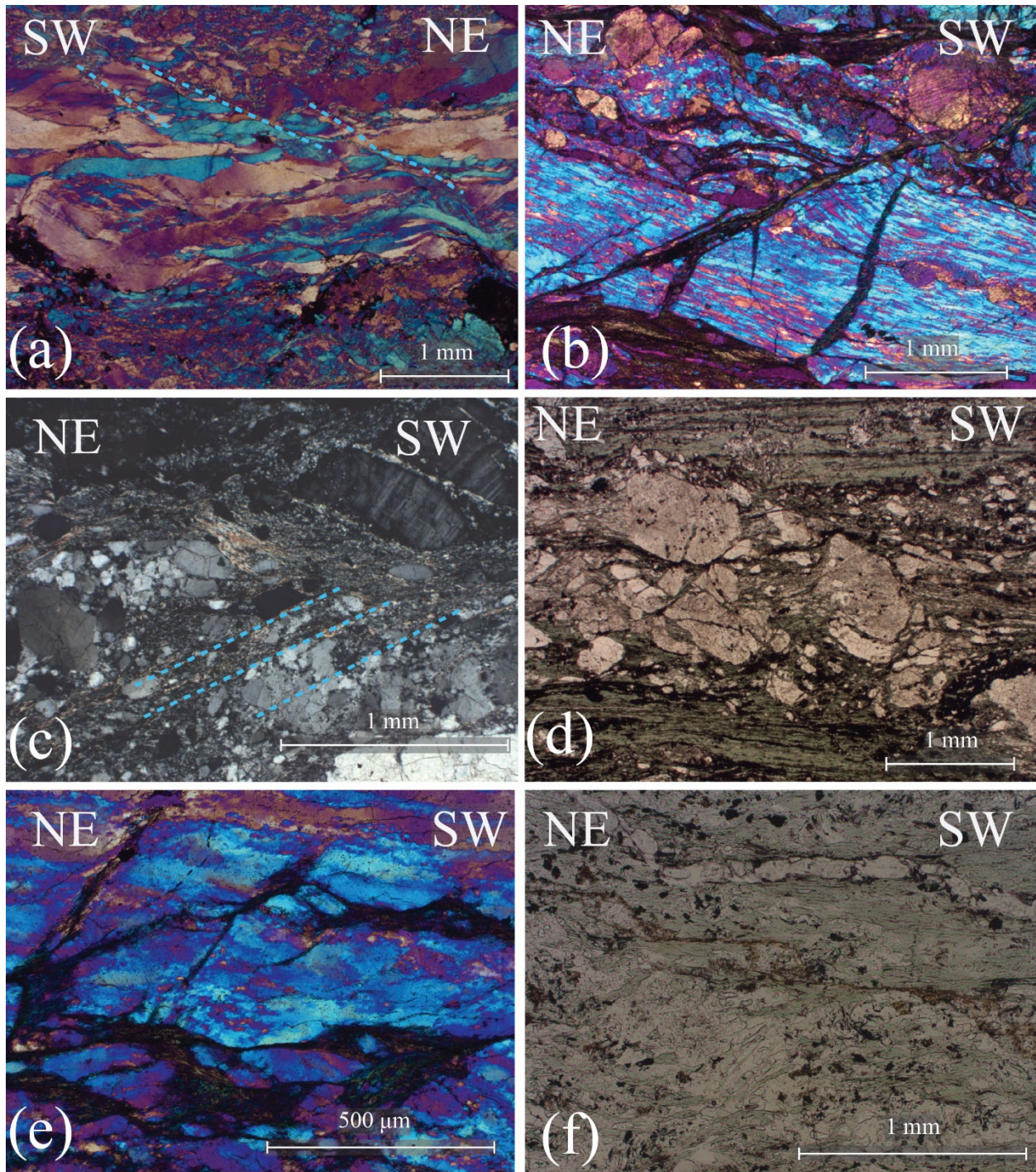


Figure 28. Representative photomicrographs of microstructural top-NE kinematic indicators in the study area. (a) Sample 05-21-SC34C: S-C-C' fabric in SGR-dynamically recrystallized quartz, with well-developed CPO. (b) Sample 05-21-SC29: Brittle fracturing of dynamically recrystallized quartz ribbon along top-NE C' shear band. (c) Sample 09-21-SC578: Brittle fracturing of quartz and K-feldspar along top-NE C' bands in protomylonite, with incipient alteration of feldspars to white mica. (d) Sample 06-21-SC144: Fractured K-feldspar porphyroclast(s), bounded above and below by high-strain chlorite-rich ~C bands. (e) Sample 05-21-SC29: Possible late(?) -kinematic brittle fracturing of top-NE, SGR-recrystallized quartz ribbons with top-NE-consistent oblique grain-shape fabric. (f) Sample 05-21-SC58: Top-NE shearing of syn-kinematic calcite veins and Fe-oxide in chlorite-quartz mylonite with well-developed C shear bands.

Microstructural kinematic indicators in shear zone samples are similar to those visible in outcrops, with top-SW S-C \pm C' fabrics (e.g., Figs. 26, 27) variably overprinting top-NE S-C fabrics (i.e., Fig. 28). Top-NE fabrics and domains preserving top-NE fabrics in samples with mixed kinematic indicators (e.g., Fig. 28E) generally contain less phyllosilicate (i.e., 5–20%; Fig. 16) than those overprinted by top-SW fabrics. Rarely (e.g., Figs. 28E, 28F), chlorite mylonites with brittle-plastic fabrics and interconnected phyllosilicate exclusively display kinematic indicators consistent with top-NE shear. Domains with kinematic indicators suggesting top-NE shear disproportionately record plastic quartz deformation through dynamic quartz recrystallization, sometimes with fully developed S-C-C' fabrics preserved entirely within dynamically recrystallized quartz ribbons and domains (Fig. 28A). In most samples with interpreted top-NE kinematics, ribbons of quartz are dominated by relatively small (i.e., 10–20 μm) subgrains with well-developed grain-shape preferred orientations oblique to interpreted sample kinematics (e.g., Fig 28B, 28E). Chaotic arrangements of smaller (i.e., $\leq 10 \mu\text{m}$), randomly oriented quartz grains also commonly appear along internal and external margins of elongate quartz crystals and porphyroclasts (e.g., Fig. 28E). These textures suggest a combination of subgrain rotation (SGR) and bulging (BLG) dynamic quartz recrystallization. Of the two, the latter is probably more common within samples from the study area, but the former accounts for a greater volume of quartz recrystallization where present. Top-NE fabrics are not exclusively plastic; many samples record brittle-cataclastic fracturing through angular quartz porphyroclasts with minor recrystallization (e.g., Fig. 28D), while others record late-kinematic top-NE-consistent brittle overprinting of dynamically recrystallized quartz (e.g., Fig. 28B) and others record predominantly cataclastic textures with very low ($\sim 1\text{--}5\%$) degrees of dynamic quartz recrystallization (e.g., Fig. 28D). Other kinematic indicators besides S-C-C' fabrics

include mica fish, σ -porphyroclasts with mica tails (e.g., Fig. 28C), and sheared syn- to late-kinematic calcite veinlets (Fig. 28F). Though top-NE-dominant samples tend to contain more quartz, feldspar, and white mica than top-SW dominant samples, multiple sample of chlorite-quartz mylonite (e.g., Figs. 28D, 28F) with consistently top-NE kinematic indicators display fabrics (e.g., porphyroclasts bounded by high-strain C-foliations) that appear to either post-date or have developed coevally with chloritization. These samples suggest that the compositional frameworks for chlorite-rich top-SW-dominant shear zones may predate their fabrics.

The most characteristic microstructural kinematic indicators for top-SW fabrics in the study area are C' shear bands, usually either hosted within or lined by phyllosilicates (usually chlorite > white mica; e.g., Fig. 26). In several samples, C' shear bands cutting top-NE-consistent S-C fabrics are the only indicators for top-SW overprinting. More common, however, are fully developed, phyllosilicate-dominated S-C-C' fabrics without any relict indicators for top-NE kinematics (e.g., Fig. 26A). These fabrics may be dominant on an outcrop scale (as in much of the IMSZ) or be constrained to localized domains, high-strain zones, and/or shear bands where phyllosilicates form an interconnected weak phase within samples otherwise dominated by top-NE kinematic indicators. Greater modal proportions of phyllosilicates (20–55%, usually majority-chlorite) appear correlated with top-SW kinematics (Fig. 16). Fabrics in many top-SW-dominated samples preserve dynamic quartz recrystallization indicative of top-SW plastic quartz deformation, including inclined dynamically recrystallized grain shape preferred orientations (e.g., Fig. 27F) and sigmoidal elongation of quartz porphyroclasts (Fig. 27C). Top-SW S-C-C' fabrics are, however, also frequently associated with brittle reworking of quartz fabrics likely to have originated through top-NE deformation (e.g., Fig. 27A). Brittle fracturing and rotation of K-feldspar and, locally, quartz \pm partially sericitized plagioclase porphyroclasts (e.g. Fig. 26C) are

common top-SW kinematic indicators; sheared late-synkinematic calcite and Fe-oxide veins, mica fish, and σ -porphyroclasts with chlorite-white-mica tails are somewhat less common (Fig. 27C-E).

Unlike in outcrop (i.e., Fig. 8B), the single petrographic section (K-feldspar-quartz-white-mica mylonite, with white mica as the developing, interconnected weak phase) collected from the protomylonite-mylonite zone of the Deadman Creek thrust displays little kinematic evidence for top-SW displacement. Top-NE kinematic indicators include K-feldspar σ -porphyroclasts with white mica tails, preserved C' shear bands apparent in micaceous intervals, and high-angle antithetic (top-SW) shear bands. Localized, lower-angle shear bands that could otherwise be interpreted as top-SW C' bands are mutually cross cutting with top-NE-consistent bands and thus not reliable as kinematic indicators. Plastic deformation of quartz is limited to relatively minor BLG-SGR dynamic recrystallization in a minority of porphyroclasts.

3.4.1. EBSD

EBSD analyses of IMSZ mylonite samples were not uniformly successful; though all yielded misorientation data strongly indicative of quartz basal $\langle a \rangle$ slip (Fig. 29B), two out of the four quartz-rich mylonitic samples targeted have thus far failed to yield clear crystallographic preferred orientation patterns (Fig. 30). These samples may require additional data and/or sample re-processing.

The two samples that have been successfully analyzed (Fig. 29) differ in petrographically interpretable kinematics. Sample 19-7-14A is a chlorite mylonite from the IMSZ. It has a well-developed, chlorite-dominated top-SW S-C-C' fabric and isolated quartz ribbons that locally display minor domains of dynamic recrystallization and have been fractured along top-SW C' bands. A c-axis opening angle of 30° suggests a quartz dislocation creep temperature of $255^\circ \pm$

50°C for this sample using the calibration of Faleiros et al. (2016; Fig. 29A). Despite its clear top-SW S-C-C' fabric, however, the quartz asymmetry fabric of sample 19-7-14A is compatible with top-NE, simple-dominated shear (Fig. 29A; e.g., Passchier & Trouw, 2005). Sample 05-21-SC34C is a quartz-rich mylonite from the IMSZ at Independent Mine. In contrast to sample 19-7-14A, kinematic indicators in sample 05-21-SC34C are mixed, with top-NE compatible sigmoidal quartz ribbons and shear bands intermingled with much more localized domains of top-SW-compatible S-C fabrics and sigmoidal foliations. The pole figure for sample 05-21-SC34C is also compatible with top-NE, simple-dominated shear (Fig. 29B).

The samples without clearly interpretable kinematics in their EBSD lower hemisphere pole figures are 05-21-SC12C and 20-09-SC34 (Fig. 30). Sample 05-21-SC12 is of a quartz-hornblende boudin in a shear zone that splays from the IMSZ, and in petrographic thin section it displays synthetic (i.e., R or C') and antithetic (i.e., R') brittle-plastic shear bands consistent with top-SW shear, with local domains of minor quartz BLG-SGR recrystallization with an oblique grain shape fabric consistent with top-SW shear. Lower hemisphere pole figures show girdling and point-maxima that are not clearly interpretable with quartz basal <a> shearing kinematics (Fig. 30A). Sample 20-09-SC34 is of quartz-dominated ultramylonite and was collected at the mapped intersection between a non-IMSZ shear zone and the Sangre de Cristo fault (Plate 1). Fabrics visible in the petrographic thin section prepared for this sample suggest top-SW kinematics and include quartz sigmoids and C' shear bands. The sample is notably cut by a quartz vein that appears to have been partially recrystallized; recrystallized grains are broadly morphologically compatible with top-SW BLG-SGR dynamic recrystallization. EBSD analyses of this sample produce ambiguous results which could potentially be compatible with the presence of a weakly-developed c-axis girdle consistent with top-SW shear or of partial top-SW

overprinting of a top-NE-compatible crystallographic preferred orientation (Fig. 30B). More data are likely needed from this sample for less equivocal interpretation.

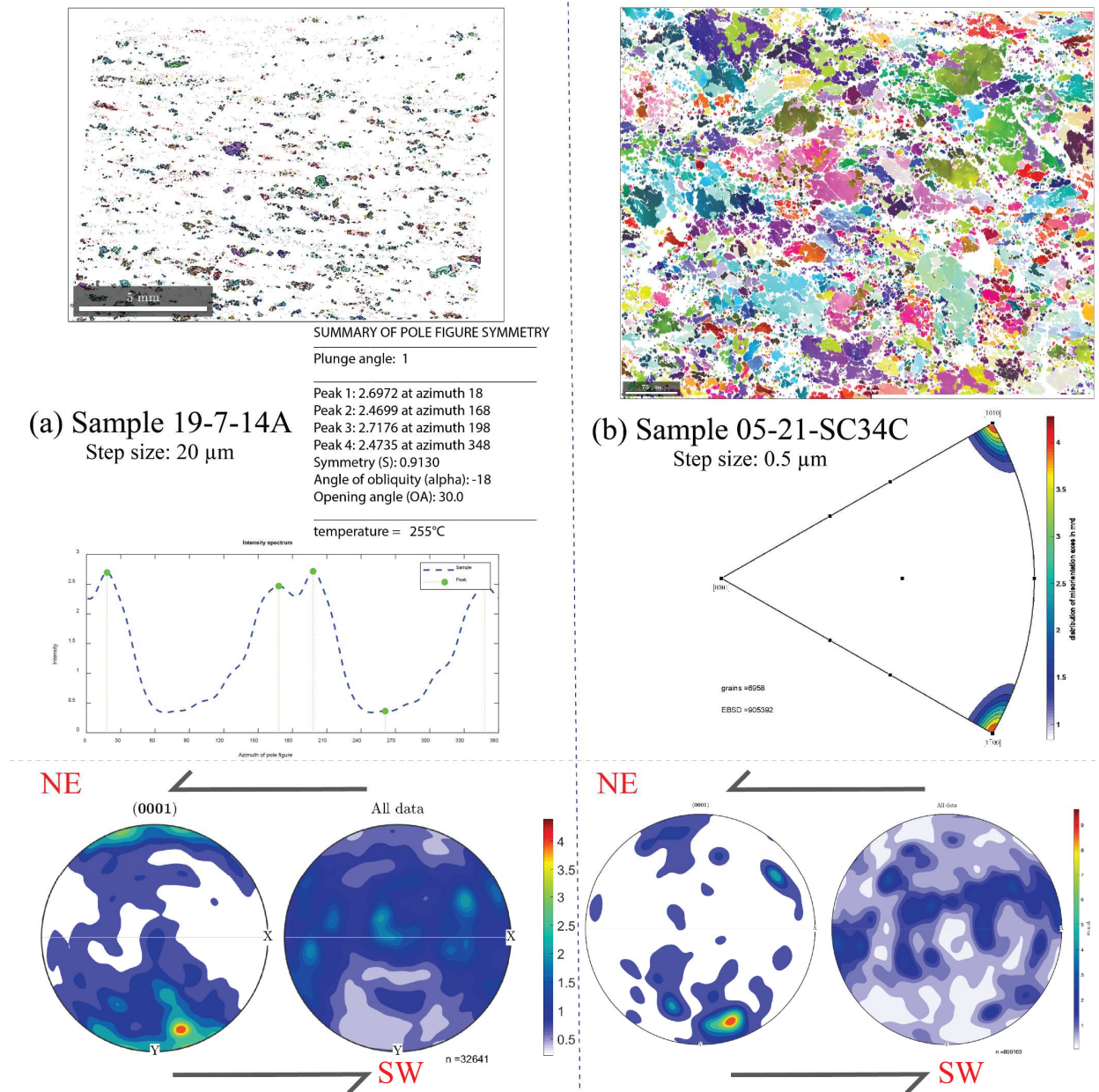


Figure 29. Selected EBSD data for oriented IMSZ mylonite samples. (a) Chlorite mylonite sample 19-7-14A, which displays spectacular chlorite-dominated top-SW S-C-C' fabric in petrographic thin section. C-axis opening angle indicates temperature of ~255 °C for dynamic recrystallization. Quartz pole figure indicates quartz basal <a>, simple-dominated top-NE shear. (b) Quartz mylonite sample 05-21-SC34C, which displays mixed kinematic indicators (e.g., top-NE quartz sigmoids; top-SW mica S-foliae) in petrographic thin section. Intracrystalline misorientations indicate basal <a> slip, with top-NE simple-dominated shear suggested by quartz pole figure.

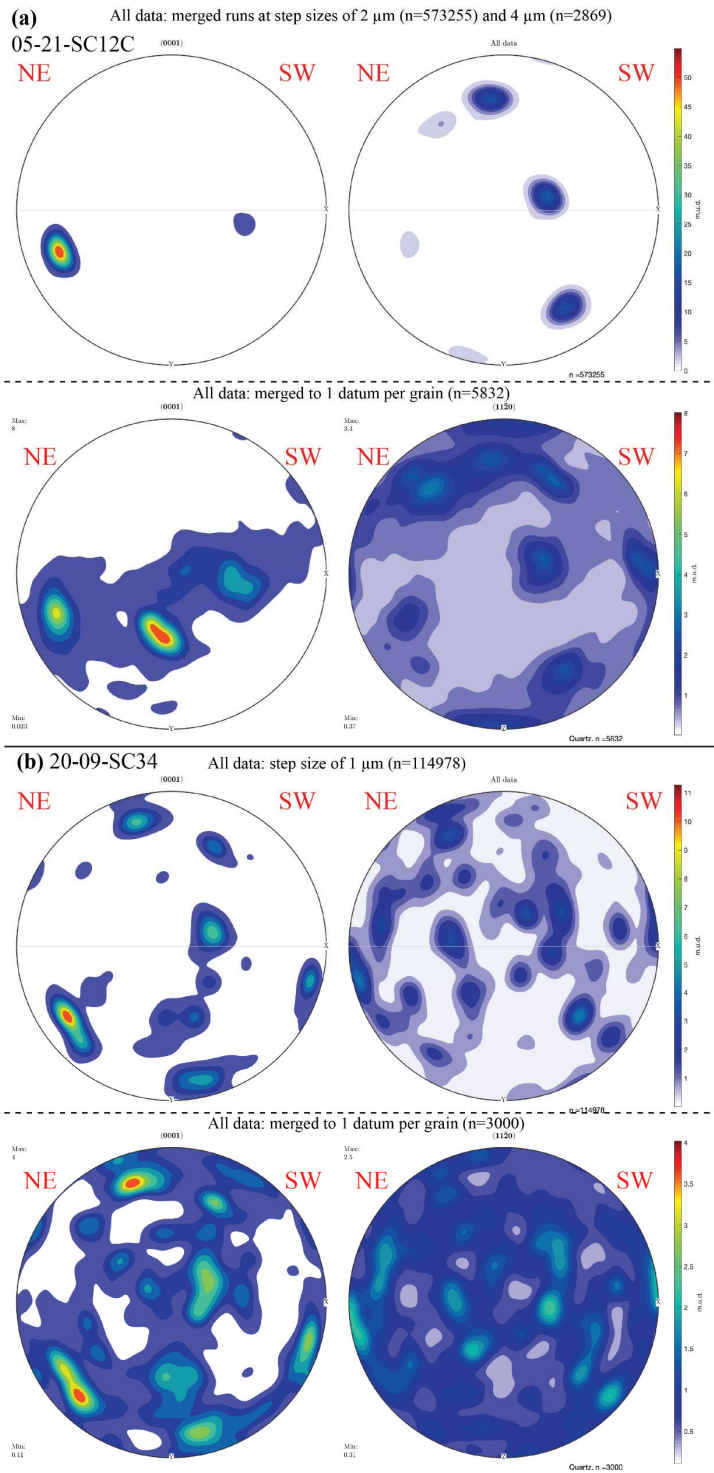


Figure 30. Additional, less interpretable lower hemisphere EBSD pole figures for samples from the study area. Top figures for (a) and (b) are compilations of all data from EBSD analyses, and lower figures are of data after reduction to one datum per quartz grain. (a) Sample 05-21-SC12C, of a quartz-hornblende boudin in a shear zone splaying from the IMSZ. (b) Sample 20-09-SC34, from a quartz-rich ultramylonite in non-IMSZ shear zone exposure adjacent to the Sangre de Cristo fault.

3.5. Geochronology and Thermochronology

LA-ICP-MS U-Pb analysis of zircon grains separated from a sample of the **Fig** stock cut by a brittle-plastic shear zone (06-21-SC142; Fig. 31) yielded 26 concordant dates ranging from the Paleoproterozoic to Late Oligocene (Fig. 32C), with inherited subpopulations from the Paleoproterozoic (~2500–1658 Ma; n=4), Mesoproterozoic (~1525–1054; n=4), and Neoproterozoic to Ordovician (~581–472 Ma; n=9). The youngest population (n=9) yields a concordia age of 25.57 ± 0.74 Ma (at 2σ with MSWD = 3.3; Fig. 32C) provides a Late Oligocene upper age constraint on the latest normal-sense shear along the brittle-plastic shear zone cutting the **Fig** stock. An overlapping pooled zircon fission track age of $26.7 + 3.6, -3.2$ Ma (with a corresponding IsoplotR radial plot age of 27.4 ± 3.1 Ma) from 19 grains from the same sample (Fig. 32C) indicates that the stock had cooled to below ~200-260 °C (approximate zircon fission track closure temperature range, e.g., Reiners & Brandon, 2006) before the beginning of the Miocene (~23.5 Ma at latest; less than ~2.8 Ma after emplacement).

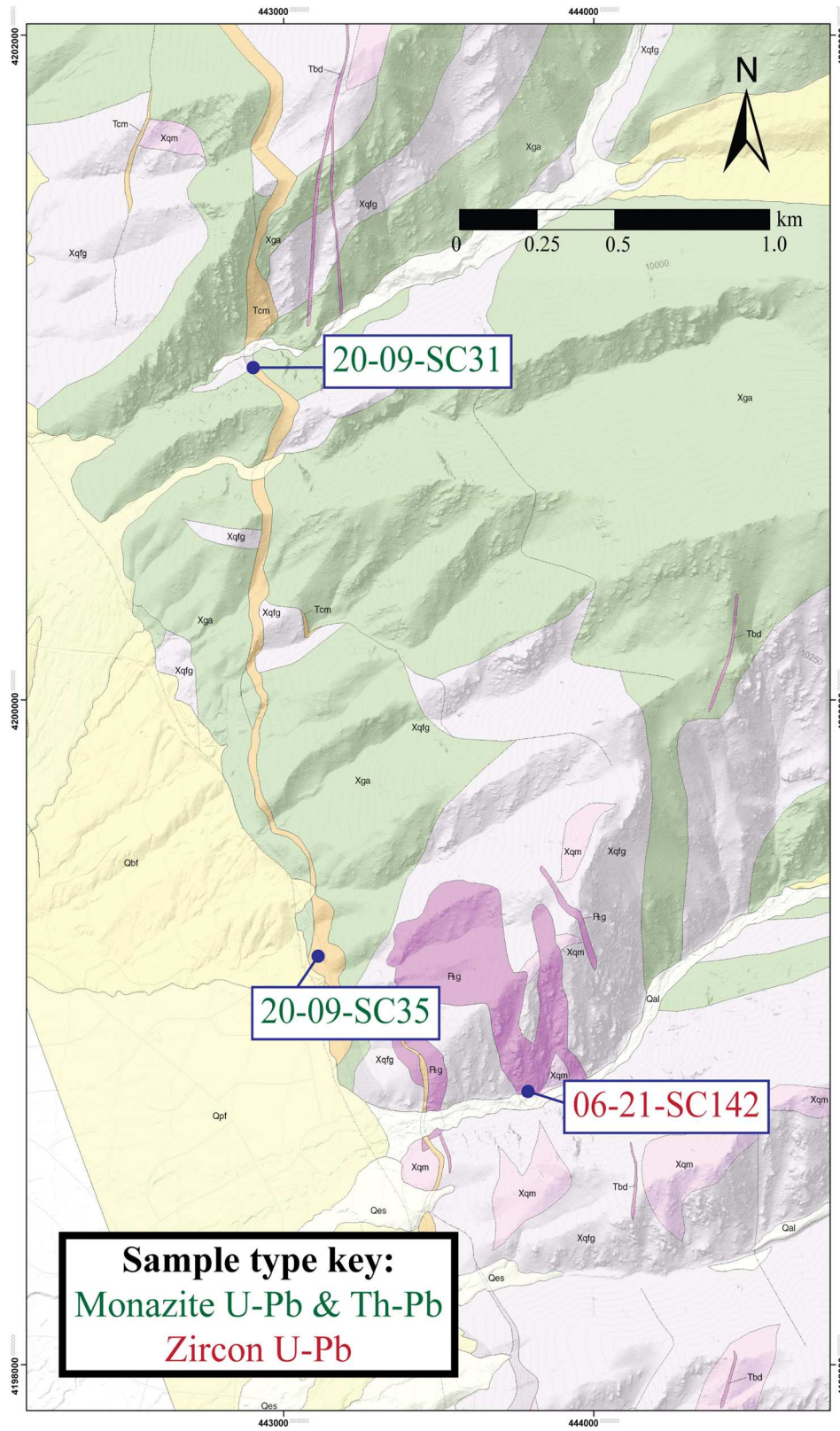


Figure 31. Index map for study area samples successfully dated via monazite U-Th-Pb or zircon U-Pb geochronology.

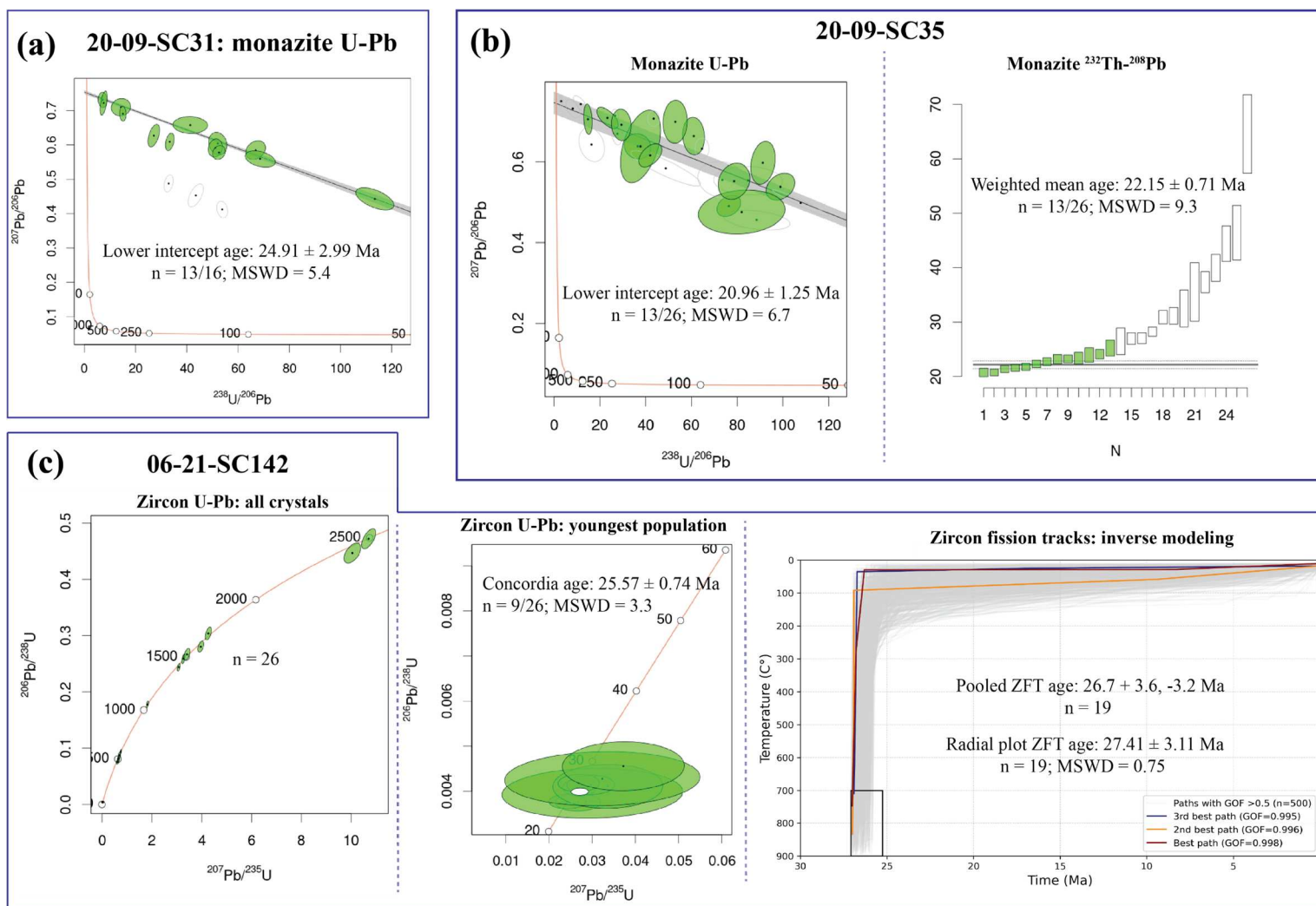


Figure 32. Geochronology analytical results for samples collected in the study area. (a) Monazite U-Pb dating of sample 20-09-SC31 with lower intercept age of 24.91 ± 2.99 Ma shown on Tera-Wasserburg discordia diagram. (b) Monazite U-Pb and Th-Pb dating of sample 20-09-SC35; with analyses where $^{208}\text{Pb}/^{204}\text{Pb} < 200$ or $^{232}\text{Th}/^{238}\text{U} < 100$ discounted. U-Pb lower intercept discordia age of 20.96 ± 1.25 Ma shown on left Tera-Wasserburg diagram; IsoplotR U-Th weighted mean age of 22.15 ± 0.71 Ma shown on plot at right. (c) Sample 06-21-SC142: zircon U-Pb concordia youngest population age of 25.57 ± 0.74 Ma plotted on concordia diagram in center, HeFTy pooled zircon fission track age of $26.7 \pm 3.6, -3.2$ Ma shown atop inverse HeFTy (Ketchum, 2005) model results at right.

A sample of the Crestone quartz monzonite (as mapped by Lindsey, 1986) along North Crestone Creek, ~3 km N of the northern margin of the study area, yielded 20 concordant Paleoproterozoic LA-ICP-MS zircon U-Pb dates for a concordia age of 1701.6 ± 9.5 Ma (Fig. 33). ZFT dating of the same sample returned dates of $69.7 +12.3$, -14.8 or 74.6 ± 12.3 Ma, dependent on calculation method (Fig. 33). Between these two methods, cooling to below ~200-260°C (ZFT closure temperature; Reiners & Brandon, 2006) is loosely constrained to pre-Early Eocene, with an aggregate 2σ interval between 54.8 and 86.8 Ma.

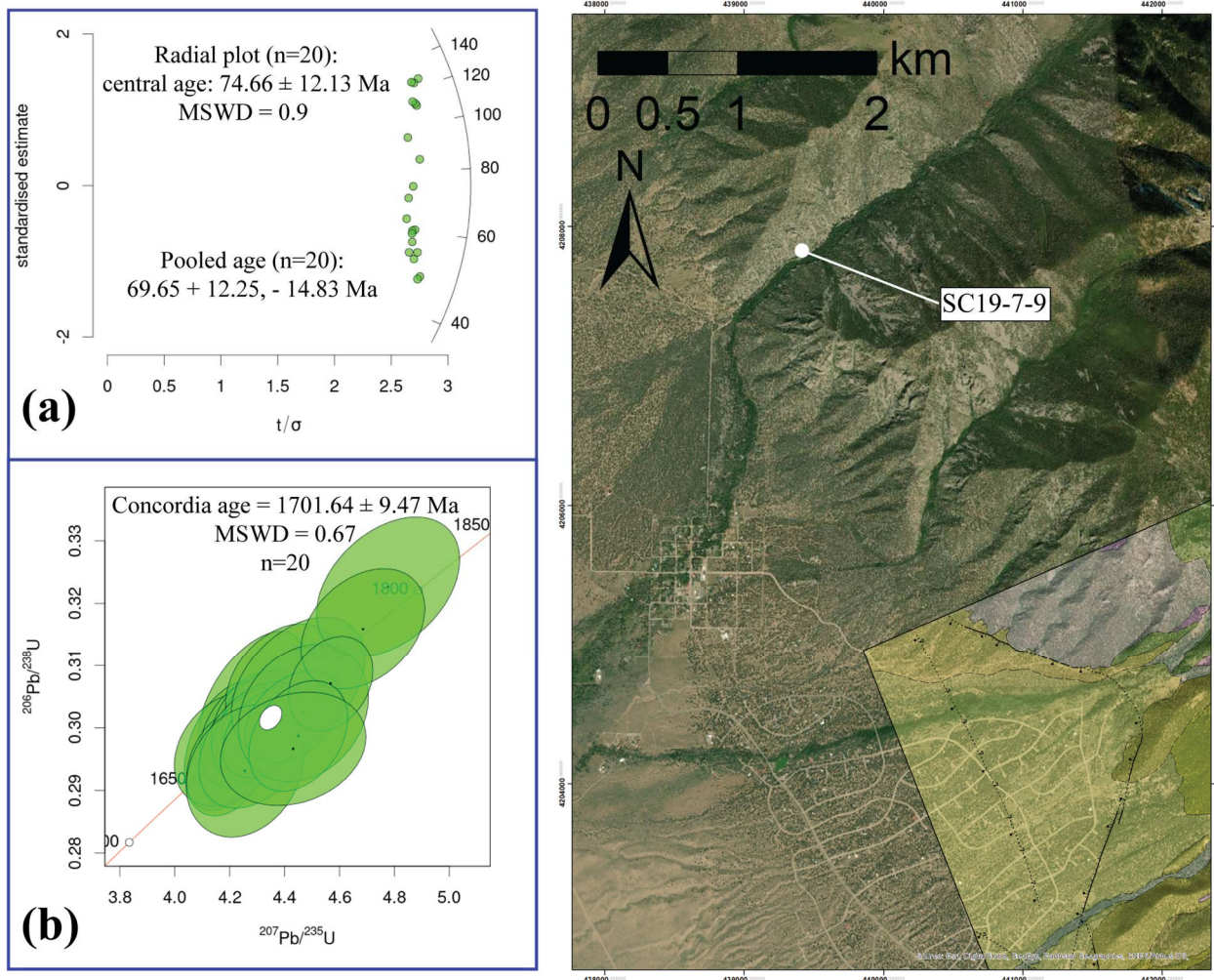


Figure 33. Geochronological analytical results for sample SC19-7-9, with sample location (North Crestone Creek) indicated on the index map at right. (a) Zircon fission track ages; IsoplotR radial plot age (74.7 ± 12.1 Ma) and HeFTy pooled age ($69.7 +12.2$, -14.8 Ma) are shown atop IsoplotR radial plot. (b) Zircon U-Pb dating; concordia age of 1701.7 ± 9.5 Ma plotted atop concordia diagram.

Reflected light petrography and TESCAN mapping of a quartz-feldspar-rich mylonite sample (20-09-SC31) collected from the IMSZ at Spanish Creek, revealed a population of sparse, small ($\leq 50 \mu\text{m}$) monazite grains, mostly along top-SW C shear bands. These grains are interpreted as being essentially metasomatic; they are found in close association with Fe-oxide veinlets. Because the veinlets have an apparently mutually cross-cutting relationship with the sample's top-SW C shear bands, where they (along with associated monazite) are commonly either sheared or completely dissected, they are interpreted as being late-synkinematic to top-SW displacement on the IMSZ. It follows that the monazite grains can also be considered late-synkinematic. LA-ICP-MS U-Th-Pb dating of monazite from this sample yielded dates at 16 spots (Figs. 31, 32A). U-Pb age calculation was done via Terra-Wasserburg discordia (Fig. 32A) due to low Th content (i.e., < 200 ppm for most spots). Three spots were discarded due to anomalously low $^{207}\text{Pb}/^{206}\text{Pb}$; two of these spots were on the same grain and all may have been placed too close to the margins of the target monazites. The remaining analyses produced a calculated age of 24.9 ± 3.0 Ma, though with a high MSWD (5.4) (Fig. 32A). A likewise high $(^{207}\text{Pb}/^{206}\text{Pb})_o$ of ~ 0.754 suggests a possibility of recrystallization inheritance from older monazite (A. Kylander-Clark, personal communication, 2021) and that the actual age of these grain could be younger. Local normal-sense displacement along the IMSZ is thus somewhat tentatively constrained to the latest Oligocene to earliest Miocene.

Sample 09-20-SC35 is of a chlorite-rich mylonite outcrop at the interpreted intersection between the IMSZ and the Sangre de Cristo fault system. Similar to sample 20-09-SC31, monazite in this sample was identified in association with bands of rutile entrained along C and C' shear bands and within sheared Fe-oxide veinlets, and a probable late-synkinematic origin was likewise interpreted. LA-ICP-MS U-Th-Pb of these monazite grains yielded dates from 26

spots (Figs. 31, 32B). Scatter in Tera-Wasserburg space (Fig. 32B) and extremely old calculated ^{232}Th - ^{208}Pb ages for spots with low (i.e., < 200) $^{208}\text{Pb}/^{204}\text{Pb}$ indicated probable common Pb inheritance for this dataset (A. Kylander-Clark, personal communication, 2021). A weighted mean of ^{232}Th - ^{208}Pb dates ($n=13$, after discarding 13 analyses with $^{208}\text{Pb}/^{204}\text{Pb} < 200$ or $^{232}\text{Th}/^{238}\text{U} < 100$) was used to obtain a more ~robust sample age of 22.2 ± 0.7 Ma (Fig. 32B). This age is supplemented by a slightly younger Tera-Wasserburg lower intercept age of 21.0 ± 1.3 Ma (Fig. 32B). Given the sample location for 20-09-SC35 (i.e., at the intersection between the Sangre de Cristo fault, the IMSZ, and at least one other map-scale, chlorite-mylonite-rich shear zone; Sect. 3.2.1), some uncertainty remains as to whether the aforementioned date is directly applicable to the IMSZ. In any case, the 20-09-SC35 monazite U-Th-Pb age constrains latest normal-sense displacement on either the IMSZ, or a sub-parallel brittle-plastic shear zone immediately adjacent, to the earliest Miocene.

LA-ICP-MS U-Pb dating of synkinematic calcite veins was unsuccessful. Though many of 458 spots analyzed contained sufficient ^{238}U for dating, all contained too much common Pb to resolve precipitation ages.

3.6. Whole Rock Geochemistry

Whole-rock geochemical analyses of chloritic mylonites and local gneissic host rock samples (Fig. 35A) paint a complex picture that may be further complicated by small and potentially unrepresentative sample-batches for half the samples analyzed (i.e., Sect. 2.5). Analytical results from one of the samples (20-09-SC5B) that was crushed entirely via sledgehammer were so anomalous (e.g., with Cr content greater than that of any other sample in the study area, by an order of magnitude) that contamination could not be ruled out, and it was eliminated from the dataset entirely. Results from the other samples prepared using this method

(20-09-SC5A, 20-09-SC10, and 19-7-14a-c) are not anomalous but still may not be entirely representative.

Spidergram comparisons (Figs. 35B, 35C) suggest some compositional variance within both gneissic host rocks and chloritic mylonites. Samples 20-09-SC5A and 08-21-SC12F are respectively dominated by quartzo-feldspathic gneiss and gneissic amphibolite, and much of the compositional differences between them (i.e., greater proportions of U, Zr, and Hf in 20-09-SC5A) can be directly attributed to 20-09-SC5A having a more felsic (or potentially pelitic) protolith. Samples 20-09-SC10 and 06-21-SC142 are both of $\text{P}\epsilon\text{g}$, with the former only exposed in a sliver below the IMSZ. These samples are unsurprisingly compositionally similar, with variations between them possibly representing intra-unit compositional variation or artefacts from differing sample sizes (Fig. 35B). The most consistent compositional differences within the chloritic mylonite sample set are between 08-21-SC266 (collected within the brittle-plastic shear zone cutting $\text{P}\epsilon\text{g}$; Fig. 18A) and the other samples. These differences (e.g., lower Zr and Hf in 08-21-SC266) are consistent with 08-21-SC266 being more mafic than other shear zone samples (Rollinson, 2014). The sampled shear zone exposure is necessarily younger (i.e., Oligo-Miocene) and has almost certainly accommodated less total displacement than other shear zones; while finely comminuted material within other shear zones likely represents a mixture of different host rocks, sample 08-21-SC266 is probably mostly made up of (relatively recently) mylonitized $\text{P}\epsilon\text{g}$. Other compositional variation within the chloritic mylonites (e.g., relative Ti-depletion in the 19-7-14 IMSZ samples; Fig. 35A) is more enigmatic and could represent actual inter-shear zone geochemical differences or be an artefact. A non-mylonitic sample (08-21-SC12D) of the metasomatized, ~dm-scale “transition zone” between amphibolitic host rock and a chlorite-rich

mylonitic shear zone appears to be relatively less enriched in most elements but especially refractory ones (e.g., Zr and Ti; Fig 35B).

Composites of host rock geochemical results were used to normalize most mylonitic samples for a final spidergram comparison (Fig. 35C) and as baselines (i.e., “unaltered rock”; (Grant, 2005) in Isocon analyses (Fig. 36). This approach was taken in order to mitigate potential errors stemming from locally unrepresentative samples of the highly variable crystalline basement units in the face of mylonitic homogenization within sampled shear zones. A weighted average of 45% Xqfg (20-09-SC5A), 45% Xga (08-21-SC12F) and 10% P_{eg} (5% each of 20-09-SC10 and 06-21-SC142) was used as a baseline for all chloritic mylonite samples except for 08-21-SC266 and two samples from a single location (08-21-SC12B and 08-21-SC12E). An average of P_{eg} samples was applied for sample 08-21-SC266, and samples 05-21-SC12B and 08-21-SC12F were normalized against a sample (08-21-SC12F) of their relatively fresh, homogenous Xga host rock. The normalized spidergram plot (Fig. 35C) indicates similar relative LREE, HREE, and refractory element enrichment trends (notably nearly identical Eu anomalies) in all chlorite mylonite samples from older shear zones; enrichment-depletion trends are largely mutually inconsistent for other elements. The spidergram trace for sample 08-21-SC266 is fairly flat with the exception of significant but possibly artefactuous apparent Cs depletion. Normalized analytical results for sample 08-21-SC12D are similar to those of 08-21-SC266 up until Gd, where a trend of progressively increasing relative HREE enrichment appears and continues through Lu (Fig. 35B). Given that sample 08-21-SC12D is not mylonitized, hydrothermal HREE enrichment is plausible. However, sample 08-21-SC12D also contains minor tourmaline which appears to predate the metasomatic events being examined, and tourmaline is not found in the

08-21-SC12F petrographic section. Pre-metasomatic compositional differences (possibly including earlier hydrothermal alteration and/or mineralization) also cannot be ruled out.

Isocon diagrams for chlorite mylonite samples from the IMSZ (19-7-14a-14c; Fig. 36A) and from a shear zone that splays from it (05-21-SC12; Figs. A2, 36D) are ambiguous. Interpretations of whether the shear zones underwent significant volume reduction or marginal volume reduction to volume addition depend entirely on which elements are considered to be refractory (Figs. 36A, 36D). If Zr is considered to be refractory, the Isocon analyses suggest volume reduction by a factor of $\leq \sim 0.33$, though the relative degrees of depletion for other elements vary between the two sample localities. This effect disappears entirely, however, when Al is considered to be refractory. Isocon analyses for the Oligo-Miocene, gabbro-hosted chlorite mylonite of sample 08-21-SC266 and for the metasomatized shear-zone-bounding amphibolite of sample 08-21-SC12D suggest little (i.e., with a volume factor of 0.93 to 1.19, again dependent on refractory element selection) volume change. This is unsurprising in the case of the latter sample, which displays significant veining with epidote in thin section. The shear zone cutting Fig (e.g., Figs. 18, 27B, 34) is protomylonitic and completely lacks clinopyroxene and amphibole, but does contain significant (i.e., $\sim 20\%$) proportions of presumably metasomatic

calcite. Locally isovolumetric to marginally dilatational strain is not implausible for this sample.

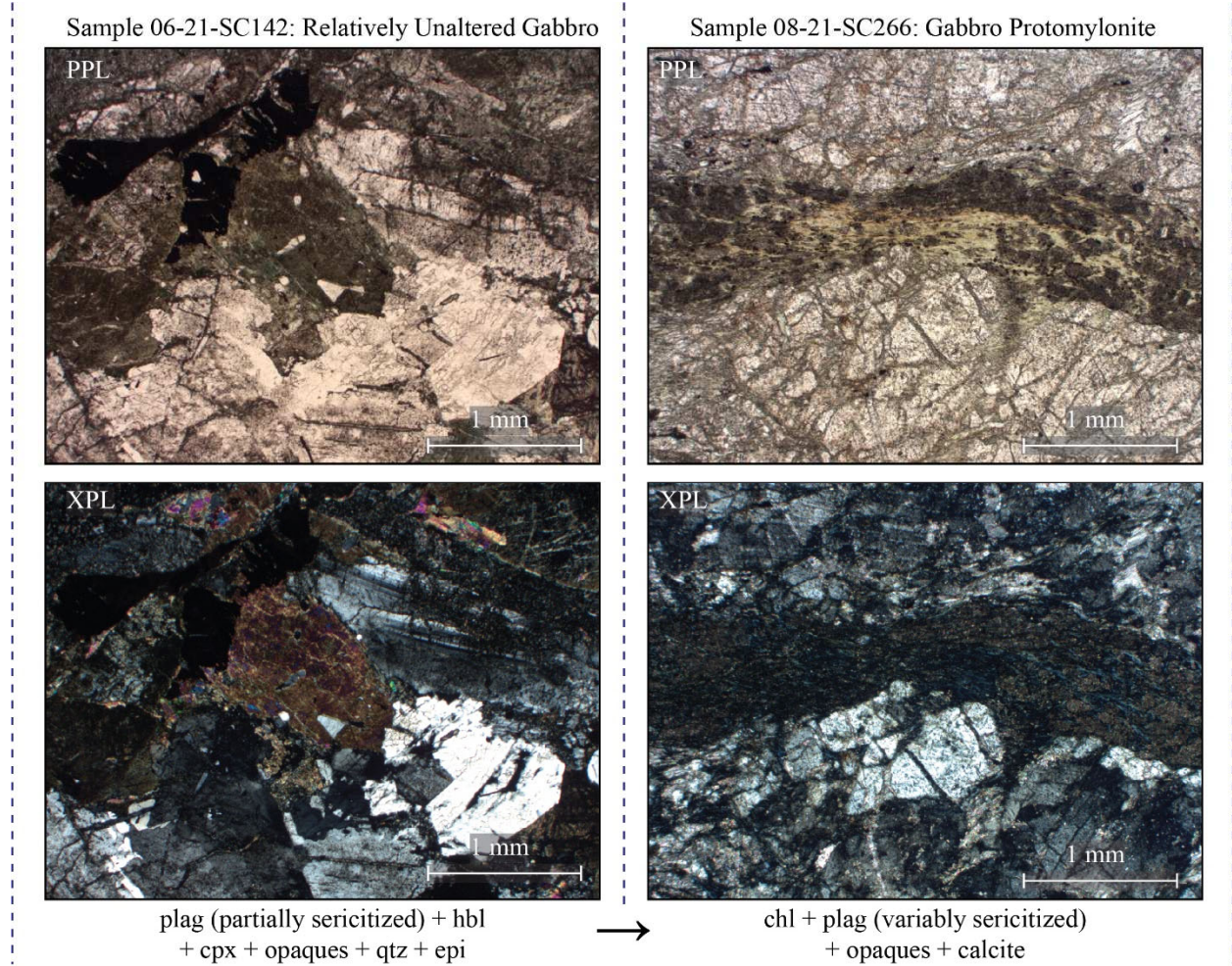


Figure 34. Photomicrographs showing mineralogical and textural differences between sample 06-21-SC142 (relatively unaltered gabbro) and sample 08-21-SC266 (gabbro protomylonite from shear zone shown in Fig. 18; unoriented).

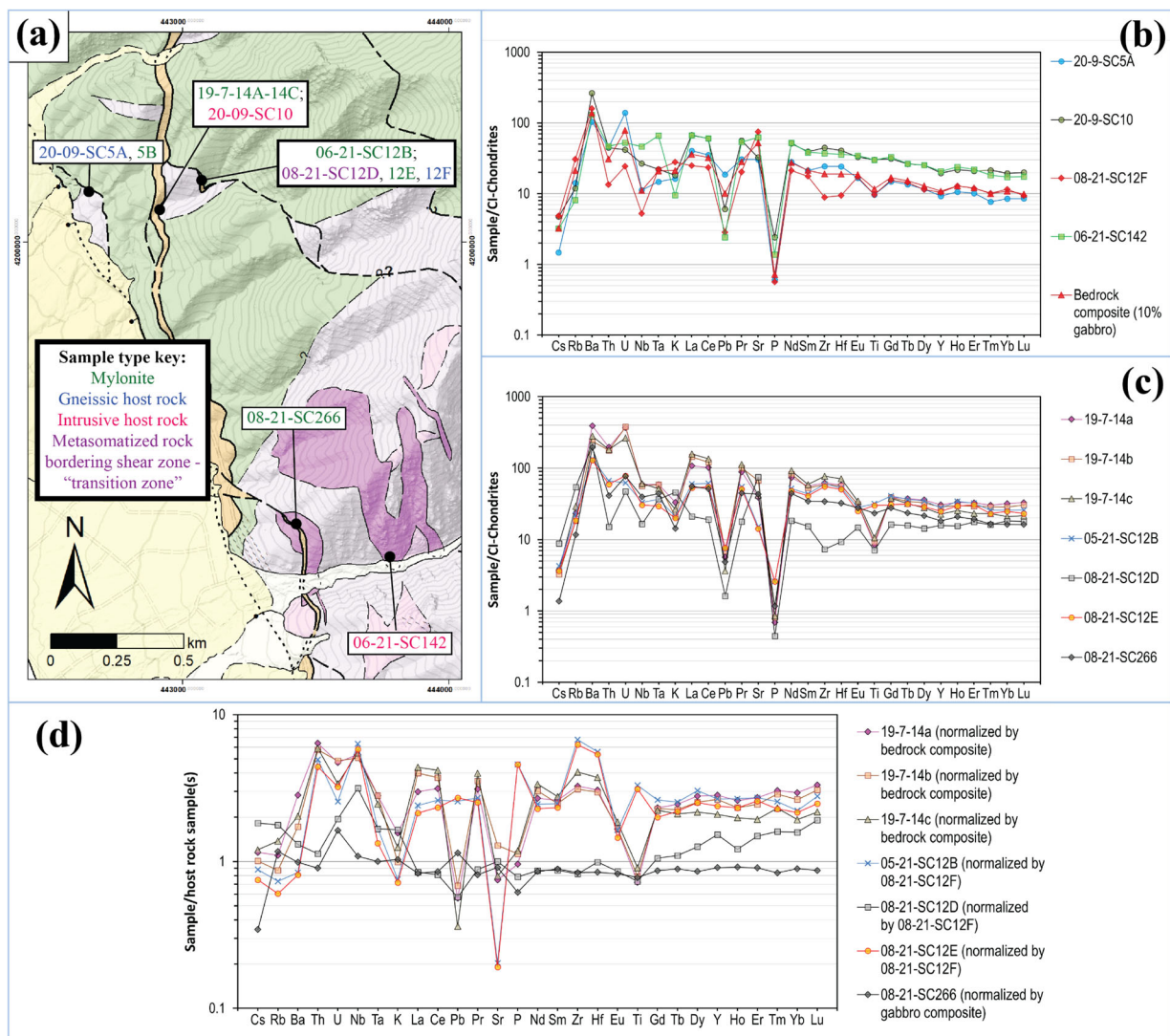


Figure 35. Index map for whole-rock-geochemistry samples and spider diagrams (Stosch, 2022) presenting geochemical analytical results. (a) Index map showing the locations and broad lithology of all samples collected for whole-rock geochemistry in the study area. (b) CI-chondrite-normalized spider diagram plot of gneissic and intrusive shear zone host rock compositions. (c) CI-chondrite-normalized spider diagram plot of geochemically analyzed mylonite samples, plus a single metasomatized non-mylonitic sample. (d) Variably-normalized spider diagram plot of samples shown in c; gneiss-hosted mylonite samples are normalized by an composite bedrock composition (90% gneiss, 10% P_{eg}) for the area, P_{eg} sample by the average composition of P_{eg} samples, and the metasomatized sample by a local amphibolite sample.

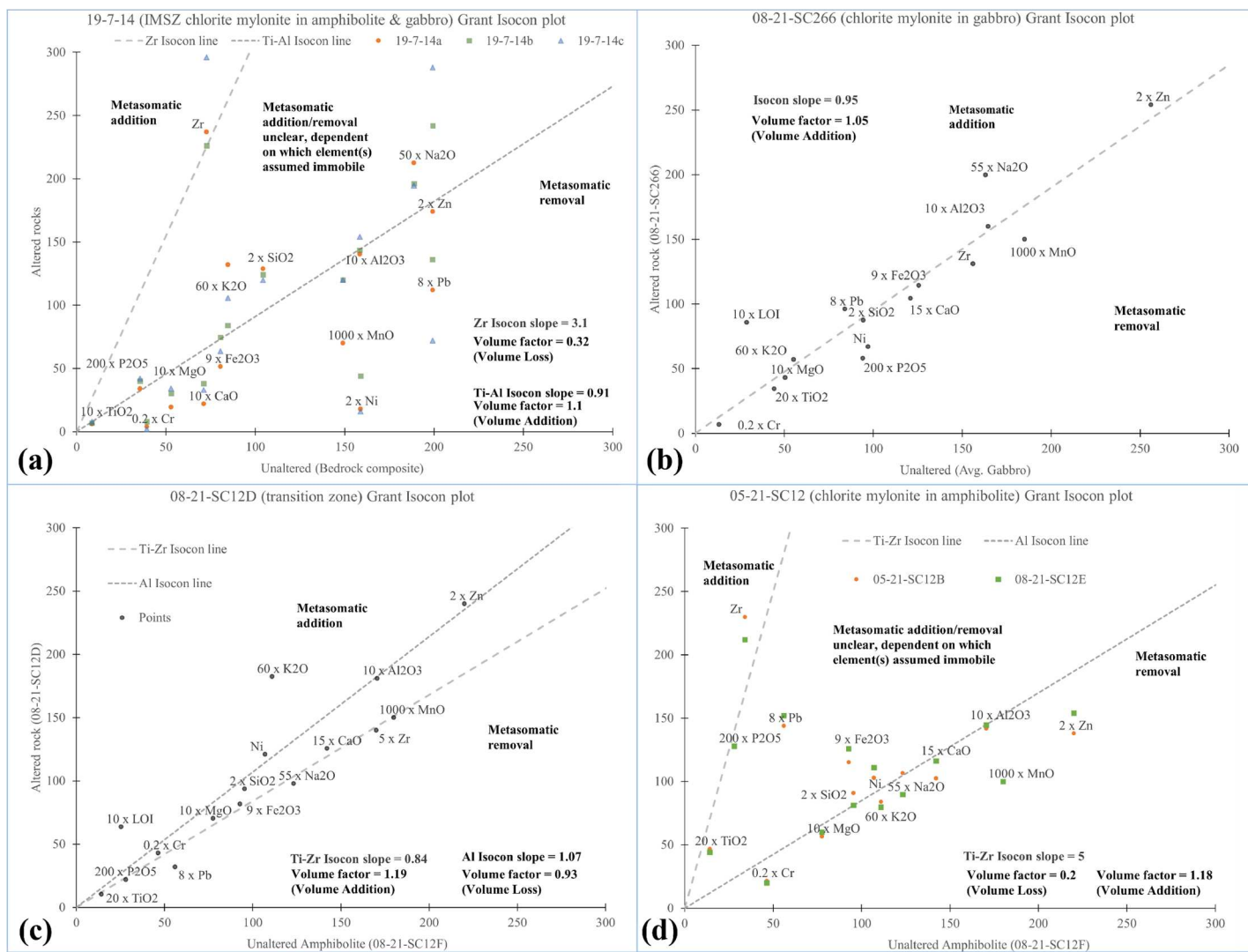


Figure 36. Grant isocon diagrams (i.e., Grant, 2005) comparing the compositions of “unaltered” rock (x-axes) to those of mylonite samples (y-axes). Averaged gneiss and gabbro compositions are used as proxies for “unaltered” rock in the cases of mylonites. Isocon lines are drawn through Ti and Zr where possible, with a preference for Zr where not possible. (a) IMSZ mylonite samples 19-7-14a-c, with weighted-average bedrock baseline. (b) Mylonite sample 08-21-266, with averaged gabbro baseline. (c) Metasomatized amphibolite sample 08-21-SC12D, with local fresh amphibolite baseline. (d) 05-21-SC12B, 12E non-IMSZ mylonites, with weighted-average bedrock baseline.

4. DISCUSSION

4.1. Geologic History

4.1.1. Proterozoic

Compositional foliations in Early Proterozoic gneisses in the study area are dominantly NE-striking, with NW-striking foliation apparently more prevalent above the IMSZ (Fig. 7; Plate 1). Development of the NE-striking foliation is locally constrained to before or possibly during the ~1701 Ma emplacement of the Crestone quartz monzonite, which appears to have intruded along that foliation at the pluton's margins (Fig. 33; Jones & Connelly, 2006). This NE-striking foliation must consequently pre-date the ~1637 Ma development (D₂) of the oldest NE-striking foliation established by Jones & Connelly (2006) for the range as a whole. That local NE-trending fabrics are apparently dominant in the footwalls of the IMSZ and subparallel shear zones but not in superjacent rock suggests that they are relatively localized within the broader basement of the range and San Luis Valley (Jones & Connelly, 2006). Jones & Connelly (2006) speculate that NE-trending fabrics mapped by Johnson et al. (1987) could have been produced via localization of strain associated with NW-directed accretion in the latest phase of the Yavapai orogeny.

Overtured, NE-trending isoclinal folds present in outcrops of Xga and Xqfg throughout the study area (i.e., Fig. 11A) in combination with possible map-scale NE-trending folds (Plate 1) are broadly consistent with the interpretation of coaxial NW-directed shortening in later Paleoproterozoic (D₂; Mazatzal Orogeny) and Mesoproterozoic (D₃) events by Jones & Connelly

(2006). Interpreted map-scale, upright folds were presumably generated through D₃ deformation, but widespread distribution in the mapping area (Plate 1) and apparently to the S (J.S. Caine, personal communication, 2022) is somewhat inconsistent with an interpretation by Jones & Connelly (2006) wherein local NE-SW-trending folds were generated through folding against the Crestone quartz monzonite pluton. D₃ deformation may instead have less localized and been accommodated by large-wavelength folding within a broader area of the north-central Sangre de Cristo Range including the study area.

Oblique foliations apparent in Xga, Xqfg, and Yqm petrographic sections (e.g., Figs. 6A-C) may have formed during D₂ and D₃ events, but their map-scale orientations are unconstrained. Some Proterozoic structural elements, including highly localized, ~NNW-SSE-trending isoclinal folds in the (likely) Mesoproterozoic Yqm (Fig. 11A) are not readily explainable through the known Proterozoic deformation history (i.e., Jones & Connelly, 2006) of the range. A more detailed study focused specifically on the Proterozoic units in the vicinity of Crestone would be required to clearly establish the provenance of these structures and their interrelations.

4.1.2. Paleozoic

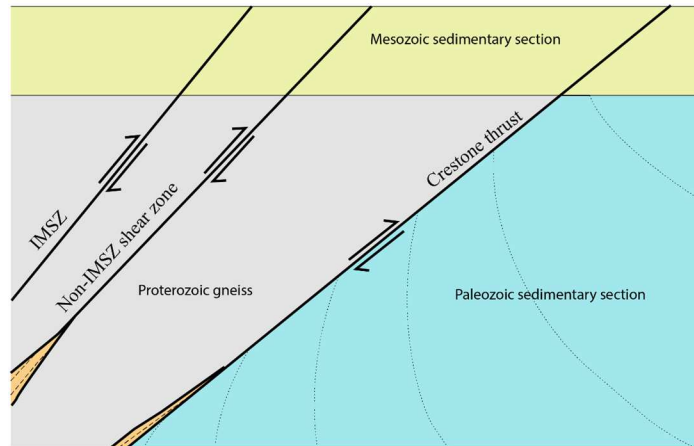
The contacts of Paleozoic units in the study area were refined relative to previous mapping (Plate 1), but other findings with possible implications for local Paleozoic history are scant and somewhat speculative. Some NE-SW-trending joints measured in the Proterozoic basement of the study area could have originated during ARM-related shortening (Fig. 24B). No evidence was found to support or detract from the ARM origin for the Crestone thrust interpreted by Hoy and Ridgway (2002). If this is the case, however, its orientation could have been partially controlled by the NW-striking gneissic fabrics (e.g., Fig 11D) that are found in some parts of the study area and are, per Jones & Connelly (2006), dominant in other parts of the range. These

fabrics are generally sub-vertical but locally dip more shallowly (Jones & Connelly, 2006) and may have promoted the development of similarly striking faults.

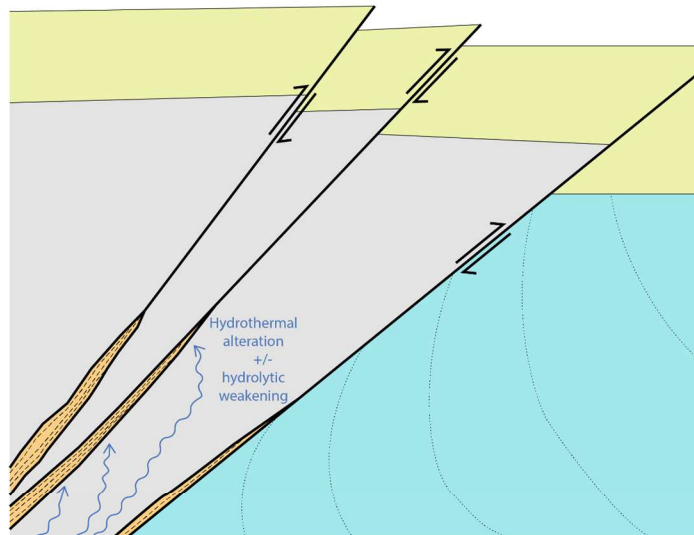
4.1.3. Laramide

One new exposure of the Deadman Creek thrust was identified (Fig. 8). Identification of macro- and micro-structural indicators for potentially mixed top-NE and top-SW kinematics in the exposed Deadman Creek thrust protomylonite-cataclasite zone (Fig. 8B) might indicate a more complex structural history than previously established (i.e., Caine et al., 2013; Weigel, 2014). Map traces and associated contacts for the Laramide Crestone thrust system were refined from previous mapping (Clement, 1952; Johnson et al., 1987; Lindsey, Johnson, et al., 1986), and new mapping generally corroborates relationships noted by prior workers (i.e., that the Crestone thrust localized above the Harding Formation, per Clement (1952)). In contrast with the Deadman Creek thrust, no clear macro- or micro-structural indicators for extensional reactivation of the Crestone thrust system were identified in the map area; an undeformed T1 dike intruding along the Crestone thrust near the N end of the study area (Plate 1) and a similar relationship mapped by Lindsey et al. (1985) farther to the N instead provide strong evidence for a lack of post-Laramide displacement. For lack of additional exposures, no interpretation of the correlativity (i.e., Fig. 5) between the Deadman Creek thrust and other thrust faults to the NE is made in this study.

Early-Laramide: Late Cretaceous(?)



Mid-Laramide: Late Cretaceous to Eocene:



Latest Oligocene to earliest(?) Miocene:

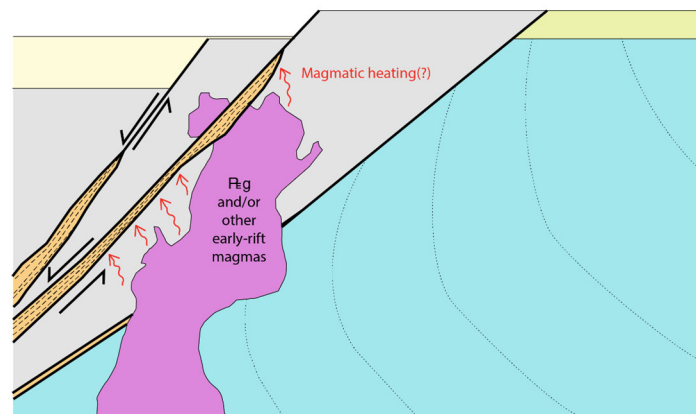


Figure 37. Schematic showing possible evolution of IMSZ, related shear zones during the Late Mesozoic to Miocene.

Detailed mapping of the IMSZ partially expands on the work of prior researchers (e.g., Clement, 1952; Lindsey et al., 1986), and identifies the IMSZ as being the thickest and most laterally extensive member of a system of brittle-plastic shear zones (some previously mapped as faults by Clement, 1952). These shear zones have generally been assumed to record Laramide shortening, though previous studies did not address the timing and kinematics (Clement, 1952; Johnson et al., 1987; Lindsey, Johnson, et al., 1986). Evidence from mapping and microstructural work (i.e., Sects. 3.2, 3.4) broadly supports Laramide origins for these brittle ductile shear zones without precluding or substantiating origins during the ARM orogeny (Fig. 37). Top-NE displacement magnitudes along brittle-plastic shear zones are effectively unconstrained, but decameter-scale zones of mylonite to ultramylonite suggest but do not necessitate that said displacements were significant.

Inconsistent overprinting relations between plastic quartz deformation (e.g., dynamic recrystallization and formation of ribbons) and brittle-cataclastic fracturing is apparent in top-NE shear fabrics from the study area (i.e., Sect. 3.4; Fig. 28), which suggests a spatio-temporally variable relationship between shear zones and the brittle-plastic transition during active top-NE deformation. All brittle-plastic shear zones in the study area are located in Proterozoic rocks in the hanging wall(s) of either the Crestone thrust or other subparallel Laramide thrust faults, and ZFT data indicate that locally these basement rocks had cooled below generally accepted temperatures for quartz dislocation creep (i.e., a bare minimum of $\sim 250^{\circ}\text{C}$ but more commonly closer to 300°C ; Kjøl et al., 2015; Singleton et al., 2020; van Daalen et al., 1999) by the Early Eocene. Greenschist-facies metamorphic assemblages (i.e., hornblende and/or biotite altered to chlorite and plagioclase to white mica, with secondary epidote \pm calcite) preserved in top-NE fabrics suggest localized heating up to $\sim 300^{\circ}\text{C}$ in Pennsylvanian strata during the Laramide.

EBSD data are consistent with deformation near the lower limit of quartz plasticity during top-NE shear ($\sim 300^{\circ}\text{C}$; Fig. 29A), and this will be assumed to approximate the average shear zone deformation temperature during the Laramide. Assuming the $30^{\circ}\text{C}/\text{km}$ Laramide geothermal gradient used by Lindsey et al. (1986), a Laramide depth of ~ 10 km is likely for basement rocks exposed along the western flank of the range.

Given evidence for a brittle precursor to plastic quartz deformation associated with top-NE shear, the IMSZ and related smaller shear zones may have initiated as cataclastic fault zones to accommodate early Laramide shortening at depths above the brittle-plastic transition. They may then have been buried under since-eroded thrust sheets to depths approaching or below the brittle-plastic transition. Greenschist-facies assemblages, shear-involved accessory mineral veinlets, and geochemical analyses (i.e., Sect. 3.6) equivocally suggest concurrent burial-associated heating and contact with fluid (e.g., Fig. 37), and hydrolytic weakening may have helped to facilitate dislocation creep. The $\sim 255^{\circ}\pm 50^{\circ}\text{C}$ temperature suggested for top-NE shear based on the c-axis opening angle for sample 19-7-14 also suggests a role for hydrolytic weakening to facilitate relatively low-temperature dislocation creep. Mylonitic fabrics characterized by plastic deformation of quartz could then have formed concurrent to continued top-NE offset, with advanced lower-greenschist-facies alteration facilitated within shear zones by comminution and fluid channelization. Finally, plastic quartz fabrics could have been locally overprinted by top-NE brittle deformation due to subsequent unroofing, increases in strain rate, a reduction in fluid availability, or some combination thereof.

4.1.4. Cenozoic

This study conclusively dates the dominant local mafic intrusive unit, **Peg**, to the Late Oligocene and classifies it as a tholeiitic gabbro via whole-rock geochemistry (Figs. 32, A.1;

Appendix A). A new ZFT date (26.7 ± 3.6 , -3.2 Ma; Fig. 32C) for the dated stock overlaps with the intrusion's zircon U-Pb date, suggesting the intrusion cooled rapidly to sub-ZFT-closure temperatures following crystallization (e.g., Fig. 37).

Macro- and micro-structural evidence in the study area (e.g., Figs. 15, 16, 26-28) strongly suggests widespread (Fig. 16) extensional reactivation of locally non-Andersonian brittle-plastic shear zones in the study area, but not of the Crestone thrust. Zircon U-Pb dating of the **Fig** intrusion provides a robust latest Oligocene to earliest Miocene (25.6 ± 0.7 Ma; Figs. 14, 32C) upper age constraint for the latest top-SW shearing in one brittle-plastic shear zone in the study area. This age is approximately synchronous with the timing of early Rio Grande rift extension in the vicinity of the Sangre de Cristo Range as interpreted by previous studies (e.g., Wallace, 2004; Ricketts et al., 2016; Sanders et al., 2006).

Though somewhat simplistic (e.g., assuming simple shear), the calculated minimum shear zone displacement estimates (Figs. 23, 24) from this study may provide serviceable basal constraints for normal-sense displacement along the IMSZ and other shear zones. These calculations suggest a sum total of at least ~ 400 – 500 m of normal-sense displacement along the entire stack of brittle-plastic shear zones mapped along the range front.

Age constraints from U-Th-Pb dating of syn-late-kinematic monazite (i.e., 24.91 ± 2.99 Ma from 20-09-SC31, 22.15 ± 0.71 Ma from 20-09-SC35) provide additional insight into timing of normal-sense displacement. All analyses returned have high MSWD values (Figs. 32A-B) but the weighted mean Th-Pb date from 20-09-SC35 (22.15 ± 0.71 Ma; Fig. 33B) is probably more robust given a $^{207}\text{Pb}/^{206}\text{Pb}$ in sample 20-09-SC31 that indicates Pb inheritance (Sect. 3.5). In any case, extensional displacement along the reactivated brittle-plastic shear zones was ongoing during synkinematic monazite development in the Late Oligocene to earliest Miocene, prior to

interpreted timings for an uptick in exhumation rates adjacent to the San Luis Valley as a whole (~14-15 Ma; Miggins et al., 2002; Ghamedi et al., 2023).

The potential uptick in exhumation rates (Lindsey et al., 1986; Miggins et al., 2002) subsequent to the end of top-SW displacement along brittle-plastic shear zones may indicate that extension began to be accommodated along a higher-angle brittle normal fault system (e.g., the Sangre de Cristo fault system and W-dipping normal faults in the San Luis Basin) at this time. Whether Early Miocene Rio Grande rift extension was accommodated by similar, since-obscured reactivated brittle-plastic shear zones in other parts of the range is unclear. Early-rift extension along a chlorite-rich “detachment fault” interpreted by Benson & Jones (1996) to the S of the range and apparent chlorite-rich “breccia” intervals in exploratory boreholes in the San Luis Valley along a structure interpreted by Hoey et al. (2006) as a low-angle, Miocene extensional fault provide limited evidence for more widespread extension along structures similar to the brittle-plastic shear zones found in the study area. Evidence for low-angle extension from Hoey et al. (2006) and Watkins (1996), in particular, is broadly inconsistent with the interpreted subsurface geometry of the Sangre de Cristo fault system established in other studies (Drenth et al., 2019; Kluth & Schaftenaar, 1994; Grauch et al., 2013; Caine et al., 2013), and further investigation through high-resolution seismic transects and potentially through identification and geochronometric analysis of interpreted Mesozoic outcrops could help to rectify these inconsistencies. In any case, an apparent increase in spatial density of brittle-plastic shear zones approaching the present-day Sangre de Cristo fault (Plate 1) and the apparent sub-parallel strike of the Sangre de Cristo fault relative to these shear zones (Fig. 14B; Plate 1) suggests a possibility of structural inheritance.

4.2. Extensional Shear Zone Rheology and Controls on Reactivation

A comparison between interpreted petrographic sample kinematics and local interpreted host shear zone dip suggests that top-SW shear occurred in slip regimes locally ranging from Andersonian to non-Andersonian (Fig. 16C). Reactivation may have been more pervasive in the former class of shear zones, but results are somewhat ambiguous (Fig. 16C). Given that workers (e.g., Benson & Jones, 1996) have proposed significant mineralizing fluid flow along range-bounding faults coeval with early stages Rio Grande rifting and that the IMSZ and other mylonitic shear zones in the field area are rich in phyllosilicates (e.g., Fig. 4B), both high fluid pressure (p_f) and low coefficient of friction μ are viable candidates for enabling the reactivation of the sub-Andersonian shear zones and shear zone segments. Besides p_f , other processes attendant to fluid migration at depth (e.g., hydrolytic and reaction weakening) must be considered as well.

Secondary phyllosilicates (chlorite, white mica, or both) are common constituents of brittle-plastic shear zones samples within the study area (i.e., Fig. 16). The relative proportions of these two different phyllosilicates in a given sample seems to be related to host rock mineralogy; shear zones cutting quartzo-feldspathic gneiss commonly contain more white mica, and shear zones bounded on one or both sides by amphibole-rich host rock (e.g., Xga in the case of the entire IMSZ, Fig. 16) tend to be richer in chlorite. The reaction weakening process by which white mica is generated in a shear zone is locally well preserved in several samples dominated by top-NE kinematic indicators; fractured plagioclase is altered to sericite/white mica by metasomatic (likely hydrothermal) fluids channelized along brittle shear bands, and mica in turn promotes further shear and fluid flow along shear bands (Fig. 11D). Chlorite may be generated from host-rock-derived hornblende

through a similar process, but this process may progress more rapidly. Incipient alteration of hornblende to chlorite is not preserved in any mylonitic samples from the study area, but does appear in the metasomatized ‘transition zone’ sample 08-21-SC12D. Shear zone phyllosilicate mineralogy is likely largely controlled by host rock mineralogy, with relatively chlorite-rich mylonites generated where shear zones cut mafic, hornblende-rich host rock, relatively white-mica-rich mylonites generated where shear zones cut plagioclase-rich rock, and phyllosilicate-deficient mylonites or, more commonly, protomylonites generated where shear zones cut rocks deficient in hornblende and those with relatively less plagioclase.

Alteration of plagioclase to white mica and hornblende to chlorite likely required lower greenschist-facies conditions, and these conditions were probably achieved along most shear zones concurrent to Laramide thrusting (i.e., Fig. 33A; Sect. 4.1.3). ZFT data (i.e., Fig. 32C) suggests temperatures of under ~200-260 °C at North Crestone Creek at the time of top-SW shear zone reactivation. Barring significant variability in burial depths, this would place the shear zones (~8 km to the south) below the accepted limit of ~300°C for greenschist facies metamorphism (Bucher & Grapes, 2011). The chlorite-rich mylonitic fabric of sample 08-21-SC266 (Figs. 27B, 35A), which formed from Late Oligocene P_{eg} host rock, may have developed in the presence hydrothermal fluid sourced either from the gabbroic stock itself or from proximal, co-genetic magmatic bodies. Small intrusive dikes and stocks are common in the study area (e.g., P_{eg} , Tad, Td, Tr; Plate 1), and hydrothermal mineralization along rift-related structures is well attested to both by syn-late-kinematic calcite and Fe-oxide veins within study area shear zone samples (e.g., Fig. 27B) and by a broad zone of (generally) subeconomic mineralization following the Sangre de Cristo fault system, identified by (Johnson et al., 1984). Localized Late Oligocene heating via hydrothermal fluids, or through locally magmatically

elevated geothermal gradients may help to explain how top-SW extensional shear likely occurred at temperatures $\geq 300^{\circ}\text{C}$, whereas crystalline rocks farther N cooled below $\sim 250^{\circ}\text{C}$ during Laramide time (e.g., Figs. 27B, E-F; Fig. 37).

Geochemical analyses (Figs. 35, 36) provide some evidence for the role that hydrothermal fluid may have played in the brittle-plastic shear zones. Shear zone samples likely representing a combination of top-NE and top-SW displacement (i.e., from the IMSZ or splaying from it; Figs. 35, 36) have self-similar spidergram trends (Fig. 35D) that record significant volume loss on Isocon diagrams (Figs. 36A, 36D; consistent with findings of volume loss during reaction weakening and development of phyllonites (O'Hara, 1988, 1990)). In contrast, sample 08-21-SC266 has a relatively flat spidergram trace when normalized by its Late Oligocene gabbroic host rock (Fig. 35B), and plots consistently with mild volume addition (volume factor of 1.16) on an Isocon diagram (Fig. 36B). The relations among these samples suggest that the majority of geochemical-volumetric change in shear zones rocks within the study area was associated with pre-Oligocene displacement, with said changes likely dominated by volume reduction. A sample of metasomatized amphibolite immediately adjacent to a top-SW chlorite mylonite zone (08-21-SC12D; normalized by adjacent fresh amphibolitic gneiss) exhibits a similar Isocon-derived volume factor (1.18; Fig. 36C) to that of sample 08-21-SC266. It also, however, displays a trend of relative HREE addition (Fig. 35D) shared to some degree by mylonite samples from the IMSZ and its splay. Possible HREE addition is also indicated in samples of ~~Fig~~ host rock itself (Fig. A1C), but not in 08-21-SC266 (Figs. 35D, 36B). The implications of apparent HREE enrichment for fluid geochemistry are enigmatic. Cl^- is the most common ligand involved in hydrothermal REE mobilization, and REE- Cl^- -complexation in hydrothermal systems is expected to result in either HREE enrichment at the expense of LREEs or LREE enrichment without HREE

enrichment, depending on temperature, but not HREE enrichment without LREE enrichment (Williams-Jones et al., 2012). Regardless, if HREE enrichment is taken as a signature for hydrothermal alteration in the study area, the relative lack of HREE enrichment in sample 08-21-SC266 could indicate relatively less syn-kinematic exposure to hydrothermal fluids. Thus, geochemical evidence somewhat equivocally suggests relatively less fluid involvement along shear zones during active top-SW displacement than during active top-NE displacement.

Petrographic sections (e.g., Figs. 26, 27) indicate that top-SW fabrics formed in zones dominantly composed of phyllosilicate or along phyllosilicate-lined structures surrounded by stronger minerals (Figs. 27A, 27B, 27A, 27D), sometimes with cataclastic fracturing of dynamically recrystallized quartz (Fig. 27F). Compiled estimates of microstructural kinematics and modal phyllosilicate (i.e., chlorite and white mica) proportions suggest that samples preserving exclusively top-NE kinematic indicators are disproportionately mica-poor (Fig. 16). Samples with pervasive overprinting by top-SW kinematic indicators are likewise generally richer in phyllosilicates (Fig. 16). In petrographic sections containing mixtures of top-NE and top-SW kinematic indicators, top-SW fabrics are often more localized and concentrated in intervals where phyllosilicates form the interconnected weak phase (e.g., Fig. 27D), and this relationship seems to hold both within the microstructural dataset and on a macro- and map-scale (Figs. 15, 16, 14). A lack of top-SW-consistent quartz asymmetry fabrics in the two samples successfully analyzed via EBSD also suggests that top-SW quartz dislocation creep was limited, at least relative to during top-NE deformation. Extensional deformation was consequently likely accommodated mostly through grain-boundary sliding and slip on basal mica planes in micaceous domains of reactivated shear zones, with the presence of interconnected phyllosilicates partially controlling whether shear zones were reactivated or not (i.e., Fig. 16).

Most shear zones identified in the study area (Fig. 16A) preserve some evidence for top-SW reactivation. Reactivation appears to have been pervasive in some shear zones (e.g., with top-SW fabrics observed in almost every outcrop of the IMSZ), but in others may have localized to thinner, mostly phyllosilicate-rich intervals (Fig. 16; Plate 1). Overall, brittle to brittle-plastic reactivation of the shear zones seems to have been controlled by the mineralogy of their constituent interconnected weak phases such that phyllosilicate-rich shear zones were disproportionately reactivated. Intra-shear zone phyllosilicate contents were in turn likely controlled by reaction weakening in conjunction with hydrolytic weakening, with the magnitude of weakening varying dependent on host rock petrology. Though Pennsylvanian strata in the footwall of the Crestone thrust system within the study area are locally mica-rich, these sedimentary units are heterogenous and may not have been weak enough on net to allow reactivation. Additionally, the Crestone thrust could have been effectively kinematically ‘locked’ by late(?) Laramide folding, as would be expected in interpretations where it is contiguous with the Deadman Creek thrust fault (e.g., Fig. 5).

5. CONCLUSIONS

This study presents results from geologic mapping in conjunction with microstructural, geochemical, geochronological, and thermochronological analyses in a 50 km² study area along the western flank of the Sangre de Cristo Range, with a focus on the brittle-plastic IMSZ near Crestone, Colorado. Key findings include the IMSZ as the thickest and most laterally extensive member of a system of SW-dipping brittle-plastic shear zone and that many of these shear zones show extensive micro- and macro-structural evidence for extensional (top-SW) overprinting of originally reverse-sense (top-NE), brittle-plastic deformational fabrics. These shear zones are likely of Laramide origin, and normal-sense overprinting is associated with early stages of extension in the Rio Grande rift.

Inconsistent microstructural relationships between preserved brittle and plastic fabrics associated with top-NE (probable) Laramide displacement suggest a complicated spatio-temporal relationship with the brittle-plastic transition. The shear zones may have originated as cataclastic fault zones during early Laramide deformation. Mylonitic fabrics characterized by quartz dislocation creep and dynamic recrystallization formed through a combination of overthrusting burial and, probably, hydrolytic weakening. Also at this time, reaction weakening through alteration of comminuted host rock plagioclase and hornblende produced domains where phyllosilicate (white mica and chlorite) forms an interconnected weak phase in many shear zones. Brittle fracturing of plastic fabrics, consistent with top-NE Laramide kinematics, suggests that some of the shear zones ceased to deform plastically while still accommodating Laramide shortening.

Extensional reactivation is constrained to the latest Oligocene-earliest Miocene by a 25.6 ± 0.7 Ma zircon U-Pb age for a tholeiitic gabbro stock cut by one of the non-IMSZ shear zones identified. Variable U-Pb and Th-Pb dates of apparent late-synkinematic monazite constrain the end of extensional displacement along the reactivated shear zones to the Early Miocene. A ZFT age of $26.7 + 3.6, -3.2$ Ma from the gabbroic stock suggests that shearing was locally short lived and may have occurred during magmatic cooling.

Extensional fabrics are characterized by S-C-C' fabrics in micaceous domains and by C' shear bands lined by phyllosilicates, with extensional shear bands locally fracturing inferred Laramide dynamically recrystallized quartz bands. Top-SW deformation was probably accommodated primarily through grain boundary sliding and basal slip along mica planes, locally in addition to quartz dislocation creep. Extensional overprinting is concentrated in micro-, macro- and map-scale domains where phyllosilicates form an interconnected weak phase, with contractional fabrics better preserved where quartz or feldspars form the interconnected phase. Whether shear zones were reactivated or not was consequently likely governed by host rock mineralogy, by way of inferred Laramide reaction weakening.

The apparent end of extensional displacement along the reactivated shear zones predated or roughly coincided with an uptick in local extension rates. Displacement may have moved to the sub-parallel range-bounding Sangre de Cristo fault system at this time. Reactivation of Laramide structures may have been a more widespread process by which mid-crustal extension was accommodated during the earliest stages of Rio Grande rifting.

REFERENCES

- Abbey, A. L., & Niemi, N. A. (2018). Low-temperature thermochronometric constraints on fault initiation and growth in the northern Rio Grande rift, upper Arkansas River valley, Colorado, USA. *Geology*, *46*(7), 627–630. <https://doi.org/10.1130/G40232.1>
- Abbey, A. L., & Niemi, N. A. (2020). Perspectives on Continental Rifting Processes From Spatiotemporal Patterns of Faulting and Magmatism in the Rio Grande Rift, USA. *Tectonics*, *39*(1), e2019TC005635. <https://doi.org/10.1029/2019TC005635>
- Allmendinger, R. W. (2015). *Modern Structural Practice* (v. 1.7.0).
- Allmendinger, R. W., Cardozo, N., & Fisher, D. M. (2013). STRUCTURAL GEOLOGY ALGORITHMS: VECTORS AND TENSORS. *American Mineralogist*, *98*(10), 1915–1915. <https://doi.org/10.2138/am.2013.607>
- Allmendinger, R. W., Siron, C. R., & Scott, C. P. (2017). Structural data collection with mobile devices: Accuracy, redundancy, and best practices. *Journal of Structural Geology*, *102*, 98–112. <https://doi.org/10.1016/j.jsg.2017.07.011>
- Anderson, E. M. (1905). The dynamics of faulting. *Transactions of the Edinburgh Geological Society*, *8*(3), 387. <https://doi.org/10.1144/transed.8.3.387>
- Baldrige, A. M., Hook, S. J., Grove, C. I., & Rivera, G. (2009). The ASTER spectral library version 2.0. *Remote Sensing of Environment*, *113*(4), 711–715. <https://doi.org/10.1016/j.rse.2008.11.007>
- Barth, N. C., Hacker, B. R., Seward, G. G. E., Walsh, E. O., Young, D., & Johnston, S. (2010). Strain within the ultrahigh-pressure Western Gneiss region of Norway recorded by quartz

CPOs. *Geological Society, London, Special Publications*, 335(1), 663–685.

<https://doi.org/10.1144/SP335.27>

Behr, W. M., & Platt, J. P. (2014). Brittle faults are weak, yet the ductile middle crust is strong: Implications for lithospheric mechanics. *Geophysical Research Letters*, 41(22), 8067–8075. <https://doi.org/10.1002/2014GL061349>

Benson, R. G., & Jones, D. M. (1996). Geology of the San Luis gold deposit, Costilla County, Colorado: An example of low-angle normal fault and rift-related mineralization in the Sangre de Cristo Range of Colorado. In *Geologic Excursions to the Rocky Mountains and Beyond*. Colorado Geological Survey.

<https://catalog.aspencaat.info/GroupedWork/3e5319a8-b526-220b-5410-5197f00dc5b4>

Bickford, M. E., Shuster, R. D., & Boardman, S. J. (1989). U-Pb geochronology of the Proterozoic volcano-plutonic terrane in the Gunnison and Salida areas, Colorado. In J. A. Grambling & B. J. Tewksbury (Eds.), *Proterozoic Geology of the Southern Rocky Mountains* (Vol. 235, p. 33-48). Geological Society of America.

<https://doi.org/10.1130/SPE235-p33>

Brace, W. F. and Kohlstedt, D. L.: Limits on lithospheric stress imposed by laboratory experiments, *Journal of Geophysical Research: Solid Earth*, 85, 6248–6252,

<https://doi.org/10.1029/JB085iB11p06248>, 1980.

Brister, B. S., & Gries, R. R. (1994). Tertiary stratigraphy and tectonic development of the Alamosa basin (northern San Luis Basin), Rio Grande rift, south-central Colorado. In G. R. Keller & S. M. Cather (Eds.), *Basins of the Rio Grande Rift: Structure, Stratigraphy, and Tectonic Setting* (Vol. 291, p. 39-58). Geological Society of America.

<https://doi.org/10.1130/SPE291-p39>

- Bucher, K., & Grapes, R. H. (2011). *Petrogenesis of metamorphic rocks* (8th ed). Springer.
- Bush, M. A., Horton, B. K., Murphy, M. A., & Stockli, D. F. (2016). Detrital record of initial basement exhumation along the Laramide deformation front, southern Rocky Mountains. *Tectonics*, 35(9), 2117–2130. <https://doi.org/10.1002/2016TC004194>
- Byerlee, J. (1978). Friction of rocks. *Pure and Applied Geophysics*, 116(4), 615–626. <https://doi.org/10.1007/BF00876528>
- Caine, J. S., Giles, S. A., & Spence, K. N. (2021). *Digital Data from Mineral Investigation of Sangre de Cristo Wilderness Study Area, Alamosa, Custer, Fremont, Huerfano, and Saguache Counties, Colorado, USA* [Data set]. U.S. Geological Survey. <https://doi.org/10.5066/P98D3WXM>
- Caine, J. S., Grauch, V. J. S., & Lindsey, D. A. (2013). Tales of the Deadman Thrust: Northeast verging folds, injection breccias, and high-angle normal faults in the rift-flanking basement of the Sangre de Cristo mountains, Colorado. *Geological Society of America Abstracts with Programs*, 45(7), 443.
- Caine, J. S., Minor, S. A., Grauch, V. J. S., Budahn, J. R., & Keren, T. T. (2017). A comprehensive survey of faults, breccias, and fractures in and flanking the eastern Española Basin, Rio Grande rift, New Mexico. *Geosphere*, 13(5), 1566–1609. <https://doi.org/10.1130/GES01348.1>
- Carpenter, B. M., Saffer, D. M., & Marone, C. (2012). Frictional properties and sliding stability of the San Andreas fault from deep drill core. *Geology*, 40(8), 759–762. <https://doi.org/10.1130/G33007.1>
- Cather, S. (2004). Laramide orogeny in central and northern New Mexico and southern Colorado. *The Geology of New Mexico: A Geologic History*, 11, 203–248.

- Clement, J. F. (1952). *The Geology of the Northeastern Baca Grant Area, Saguache County, Colorado* [M.S. Thesis]. Colorado School of Mines.
- Collettini, C. (2011). The mechanical paradox of low-angle normal faults: Current understanding and open questions. *Tectonophysics*, 510(3–4), 253–268.
<https://doi.org/10.1016/j.tecto.2011.07.015>
- Shaw v. Kellogg, No. 170 (1898). <https://openjurist.org/170/us/312/shaw-v-kellogg>
- Drenth, B. J., Grauch, V. J., & Rodriguez, B. D. (2019). Geophysical constraints on Rio Grande rift structure in the central San Luis Basin, Colorado and New Mexico. *GSA Special Papers*, 494, 75–99. USGS Publications Warehouse.
[https://doi.org/10.1130/2013.2494\(04\)](https://doi.org/10.1130/2013.2494(04))
- Ellis, C. E., Hannigan, B. J., & Thompson, J. R. (1983). *Mineral investigation of the Sangre de Cristo Wilderness Study Area, Alamosa, Custer, Fremont, Huerfano, and Saguache Counties, Colorado* (No. 65–83; U.S. Bureau of Mines Open-File Report MLA, p. 190).
- EnMAP-Box Developers. (2019). *EnMAP-Box 3—A QGIS Plugin to process and visualize hyperspectral remote sensing data*. <https://enmap-box.readthedocs.io>
- Faleiros, F.M., Moraes, R.D., Pavan, M., Campanha, G.A.D.C., 2016. A new empirical calibration of the quartz c-axis fabric opening-angle deformation thermometer. *Tectonophysics* 671, 173–182.
- Fauntleroy, G. (2013, July 29). Land, water, grass & animals: History of the Baca Grant, part I. *Crestone Eagle*. <https://crestoneeagle.com/land-water-grass-animals-history-of-the-baca-grant-part-i/>
- Fletcher, J. M., Coogan, J., Benson, C. W., Csar, A. J., Gullet, C. J., Oliver, S. R., & Teran, O. J. (2006, May 19). *ROLE OF TECTONIC INHERITANCE AND MODE OF*

CONTINENTAL EXTENSION IN THE UPPER RIO GRANDE RIFT. Rocky Mountain Section—58th Annual Meeting.

<https://gsa.confex.com/gsa/2006RM/webprogram/Paper104884.html>

Ghamed, O., Singleton, J., Sitar, M. C., Rahl, J., Wong, M., O’Sullivan, P., Hurtado, C., & Malavarca, S. (2023, May 23). Refining the pre- and syn-Rio Grande rift cooling history across the Sangre de Cristo Range and Alvarado fault through application of mid- to low-temperature thermochronometry. Geological Society of America 2023 Rocky Mountain Section Meeting, Fort Collins, Colorado, USA. <https://doi.org/10.1130/abs/2023RM-387970>

Gilmer, A., Thompson, R., Turner, K. J., & Morgan, L. (2022). *EXTENSION-RELATED VOLCANISM ALONG THE MARGIN OF THE NORTHERN RIO GRANDE RIFT IN SOUTHERN COLORADO AND NORTHERN NEW MEXICO, USA*. 374038.

<https://doi.org/10.1130/abs/2022CD-374038>

Grant, J. A. (2005). Isocon analysis: A brief review of the method and applications. *Physics and Chemistry of the Earth, Parts A/B/C*, 30(17), 997–1004.

<https://doi.org/10.1016/j.pce.2004.11.003>

Grauch, V. J., Bedrosian, P. A., & Drenth, B. J. (2013). Advancements in understanding the aeromagnetic expressions of basin-margin faults—An example from San Luis Basin, Colorado. *The Leading Edge*, 32(8), 882–891. USGS Publications Warehouse.

<https://doi.org/10.1190/tle32080882.1>

Griggs, D. (1967). Hydrolytic Weakening of Quartz and Other Silicates*. *Geophysical Journal International*, 14(1–4), 19–31. <https://doi.org/10.1111/j.1365-246X.1967.tb06218.x>

- Hayden, F. V. (1877). *Geological and geographical atlas of Colorado and portions of adjacent territory* [Map]. U.S. Geological and Geographical Survey of the Territories (Hayden).
- Hoey, N., Watkins, T. A., & Parsons, K. (2006). *A SUMMARY REVIEW INCLUDING A WORK PLAN AND BUDGET PROPOSAL TO TEST OIL AND GAS PROSPECTS ON THE SAN LUIS BASIN PROPERTY, COLORADO, USA FOR LEXAM EXPLORATIONS INC.* Watts, Griffis and McOuat Limited.
- Holm-Denoma, C. S., Caine, J. S., & Pianowski, L. S. (2019). *U-Pb zircon data for: The Poncha Pass and Deadman Creek areas, northern Sangre de Cristo mountains of south-central Colorado* [Data set]. U.S. Geological Survey. <https://doi.org/10.5066/P96HNSNL>
- Horstwood, M. S. A., Košler, J., Gehrels, G., Jackson, S. E., McLean, N. M., Paton, C., Pearson, N. J., Sircombe, K., Sylvester, P., Vermeesch, P., Bowring, J. F., Condon, D. J., & Schoene, B. (2016). Community-Derived Standards for LA-ICP-MS U-(Th-)Pb Geochronology – Uncertainty Propagation, Age Interpretation and Data Reporting. *Geostandards and Geoanalytical Research*, 40(3), 311–332. <https://doi.org/10.1111/j.1751-908X.2016.00379.x>
- Hoy, R. G., & Ridgway, K. D. (2002). Syndepositional thrust-related deformation and sedimentation in an Ancestral Rocky Mountains basin, Central Colorado trough, Colorado, USA. *GSA Bulletin*, 114(7), 804–828. [https://doi.org/10.1130/0016-7606\(2002\)114<0804:STRDAS>2.0.CO;2](https://doi.org/10.1130/0016-7606(2002)114<0804:STRDAS>2.0.CO;2)
- Iacovino, Kayla, & Asimow, Paul. (2018). *Plutonic TAS Diagram Plotter* (1.0). Zenodo. <https://doi.org/10.5281/ZENODO.5907892>
- Johnson, B. R., Lindsey, D. A., Bruce, R. M., & Soulliere, S. J. (1987). Reconnaissance geologic map of the Sangre de Cristo Wilderness Study Area, south-central Colorado. In

- Miscellaneous Field Studies Map* (No. 1635-B). U.S. Geological Survey.
<https://doi.org/10.3133/mf1635B>
- Johnson, B. R., Lindsey, D. A., Ellis, C. E., Hannigan, B. J., & Thompson, J. R. (1984). *Mineral resource potential of the Sangre de Cristo Wilderness study area, south-central Colorado* (Report No. 1635A; Miscellaneous Field Studies Map). USGS Publications Warehouse.
<https://doi.org/10.3133/mf1635A>
- Jones, J. V., III, & Connelly, J. N. (2006). Proterozoic tectonic evolution of the Sangre de Cristo Mountains, southern Colorado, U.S.A. *Rocky Mountain Geology*, 41(2), 79–116.
<https://doi.org/10.2113/gsrocky.41.2.79>
- Kelley, S. A., Chapin, C. E., & Corrigan, J. (1992). *Late Mesozoic to Cenozoic cooling histories of the flanks of the northern and central Rio Grande rift, Colorado and New Mexico* (Vol. 145). New Mexico Bureau of Mines & Mineral Resources.
- Ketcham, R. A.: Forward and Inverse Modeling of Low-Temperature Thermochronometry Data, *Reviews in Mineralogy and Geochemistry*, 58, 275–314,
<https://doi.org/10.2138/rmg.2005.58.11>, 2005.
- Kington, J. (2020). *Mplstereonet* [Python]. <https://github.com/joferkington/mplstereonet>
(Original work published 2012)
- Kjøll, H. J., Viola, G., Menegon, L., & Sørensen, B. E. (2015). Brittle–viscous deformation of vein quartz under fluid-rich lower greenschist facies conditions. *Solid Earth*, 6(2), 681–699. <https://doi.org/10.5194/se-6-681-2015>
- Kluth, C. F., & Schaftenaar, C. H. (1994). *Depth and geometry of the northern Rio Grande rift in the San Luis Basin, south-central Colorado*. <https://doi.org/10.1130/SPE291-p27>

- Kokaly, R. F., Clark, R. N., Swayze, G. A., Livo, K. E., Hoefen, T. M., Pearson, N. C., Wise, R. A., Benzel, W. M., Lowers, H. A., Driscoll, R. L., & Klein, A. J. (2017). *USGS Spectral Library Version 7* (Report No. 1035; Data Series, p. 68). USGS Publications Warehouse. <https://doi.org/10.3133/ds1035>
- Leonard, E. M., Laabs, B. J. C., Plummer, M. A., Kroner, R. K., Brugger, K. A., Spiess, V. M., Refsnider, K. A., Xia, Y., & Caffee, M. W. (2017). Late Pleistocene glaciation and deglaciation in the Crestone Peaks area, Colorado Sangre de Cristo Mountains, USA – chronology and paleoclimate. *Quaternary Science Reviews*, *158*, 127–144. <https://doi.org/10.1016/j.quascirev.2016.11.024>
- Lindsay, J. (2014). The Whitebox Geospatial Analysis Tools project and open-access GIS. *Proceedings of the GIS Research UK 22nd Annual Conference*, 16–18.
- Lindsey, D. A. (1998). Laramide structure of the central Sangre de Cristo Mountains and adjacent Raton Basin, southern Colorado. *Mountain Geologist*, *35*(2), 55–70. USGS Publications Warehouse.
- Lindsey, D. A. (2010). The Geologic Story of Colorado's Sangre de Cristo Range. *US Geological Survey Circular*, 1–18.
- Lindsey, D. A., Andriessen, P. a. M., & Wardlaw, B. R. (1986). Heating, cooling, and uplift during Tertiary time, northern Sangre de Cristo Range, Colorado. *GSA Bulletin*, *97*(9), 1133–1143. [https://doi.org/10.1130/0016-7606\(1986\)97<1133:HCAUDT>2.0.CO;2](https://doi.org/10.1130/0016-7606(1986)97<1133:HCAUDT>2.0.CO;2)
- Lindsey, D. A., Clark, R. F., & Soulliere, S. J. (1985). Reference section for the Minturn Formation (Middle Pennsylvanian), northern Sangre de Cristo Range, Custer County, Colorado. In *Reference section for the Minturn Formation (Middle Pennsylvanian), northern Sangre de Cristo Range, Custer County, Colorado* (USGS Numbered Series No.

- 1622–C; Miscellaneous Field Studies Map, Vols. 1622–C). U.S. Geological Survey.
<https://doi.org/10.3133/mf1622C>
- Lindsey, D. A., Clark, R. F., & Soulliere, S. J. (1986). Minturn and Sangre de Cristo Formations of Southern Colorado: A Prograding Fan Delta and Alluvial Fan Sequence Shed from the Ancestral Rocky Mountains. In J. A. Peterson (Ed.), *Paleotectonics and sedimentation in the Rocky Mountain Region, United States* (Vol. 41, p. 0). American Association of Petroleum Geologists. <https://doi.org/10.1306/M41456C26>
- Lindsey, D. A., Johnson, B. R., & Andriessen, P. a. M. (1984). Laramide and Neogene Structure of Northern Sangre de Cristo Range, South-Central Colorado. *AAPG Bulletin*, 68(7), 941–941. <https://doi.org/10.1306/AD461548-16F7-11D7-8645000102C1865D>
- Lindsey, D. A., Johnson, B. R., Soulliere, S. J., Bruce, R. M., & Hafner, K. (1986). *Geologic map of the Beck Mountain, Crestone Peak, and Crestone quadrangles, Custer, Huerfano, and Saguache counties, Colorado* (Report No. 1878; Miscellaneous Field Studies Map). USGS Publications Warehouse. <https://doi.org/10.3133/mf1878>
- Lindsey, D. A., Scott, G. R., Soulliere, S. J., & De Angelis, B. L. (1984). *Geologic map of the Horn Peak Quadrangle, Custer and Saguache counties, Colorado* (Report No. 1623; Miscellaneous Field Studies Map). USGS Publications Warehouse.
<https://doi.org/10.3133/mf1623>
- Lindsey, D. A., Soulliere, S. J., Hafner, K., & Flores, R. J. (1985). *Geologic map of Rito Alto Peak and northeastern part of Mirage quadrangles, Custer and Saguache counties, Colorado* (Report No. 1787; Miscellaneous Field Studies Map). USGS Publications Warehouse. <https://doi.org/10.3133/mf1787>

- Lipman, P. W. (1989). Oligocene–Miocene San Juan volcanic field, Colorado. In C. E. Chapin & J. Zidek, *Field excursions to volcanic terranes in the western United States, Volume I: Southern Rocky Mountain Region*. New Mexico Bureau of Geology & Mineral Resources.
- Lisenbee, A. L. (2013). Multi-stage Laramide deformation in the area of the southern Santa Fe embayment (Rio Grande rift), north-central New Mexico. In M. R. Hudson & V. J. S. (Tien) Grauch (Eds.), *New Perspectives on Rio Grande Rift Basins: From Tectonics to Groundwater* (Vol. 494, p. 0). Geological Society of America.
[https://doi.org/10.1130/2013.2494\(10\)](https://doi.org/10.1130/2013.2494(10))
- Malavarca, S., Singleton, J., Sitar, M., Byars, B., Magloughlin, J. F., & Rahl, J. (2022). *CHARACTERISTICS AND ORIGIN OF HIGH-GRADE METAMORPHISM OF THE PENNSYLVANIAN MINTURN FORMATION IN THE SANGRE DE CRISTO MOUNTAINS, SOUTHERN COLORADO*. Joint 118th Annual Cordilleran/72nd Annual Rocky Mountain Section Meeting - 2022. <https://doi.org/10.1130/abs/2022CD-374166>
- Marshall, D. (1996). Ternplot: An excel spreadsheet for ternary diagrams. *Computers & Geosciences*, 22(6), 697–699. [https://doi.org/10.1016/0098-3004\(96\)00012-X](https://doi.org/10.1016/0098-3004(96)00012-X)
- Madole, R. F., Romig, J. H., Aleinikoff, J. N., VanSistine, D. P., & Yacob, E. Y. (2008). On the origin and age of the Great Sand Dunes, Colorado. *Geomorphology*, 99(1), 99–119.
<https://doi.org/10.1016/j.geomorph.2007.10.006>
- McCalpin, J. (1981). *Quaternary Geology and Neotectonics of the West Flank of the Northern Sangre de Cristo Mountains, South-Central Colorado*.
<https://doi.org/10.13140/RG.2.2.25742.77129>
- McIntosh, W. C., & Chapin, C. E. (2004). *Geochronology of the central Colorado volcanic field*.

- Meerdink, S. K., Hook, S. J., Roberts, D. A., & Abbott, E. A. (2019). The ECOSTRESS spectral library version 1.0. *Remote Sensing of Environment*, 230, 111196.
<https://doi.org/10.1016/j.rse.2019.05.015>
- Miggins, D. P., Thompson, R. A., Pillmore, C. L., Snee, L. W., & Stern, C. R. (2002). *Extension and uplift of the northern Rio Grande Rift: Evidence from $^{40}\text{Ar}/^{39}\text{Ar}$ geochronology from the Sangre de Cristo Mountains, south-central Colorado and northern New Mexico*.
<https://doi.org/10.1130/0-8137-2362-0.47>
- O'Hara, K. (1988). Fluid flow and volume loss during mylonitization: An origin for phyllonite in an overthrust setting, North Carolina U.S.A. *Tectonophysics*, 156(1), 21–36.
[https://doi.org/10.1016/0040-1951\(88\)90280-6](https://doi.org/10.1016/0040-1951(88)90280-6)
- O'Hara, K. (1990). State of strain in mylonites from the western Blue Ridge province, southern Appalachians: The role of volume loss. *Journal of Structural Geology*, 12(4), 419–430.
[https://doi.org/10.1016/0191-8141\(90\)90031-S](https://doi.org/10.1016/0191-8141(90)90031-S)
- OpenStreetMap contributors. (2017). *Planet dump retrieved from <https://planet.osm.org>*.
- Passchier, C. W. and Trouw, R. A. J.: *Microtectonics*, 2nd, rev.enl. ed ed., Springer, Berlin ; New York, 366 pp., 2005.
- Paton, C., Hellstrom, J., Paul, B., Woodhead, J., & Hergt, J. (2011). Iolite: Freeware for the visualisation and processing of mass spectrometric data. *Journal of Analytical Atomic Spectrometry*, 26(12), 2508–2518. <https://doi.org/10.1039/C1JA10172B>
- Penn, B. S., & Lindsey, D. A. (2009). $^{40}\text{Ar}/^{39}\text{Ar}$ dates for the Spanish Peaks intrusions in south-central Colorado. *Rocky Mountain Geology*, 44(1), 17–32.
<https://doi.org/10.2113/gsrocky.44.1.17>

- Ramsay, J. G., & Graham, R. H. (1970). Strain variation in shear belts. *Canadian Journal of Earth Sciences*, 7(3), 786–813. <https://doi.org/10.1139/e70-078>
- Rasbury, E. T., Present, T. M., Northrup, P., Tappero, R. V., Lanzirrotti, A., Cole, J. M., Wooton, K. M., & Hatton, K. (2021). Tools for uranium characterization in carbonate samples: Case studies of natural U–Pb geochronology reference materials. *Geochronology*, 3(1), 103–122. <https://doi.org/10.5194/gchron-3-103-2021>
- Reed, J. C. R. Jr. (1984). Proterozoic rocks of the Taos Range, Sangre de Cristo Mountains, New Mexico. In *Guidebook—New Mexico Geological Society* (019816026; 35th Field Conference, Vol. 35, pp. 179–185).
- Reiners, P. W., & Brandon, M. T. (2006). Using Thermochronology to Understand Orogenic Erosion. *Annual Review of Earth and Planetary Sciences*, 34(1), 419–466. <https://doi.org/10.1146/annurev.earth.34.031405.125202>
- Ricketts, J. W., Kelley, S. A., Karlstrom, K. E., Schmandt, B., Donahue, M. S., & van Wijk, J. (2016). Synchronous opening of the Rio Grande rift along its entire length at 25–10 Ma supported by apatite (U-Th)/He and fission-track thermochronology, and evaluation of possible driving mechanisms. *GSA Bulletin*, 128(3–4), 397–424. <https://doi.org/10.1130/B31223.1>
- Roberts, N. M. W., Rasbury, E. T., Parrish, R. R., Smith, C. J., Horstwood, M. S. A., & Condon, D. J. (2017). A calcite reference material for LA-ICP-MS U-Pb geochronology. *Geochemistry, Geophysics, Geosystems*, 18(7), 2807–2814. <https://doi.org/10.1002/2016GC006784>
- Rollinson, H. R. (2014). *Using Geochemical Data: Evaluation, Presentation, Interpretation*. Routledge.

- Ruleman, C. A., & Brandt, T. R. (2021). *Surficial geology of the northern San Luis Valley, Saguache, Fremont, Custer, Alamosa, Rio Grande, Conejos, and Costilla Counties, Colorado* (Report No. 3475; Scientific Investigations Map). USGS Publications Warehouse. <https://doi.org/10.3133/sim3475>
- Sabin, T. G. (1994). *Geochronology and isotope geochemistry of early Proterozoic rocks exposed in portions of the Twin Peaks and Blanca Peak quadrangles, Alamosa, Costilla, and Huerfano counties, Colorado* [M.S. Thesis]. University of Kansas.
- Sanders, R. E., Heizler, M. T., & Goodwin, L. B. (2006). $^{40}\text{Ar}/^{39}\text{Ar}$ thermochronology constraints on the timing of Proterozoic basement exhumation and fault ancestry, southern Sangre de Cristo Range, New Mexico. *GSA Bulletin*, 118(11–12), 1489–1506. <https://doi.org/10.1130/B25857.1>
- Sibson, R. H. (1977). Fault rocks and fault mechanisms. *Journal of the Geological Society*, 133(3), 191–213. <https://doi.org/10.1144/gsjgs.133.3.0191>
- Sibson, R. H. (1985). A note on fault reactivation. *Journal of Structural Geology*, 7(6), 751–754. [https://doi.org/10.1016/0191-8141\(85\)90150-6](https://doi.org/10.1016/0191-8141(85)90150-6)
- Singleton, J. S., Rahl, J. M., & Befus, K. S. (2020). Rheology of a coaxial shear zone in the Virginia Blue Ridge: Wet quartzite dislocation creep at ~250–280 °C. *Journal of Structural Geology*, 140, 104109. <https://doi.org/10.1016/j.jsg.2020.104109>
- Steven, T. A., & Lipman, P. W. (1975). *Calderas of the San Juan volcanic field, southwestern Colorado* (Report No. 958; Professional Paper). USGS Publications Warehouse. <https://doi.org/10.3133/pp958>
- Stosch, H.-G. (2022). *REE diagram and “spidergram” template for Excel*. Zenodo. <https://doi.org/10.5281/zenodo.5985208>

- Sweet, D. E., Brotherton, J. L., Chowdhury, N. U. M. K., & Ramsey, C. E. (2021). Tectonic subsidence analysis of the Ancestral Rocky Mountains from the interior to the southern margin. *Palaeogeography, Palaeoclimatology, Palaeoecology*, 576, 110508. <https://doi.org/10.1016/j.palaeo.2021.110508>
- Sweet, D. E., & Soreghan, G. S. (2010). Late Paleozoic tectonics and paleogeography of the ancestral Front Range: Structural, stratigraphic, and sedimentologic evidence from the Fountain Formation (Manitou Springs, Colorado). *GSA Bulletin*, 122(3–4), 575–594. <https://doi.org/10.1130/B26554.1>
- Thompson, R. A., Turner, K. J., Lipman, P. W., Wolff, J. A., & Dungan, M. A. (2022). Field-trip guide to continental arc to rift volcanism of the southern Rocky Mountains—Southern Rocky Mountain, Taos Plateau, and Jemez Mountains volcanic fields of southern Colorado and northern New Mexico. In *Scientific Investigations Report* (No. 2017-5022-R). U.S. Geological Survey. <https://doi.org/10.3133/sir20175022R>
- Thoms, E., Haugerug, R., Crow, R., Wardwell, R., Rose, C., & Arrington, T. (2022). *GeMS Tools for ArcMap* [Python]. U.S. Geological Survey. <https://github.com/usgs/gems-tools-arcmap> (Original work published 2017)
- Touch GIS LLC. (2021). *Touch GIS - Powerful Field Data Collection & Visualization*. Touch GIS LLC. <https://www.touchgis.app/>
- Tweto, O. (1975). *Laramide (Late Cretaceous-Early Tertiary) Orogeny in the Southern Rocky Mountains*. <https://doi.org/10.1130/MEM144-p1>
- U.S. Geological Survey. (1983). *Aeromagnetic map of the Sangre de Cristo Mountains, Colorado* (Report No. 83–60; Open-File Report). USGS Publications Warehouse. <https://doi.org/10.3133/ofr8360>

- U.S. Geological Survey National Cooperative Geologic Mapping Program. (2020). *GeMS (Geologic Map Schema)—A standard format for the digital publication of geologic maps* (Report No. 11-B10; Techniques and Methods, p. 74). USGS Publications Warehouse. <https://doi.org/10.3133/tm11B10>
- van Daalen, M., Heilbronner, R., & Kunze, K. (1999). Orientation analysis of localized shear deformation in quartz fibres at the brittle–ductile transition. *Tectonophysics*, 303(1), 83–107. [https://doi.org/10.1016/S0040-1951\(98\)00264-9](https://doi.org/10.1016/S0040-1951(98)00264-9)
- Valdez, A. D.: Development and Eolian Geomorphology of Great Sand Dunes in Quaternary Geology of Great Sand Dunes, USGS Open-File Report 2007-1193, <https://doi.org/10.3133/ofr20071193>, p.7-10, 2007.
- Vaughan, A., Collins, N., Krus, M., & Rourke, P. (2014). *Recent Development of an Earth Science App—FieldMove Clino*. 14751.
- Vermeesch, P.: IsoplotR: A free and open toolbox for geochronology, *Geoscience Frontiers*, 9, 1479–1493, <https://doi.org/10.1016/j.gsf.2018.04.001>, 2018.
- Vollmer, F. W. (1990). An application of eigenvalue methods to structural domain analysis. *GSA Bulletin*, 102(6), 786–791. [https://doi.org/10.1130/0016-7606\(1990\)102<0786:AAOEMT>2.3.CO;2](https://doi.org/10.1130/0016-7606(1990)102<0786:AAOEMT>2.3.CO;2)
- Wallace, A. R. (2004). Evolution of the southeastern San Luis Basin margin and the Culebra embayment, Rio Grande rift, southern Colorado. *Geology of the Taos Region*, 181–192. <https://doi.org/10.56577/FFC-55.181>
- Watkins, T. A. (1996). GEOLOGY OF THE NORTHEASTERN SAN LUIS BASIN, SAGUACHE COUNTY, COLORADO. *Geological Society of America, Field Trip Guides*.

Weigel, J. F. (2014). *Evaluation of thrusting and folding of the Deadman Creek thrust fault, Sangre de Cristo Range, Saguache County, Colorado* [Colorado School of Mines].

<https://repository.mines.edu/handle/11124/12279>

Williams-Jones, A. E., Migdisov, A. A., & Samson, I. M. (2012). Hydrothermal Mobilisation of the Rare Earth Elements – a Tale of “Ceria” and “Yttria.” *Elements*, 8(5), 355–360.

<https://doi.org/10.2113/gselements.8.5.355>

Appendix A: Gabbro Geochemistry

Results from whole-rock geochemical analysis of $\text{P}\epsilon\text{g}$ sample 06-21-SC142 (i.e., Fig. 31), indicate that the rock is a tholeiitic gabbro. Proximal gabbroic-basaltic rocks that have been thoroughly geochemically characterized and dated to ~ 25 Ma include an alkali basalt/gabbro at Huerfano Butte ~ 70 km to the southeast of the study area, and tholeiitic basalts constituent to the Hinsdale Group which are well-exposed in the San Luis Hills, ~ 80 km to the south-southeast of the study area (Gilmer et al., 2022; Penn & Lindsey, 2009; Thompson et al., 2022). The former unit is localized to the immediate vicinity of Huerfano Butte itself (Penn & Lindsey, 2009), but exposures of the latter rocks are more widespread, albeit generally on the opposite side of the San Luis Valley (Thompson et al., 2022). Geochemical comparisons between mafic rocks in the Hinsdale Group (using data from Thompson et al. (2022), and Gilmer (personal communication, 2022)) and the $\text{P}\epsilon\text{g}$ intrusion suggest some significant differences: the $\text{P}\epsilon\text{g}$ stock is more mafic (Fig. A1a) and plots significantly closer to the ferro-basalt end of the tholeiitic magma series (Fig. A1b) than any of the mafic rocks in the Hinsdale group. A spidergram comparison indicates that $\text{P}\epsilon\text{g}$ is geochemically similar to the Hinsdale basalts except for relative enrichment in HREEs and other heavy, moderately incompatible elements (Fig. A1c). $\text{P}\epsilon\text{g}$ plots along trend with, but off the mafic end of Hinsdale basalts on all SiO_2 -major-oxide plots except possibly that of MgO (Fig. A2). Alteration of sample 06-21-SC142 is a possible complicating factor in these comparisons; though the sampled outcrop is much less pervasively altered than other $\text{P}\epsilon\text{g}$ exposures, some sericitization is visible in thin section (i.e., Fig. 10A).

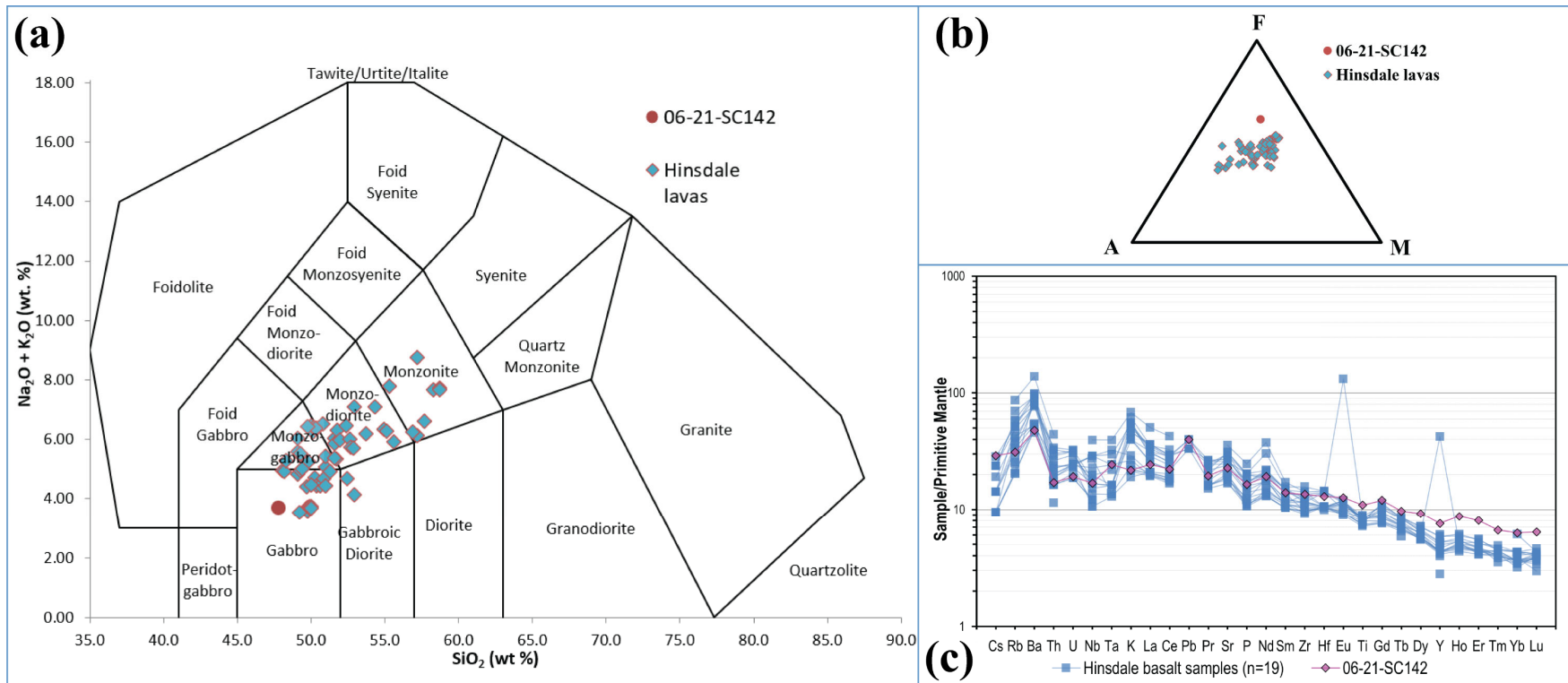


Figure A.1. Plots of whole-rock-geochemistry analytical results for **Fig** sample 06-21-SC142 alongside published (Thompson et al., 2022) and unpublished (A. Gilmer, personal communication, 2022) whole-rock geochemical analyses of basalts in the Hinsdale Group. (a) Plutonic TAS diagram (Iacovino, Kayla & Asimow, Paul, 2018). (b) AFM plot (Marshall, 1996). (c) Primitive-mantle-normalized spider diagram (Stosch, 2022).

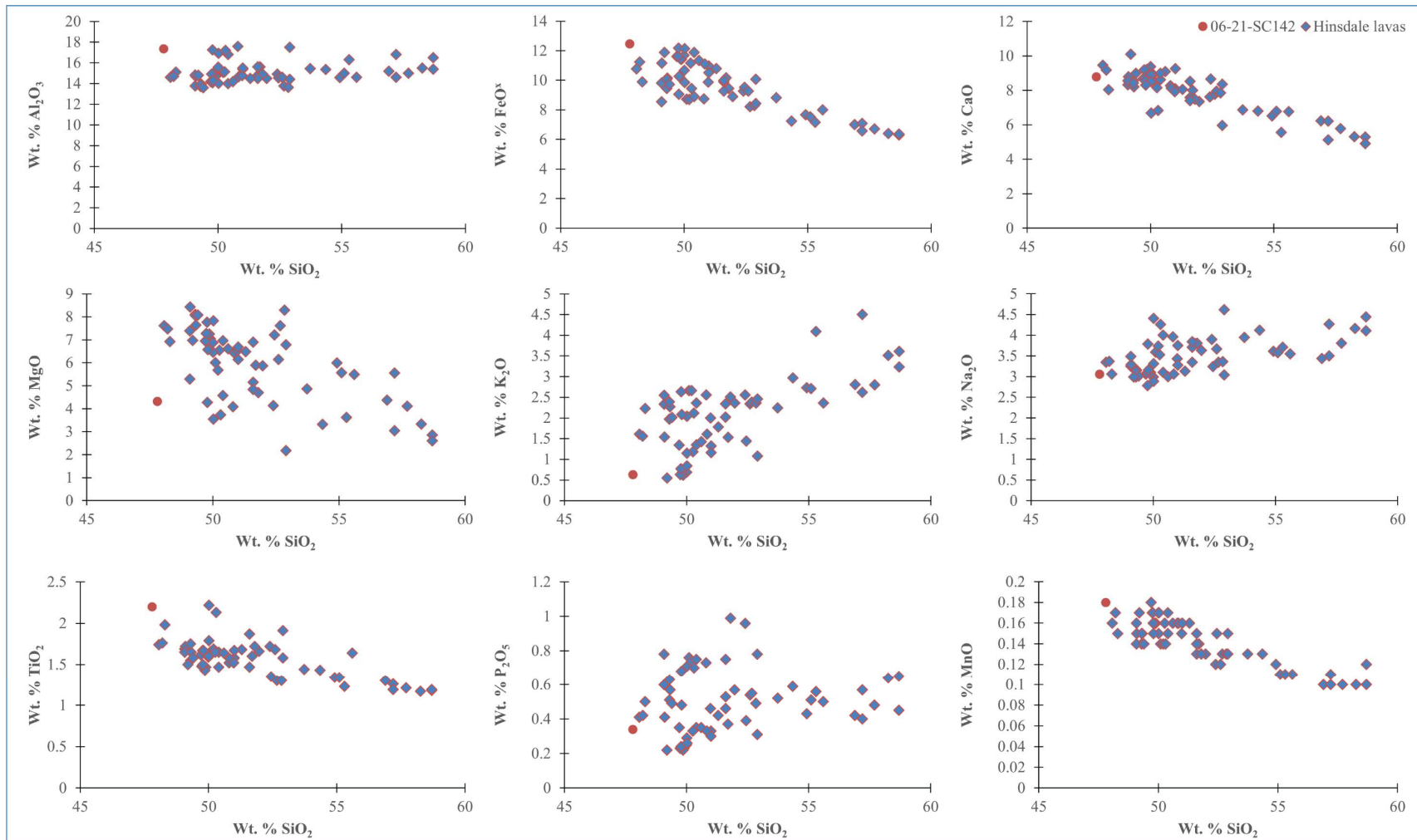


Figure A.2. Assorted SiO₂ (x axis) vs. major element oxide (y-axis) comparing the geochemistry of sample 06-21-SC142 to that of basaltic lavas in the Hinsdale Group; Hinsdale geochemical data from Thompson et al. (2022) and A. Gilmer (personal communication, 2022).

Though **F_{εg}** and gabbroic-basaltic intrusive stocks of similar probable ages and compositions have been noted by previous workers in and nearby the study area (Clement, 1952; Johnson et al., 1987; Lindsey, Soulliere, et al., 1985; Watkins, 1996), they have not been correlated with units outside the range. This study does not interpret such a correlation either; the unit is broadly geochemically similar to the nearby Hinsdale Group basalts (Gilmer et al., 2022; Thompson et al., 2022), but is significantly more mafic and relatively enriched in HREEs (Figs. A1, A2). This HREE enrichment could be partially metasomatic, but could also potentially be explained either by higher proportions of hornblende (which accumulates HREEs (Rollinson, 2014)) in **F_{εg}** than in Hinsdale basalts given a similar magmatic source composition, or by differences in magmatic source chemistries. A more detailed investigation involving sampling and geochemical characterization of the full suite of apparent Cenozoic igneous rocks in the area would be required to conclusively identify any relationships between **F_{εg}** and regional volcanic units; hypabyssal rocks (i.e., Tad) presumed to be co-genetic (Plate 1, XC B-B') with **F_{εg}** may have compositions closer to those of the Hinsdale basalts. Broadly, however, geochemical and geochronological analyses of **F_{εg}** are consistent with the same regional trend of early rift volcanism (Gilmer et al., 2022; Thompson et al., 2022) that produced the Hinsdale basalt deposits.